IS-T- 900

Crack depth determination by ultrasonic frequency analysis aided by dynamic photoelasticity

by

Anmol Singh

M.S. Thesis submitted to Iowa State University

Ames Laboratory, DOE
Iowa State University
Ames, Iowa 50011

Date Transmitted: August 1980

PREPARED FOR THE U.S. DEPARTMENT OF ENERGY
UNDER CONTRACT NO. W-7405-eng-82

DISCLAIMER

Printed in the United States of America

Available from
National Technical Information Service
U.S. Department of Commerce
5265 Port Royal Road
Springfield, VA 22161

TABLE OF CONTENTS

ABSTRACT

The work reported in this thesis describes a non-destructive method for characterizing the depth of artificial surface-breaking flaws (slots) using Rayleigh surface waves.

Dynamic photoelasticity was used in the first part of this study to obtain a full-field visualization of the waves generated on interaction of a Rayleigh wave with a slot. This visualization showed that for slot lengths of the same order of size as the predominant wavelengths in the incident Rayleigh wave, there is a significant interaction of the subsurface Rayleigh disturbance with the slot tip, producing transmitted surface disturbances that were quantitatively analyzed. Specifically, the frequency content of these transmitted waves was found for four different slot depths. The high frequency components of these transmitted signals exhibited a "maximum" frequency which decreased with increasing slot depth. This was attributed to the fact that the maximum frequencies of the subsurface field of the incident Rayleigh wave decrease with increasing depth.

Ultrasonic testing was also done on surface slots in steel blocks, using commercial Rayleigh wave transducers. A relationship similar to the photoelastic results was obtained for the frequency components of the transmitted waves at the surface relative to the slot depth. However, in the ultrasonic case, there was a definite high frequency "cut off" point which could be directly related to the slot depth for

slots perpendicular to the surface. This relationship was shown to also accurately predict the depth of inclined slots.

1. INTRODUCTION

Small defects can cause major disasters. Aircraft have crashed, oil pipelines have ruptured and nuclear reactors fail because of undetected cracks. Material or manufacturing defects, however, cannot be completely avoided. So, in order to assess the safety of a structure, it is important to establish without damaging it whether a component or structure contains defects, and if so, to decide if it can continue to be used in operation. This process, which is rapidly developing into a science, is called non-destructive evaluation or NDE (1).

The aim of NDE is not to reject a product having a defect. This would imply finding smaller and smaller flaws and rejecting more and more parts. Its aim is rather to characterize flaws and to know how serious they are. Characterization of flaws means determining their size, shape, orientation, boundary characteristics, composition, etc. By characterizing in this way and by using the techniques of fracture mechanics, it is possible to quantify the safe limits for operation of a structure.

During the 1950's and early 1960's, it was necessary to assume that an airframe structure was free of defects (2). The maximum design stress on the structure was kept well below the yield strength of the material. As the stress level in structures went up higher, however, serious structural problems were faced. The higher strength materials that were being introduced somehow were more prone to failure than their "weaker" but tougher predecessors. Then came fracture mechanics (3). The designer now assumed that his structure contains initial flaws.

It is, of course, not possible to detect flaws to absolute limits. It is found, for example, that in ultrasonic testing there is a 90 percent probability of rejecting a component which has a flaw size less than a specified initial size and a 10 percent probability of not rejecting a part with a flaw bigger than a specified size. This clearly indicates the importance of the continued development of NDE technology. Such development will not only make structures safer, but also avoid unnecessary rejection of parts.

NDE also can play a significant role in aircraft maintenance. The turbine disks used in aeroplanes, for example, are retired after a certain number of service hours, on the basis of statistical criteria which predict that disks may start failing after a certain time, even though they have designed lives from four to five times longer than this statistical time period. Replacing a disk prematurely is expensive; each costs upward of $20,000. To avoid such gigantic losses, the Air Force Materials Laboratory has set up a large NDE based program called Retirement for Cause at Wright Patterson Air Force Base near Dayton, Ohio.

Ultrasonics has a great potential for NDE. The acoustic waves, after interacting with a flaw contain information that can be used to characterize that flaw.

During the last few years the potential economic pay-off of NDE has been recognized. As a result, there has been a tremendous emphasis on research towards improving all aspects of nondestructive testing (NDT) (4). In England, for example, the Non-destructive Research Centre at

Harwell (5) was set up in 1967 with a staff of seven. The Centre now gets 500 requests a year for advice or assistance, and receives about 400 visitors each year. The ultrasonic research program at Harwell includes diffraction techniques for sizing cracks, volumetric defect sizing by creeping waves and studies to improve ultrasonic transducers. The center maintains close contact with British industry and has sponsored an acoustic emission program at Imperial College in London. It is also supporting ultrasonic 'camera research' at City University, London. The research group at the City University is also involved in checking the hydrothermal degredation of adhesive bonded joints and in surface crack characterization.

There are several major NDE programs in the U.S.A. The Electric Power Research Institute (EPRI), for example hasan extensive NDE program. Their center at Palo Alto has drawn top notch scientists from several disciplines to make fundamental contributions to the solution of NDE problems. One such problem is in modelling of realistic flaws and cracks for experimental work. EPRI is currently spending $500,000 per year learning how to make realistic cracks in model reactor components, such as cracks in nozzle welds.

A group led by Gordon S. Kino (6) at Stanford University is primarily involved in ultrasonic imaging. The imaging technique not only determines the location of a flaw but is also used to characterize it. Using this technique, small reflectors of less than 1 mm have been detected reliably.

These few examples are sufficient to show that there is interest in the quantitative aspect of nondestructive testing.

This thesis describes a method for sizing surface cracks which have been modelled as machined slots. Several techniques have been used in the past to size surface cracks. They mostly use compressional (P) and shear (S) waves. There has been much less attention given to using Rayleigh (R) waves or surface waves for sizing cracks. Since the energy of Rayleigh waves is confined to a layer of material near the surface, these waves seem to have a great potential for sizing surface cracks. These are exactly the cracks that are hardest to characterize with traditional ultrasonic techniques because they lie in the "near field" region of the transducers.

The research reported here was done in two phases. First of all, a dynamic photoelasticity technique was chosen to study the overall wave behavior and the mode conversions of a Rayleigh wave as it interacts with narrow slots cut from the edges of a two dimensional plate models. This technique gives a full field visualization of the stresses produced by an elastic wave traveling in a solid. The interaction between a Rayleigh wave and a slot could be observed from a sequence of pictures taken with a high speed Cranz-Schardin camera. Rather than using the familiar amplitude technique, we have concentrated on the frequency analysis of the transmitted Rayleigh wave. The transmitted wave was chosen because it has travelled fully around the slot and should therefore, contain the most information on the characteristics of the defect. A relationship was found between certain aspects of the spectroscopic analysis of the transmitted wave and the depth of edge slots. In the second phase, results from the photoelastic analysis were compared to

the data received from ultrasonic surface wave transducers placed on steel blocks with machined slots. Fast Fourier frequency analysis of the ultrasonic surface wave signals showed a relationship with slot depth that was similar to that observed in the photoelastic models. The fact that the depth of the Rayleigh wave is a function of the wavelength was found to be the important property which can be used to find the depth of surface breaking flaws.

II. LITERATURE REVIEW

Research in surface crack characterization can be divided into three categories; techniques that use amplitudes of the scattered waves, timing methods and, lastly, spectroscopic analysis. Compressional, shear and Rayleigh waves may be used in these methods.

A. Amplitude Methods

The pulse-echo technique using bulk waves (P and S) is the most conventional of the amplitude techniques. The amplitude of the signal reflected from the defect is related to the crack size (7). Artificial reference defects are created by machining edge slots or by producing them by electric-discharge machining. Discrepancies (8) in the amplitude of a reflected signal have been found when comparing results from slotted reference blocks to the signals received from cracks produced by fatigue. It has also been found that the amplitude of the signal from the fatigue crack depends on the cycle conditions used to produce the crack. The ultrasonic signals produced by low cycle fatigue cracks were stronger, than those from low stress high cycle fatigue cracks. The amplitude of the signal also depends on the crack shape, crack surface roughness, the state of stress near the crack (9, 10) and "mode conversion." In the last case energy is converted from one kind of particle motion to another, e.g. from P-wave to S-wave motion. In addition the amplitude of the reflected wave depends on interference effects which, in turn depend on the size

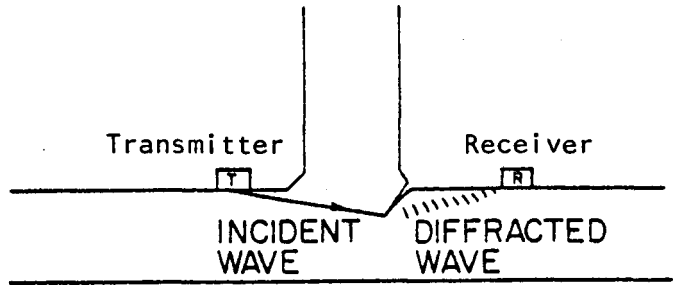

Fig. 2.1. Measuring the amplitude of the diffracted wave for crack depth measurement

and shape of the crack (11). The pulse-echo technique is, therefore, not very reliable for finding and characterizing surface cracks. The intensity of the reflected signal depends on too many interrelated variables.

Several other techniques have recently been tried which analyze the amplitude of the scattered wave. When an incident beam interacts with a crack-like defect, some of its energy is scattered by the defect. Bottcher et al. (12), for example, found that the amplitude of the scattered wave due to the grain boundaries under a slot is dependent on the depth (Fig. 2.1). Silk and Lidington (13) pointed out that the signal also depends on diffraction at the edge of the crack. They list four possible disadvantages of this technique, and suggest that the delay time of the diffracted signal be used instead of its amplitude.

During the last couple of years investigators started to recognize the potential value of Rayleigh waves for characterizing surface and near surface defects. This wave has its energy confined to a depth of

approximately two times its wavelength so that it is not disturbed by internal or back surface reflections, etc. Reinhardt and Dally (14) used photoelastic visualization to study the interaction of Rayleigh waves with surface flaws. They found the variation of transmission and reflection coefficients for slots with depths up to half of Rayleigh wavelength. Bond (15) used a numerical technique to study the interaction of Rayleigh waves with slots. He indicated that the finite difference modelling, as shown in Fig. 2.2, is a powerful technique for getting a quantitative understanding of the interaction and resulting scattered pulses from flaws with configurations that render them analytically intractable.

Figure 2.2(a) shows the displacements caused by the input R-wave in a finite difference model. On interacting with the slot, several waves are generated as shown in Fig. 2.2(b). These wave are identified in Fig. 2.2(c), in which C is a compressional wave, S is a shear wave, PS is a Von-Schmidt wave and R_t and R_r are "transmitted" and "reflected" Rayleigh waves respectively.

B. Timing Methods

Considerable emphasis has been placed on this technique by the investigators at the Harwell Non-Destructive Centre (16). If a surface opening crack is present between a transmitter and a receiver (Fig. 2.1), the time/spatial separations between certain spatial reflection and the diffracted or scattered tip echoes can provide relevant information

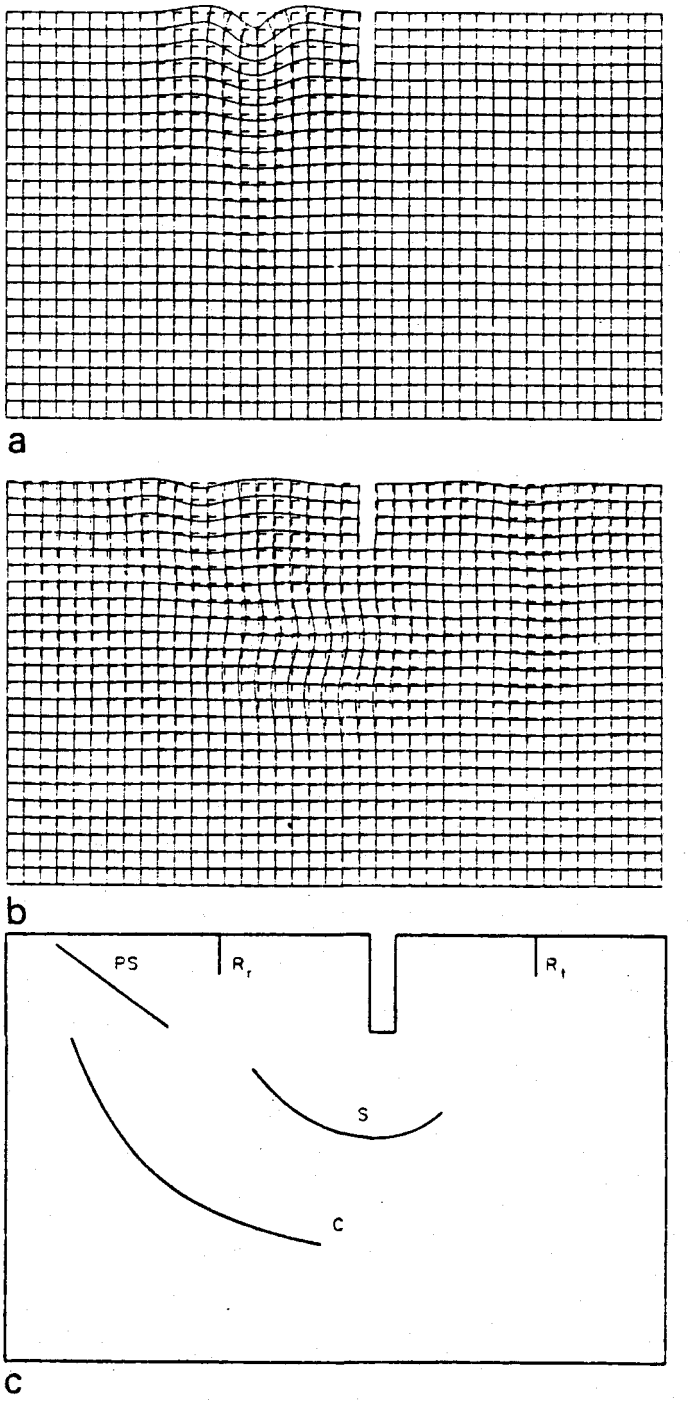

Fig. 2.2. Finite difference studies used by Bond (15)

about crack depth. Silk and Lidington (17) placed a transmitter and receiver on the opposite sides of a slot and used the transit time of the longitudinal pulse to determine the depth. By knowing the probe separation and wave speed, elementary geometry can be applied to calculate the depth. They were able to measure the depths of artificial slots, 1-30 mm deep to within $\pm$ 0.5 mm.

Recently, Silk (18, 19) used the timings between two diffracted longitudinal wave signals as shown in Fig. 2.3 to size internal cracks. The presence of a near surface or lateral wave is an indication that the crack is internal. He was able to size buried fatigue cracks of over 6 mm in depth to an accuracy of 0.5 mm. An improvement of accuracy for sizing small cracks (< 6 mm) is thus required.

In another study Silk and Lidington (20) used a single probe in transmit/receive mode for sizing fatigue cracks as shown in Fig. 2.4. The time taken for the "crack tip reflection" which is the mathematical equivalent of "zero" angle diffraction, was used directly to find the depth of the crack. They noted a variability which they attributed to microdefects in the region of the crack tip. These may cause variations in reflectivity. They also pointed out that, when the crack is jagged in cross section, it becomes possible for reflections from individual facets to dominate the reflected signal causing an under estimate of crack depth. Further work on the theoretical and experimental side is required before we will fully understand the diffraction and scattering from a crack tip as detected by a single probe. This single probe

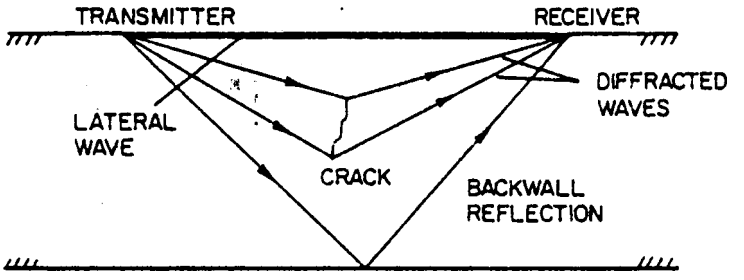

Fig. 2.3. Using the flight time of various signals to size internal cracks

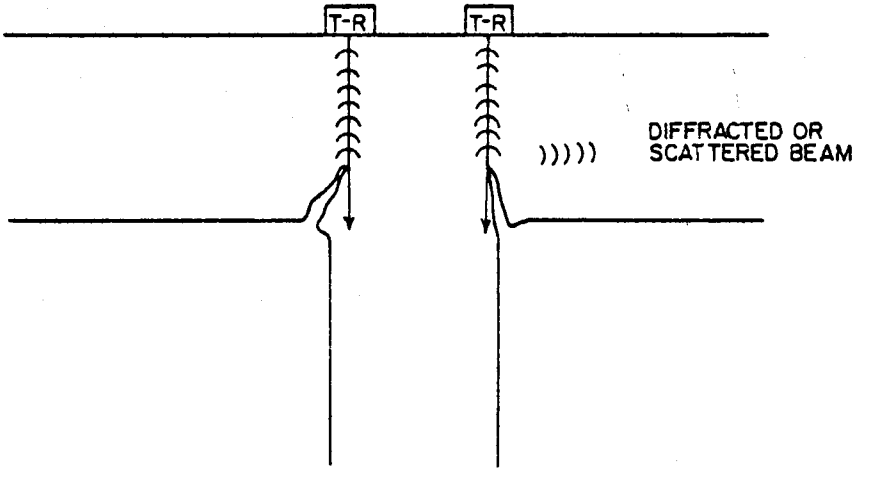

Fig. 2.4. Crack tip reflection using a single probe. (T-R = Transmitter - Receiver)

technique cannot be used when there is a weld or component on the opposite side of the crack tip. For such cases Silk suggested the use of either oblique beam sighting from two or more positions or the two probe technique.

The use of shear waves looks attractive for the timing method. They travel slower than P waves and thus have increased sensitivity. The biggest problem with generating shear waves is that they require a rigid coupling between the transducer and the test piece. There is also a difficulty in identifying them from other mode converted signals. Whereas P waves travel fastest they do not become mixed with other reflected or mode converted waves. S waves, on the other hand, are frequently mixed in with P, S or R waves that are reflected or mode converted at various sources.

Work on using the Rayleigh wave timing methods has predominantly been done in the U.K. If the depth of the surface wave (about 2λ) is smaller than the crack depth then the near surface part of the Rayleigh wave incident at the crack opening is forced to travel around the crack. The delayed time of arrival at a second receiving transducer can then be used to monitor the crack depth.

Silk (21) and Hall (22) both used this technique to size surface cracks by placing a transmitter and a receiver on opposite sides of a crack. Hall noted that three signals were received; the first he called the diffracted shear from the crack tip, the second the mode converted shear wave from the Rayleigh wave; and the last to arrive was the

Rayleigh wave. Investigators at Iowa State University including the author of this thesis, found that the first and the second signals noted by Hall consist of a mixture waves i.e., the Rayleigh wave, formed at the crack tip by subsurface particle motion of the portion of the incident Rayleigh wave which is deeper than the crack, plus other mode converted and diffracted waves. This is discussed in Chapter IV. For an inclined crack Silk suggested taking two measurements by interchanging the transmitter and the receiver to obtain more information. Hall then used the timing of the last signal, i.e. the Rayleigh wave which goes all around the crack to successfully size fatigue cracks in rails. He further clarified the sources of the three signals by using a photoelastic visualization technique in glass. The major drawback of the method is that for small cracks the three signals merge together. Any timing method which relies on separating them is, therefore, unsuitable.

Investigators at the City University (23) in London used finite difference techniques to study the mode conversions from a P wave (Fig. 2.5) incident directly at the bottom of the slot. They found that the wave mode converted to a Rayleigh wave at the bottom of the slot (R_2) and also at the slot opening on the surface (R_1). The time interval between the arrival of these two Rayleigh waves increased as the slot was made deeper and wider.

Silk (16) also used a single surface wave probe to size cracks (Fig. 2.6). He used the timing of the direct reflections from the crack opening and the crack tip to find the depth of the crack. The

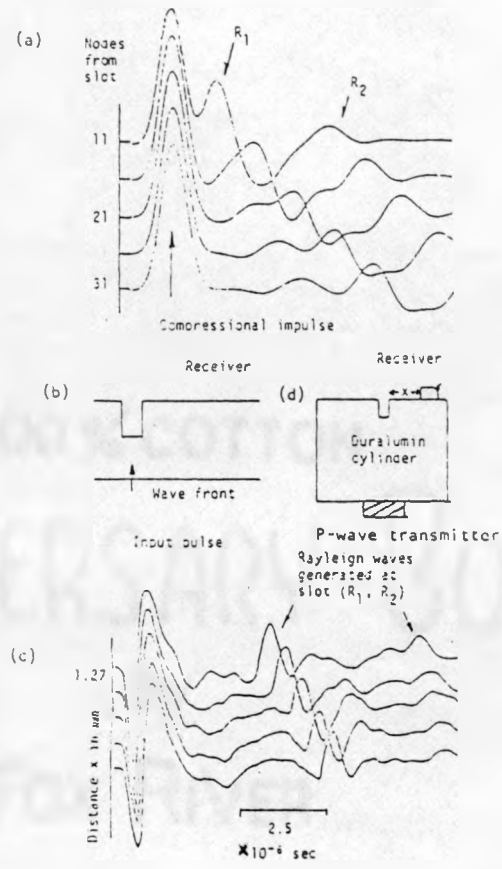

Fig. 2.5. Compressional Rayleigh wave mode conversions at a slot.

(a) Finite difference results from the model shown in (b)
(b) Experimental results from the specimen shown in (d)

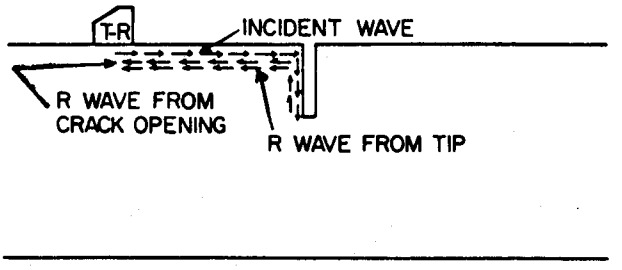

Fig. 2.6. Reflections of Rayleigh wave from slot/crack opening and the tip

probe was scanned to provide the necessary resolution for estimating the crack depth when the crack is suspected of changing direction.

Both the single probe and the two probe techniques are limited to deep cracks so that the various signals do not superimpose. It is possible to improve this technique by using very short pulses so that it becomes easier to differentiate various signals in the time domain.

C. Ultrasonic Frequency Analysis

Until recently ultrasonic frequency analysis was mainly used to characterize internal flaws. It uses a broadband ultrasonic pulse which is analyzed in the frequency domain at incidence and on reflection. Adler et al. (24) used this method to determine the size of buried planar circular flaws with arbitrary orientation in aluminum and carbon steel. He also characterized flaws in heavy section steel weldments.

Morgan (25) analyzed the reflected signal from a slot milled in aluminum and found certain modulations in the frequency spectrum. These were also observed by Zachary et al. (26) when they analyzed the transmitted signal of the Rayleigh wave using dynamic photoelasticity. These modulations are probably caused by resonances of the crack faces and as such should contain sufficient information to characterize a crack.

Bond (27) used a broadband band (0.5 - 6 MHz) longitudinal wave transmitter, and placed it below the slot on the opposite face of the plate (Fig. 2.5). A receiver placed on the side of the slot detected a Rayleigh wave. The peak frequency of this mode converted Rayleigh wave was plotted for each slot. The peak frequency (f) of the Rayleigh wave was related to the depth of the slot as follows.

$$\text{Slot depth} \propto \frac{1}{f^2}$$

The technique was used on slots 0.33 mm wide and from 0.5 to 3 mm deep in a duralumin cylinder.

The use of spectral analysis or "spectroscopy" of signals to determine the depth of surface cracks is relatively new. It is the method used in this thesis but the approach taken is slightly different from that taken by Bond. The technique has tremendous potential for research because there are several different modes of converted and scattered signals that should be investigated to find how they correlate to crack depth. There is, as yet, no theoretical analysis

available on the interaction of a wave with a slot. Experimental and numerical studies are needed to fully develop this method.

Not only is ultrasonic spectroscopy being tried for characterizing internal flaws and surface cracks, but it is now being developed to monitor hydrothermal degradation of adhesive bonded joints of the type used in aircraft. Lloyd et al. (28) claimed that this method is sufficiently sensitive to give early warning on the loss of adhesive strength.

III. THEORY AND EQUIPMENT

Since the research for this thesis deals directly with the interaction between waves and defects, a brief discussion of wave propagation in elastic solids is given in this Chapter. This is followed by a discussion of the methods of generating different kinds of waves and, finally the photoelasticity system which we used to visualize waves, is described.

A. Waves in Elastic Media (29)

1. Longitudinal and transverse waves (29)

Waves in elastic media are generated by the motion of particles. A plane displacement wave propagating with a velocity c, in a direction defined by the unit propagation vector $\hat{p}$ is represented by

$$\bar{u} = f(\bar{x}.\ \hat{p} - ct)\hat{d} \tag{3.1}$$

where $\hat{d}$ defines the direction of particle motion, $\bar{u}$ is displacement, $\bar{x}$ defines the coordinate and t is time.

In the absence of body forces, the components of the displacement vector in a homogeneous, isotropic, linearly elastic medium are governed by the following system of partial differential equations:

$$\mu\nabla^2\bar{u} + (\lambda + \mu)\nabla\nabla.\bar{u} = \rho\ \ddot{\bar{u}} \tag{3.2}$$

where $$\nabla = \hat{i}_1 \frac{\partial}{\partial x_1} + \hat{i}_2 \frac{\partial}{\partial x_2} + \hat{i}_3 \frac{\partial}{\partial x_3}$$

λ and μ are Lame's constants, ρ is mass density. Substituting equation (3.1) into (3.2) it is found that the equations are satisfied

in only two ways (29)

$$\text{either } \hat{d} = \pm \hat{p} \quad \text{or} \quad \hat{p} \cdot \hat{d} = 0$$

If $\hat{d} = \pm \hat{p}$, we have $\hat{d} \cdot \hat{p} = \hat{p} \cdot \hat{d} = \pm 1$

In this case, the motion of the particles is in the same direction as the direction of propagation of the wave. The wave is called a longitudinal, dilitational, compression, pressure or a P-wave. The velocity of propagation of the wavefront is c_L.

$$\text{If } \hat{p} \cdot \hat{d} = 0$$

then the motion of the particles is transverse to the direction of propagation so the wave is called a transverse, distortion, shear or a S-wave. The velocity of the shear wave is then equal to c_T.

In terms of the usual material elastic constants, the bulk wave velocities in 3-dimensional bodies are given by

$$c_L = \left[\frac{E}{\rho} \frac{(1-\nu)}{(1+\nu)(1-2\nu)}\right]^{1/2} \tag{3.3}$$

$$c_T = \left[\frac{E}{\rho} \frac{1}{2(1+\nu)}\right]^{1/2} \tag{3.4}$$

$$\frac{c_L}{c_T} = \left[\frac{2(1-\nu)}{1-2\nu}\right]^{1/2} \tag{3.5}$$

where E = Elastic modulus ν = Poisson ratio

For $\nu = 0.3$ this gives $c_L/c_T = 1.87$.

The dilatational velocity is modified for plates as

$$c_L' = \left[\frac{E}{P} \frac{1}{1-\nu^2}\right]^{1/2} \tag{3.6}$$

for rods as, $c_L'' = \left[\frac{E}{P}\right]^{1/2}$ (3.7)

c_T, the shear wave velocity is unaffected.

2. Rayleigh waves (29)

The longitudinal and the shear waves are both referred to as bulk waves. A wave whose disturbance is largely confined to the neighborhood of the boundary of an elastic half space is known as a Rayleigh, surface or R-wave. The particle motion of Rayleigh waves is elliptical as shown in Fig. 3.1. The displacement in a surface wave decays rapidly with distance from the free surface. The phase velocity, c of the Rayleigh wave can be found from the equation

$$\left[2-\frac{c^2}{c_T^2}\right]^2 - 4\left[1-\frac{c^2}{c_L^2}\right]^{1/2}\left[1-\frac{c^2}{c_T^2}\right]^{1/2} = 0 \qquad (3.8)$$

It is clear that equation (3.8) is independent of the wave number $= \frac{2\pi}{\lambda}$, thus the velocity is independent of the wavelength. Due to this reason the pulse shape does not change and the wave is non-dispersive. A good approximation to the velocity of a Rayleigh wave can be written as (29)

$$c = c_R = \frac{0.862 + 1.14\nu}{1 + \nu}\ c_T \qquad (3.9)$$

For $\nu = 0.3$ this gives $c_R = .93\ c_T = 0.74\ c_L$.

For plates the Rayleigh wave velocity is the same as in eq. (3.9).

Figure 3.2 shows relative displacements for a Rayleigh wave. The displacements are localized in a thin layer near the surface, with a thickness approximately equal to two times its wavelength. However, at a depth greater than 1.2λ the amplitude of the motion is so small that it is often ignored and is certainly not discernible within the resolution of the photoelastic system that was used.

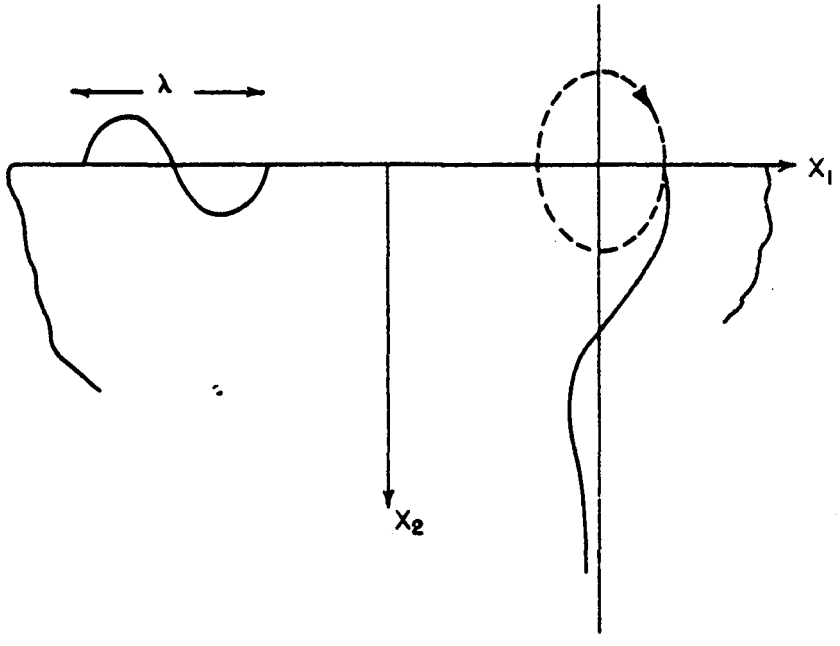

Fig. 3.1. Rayleigh waves

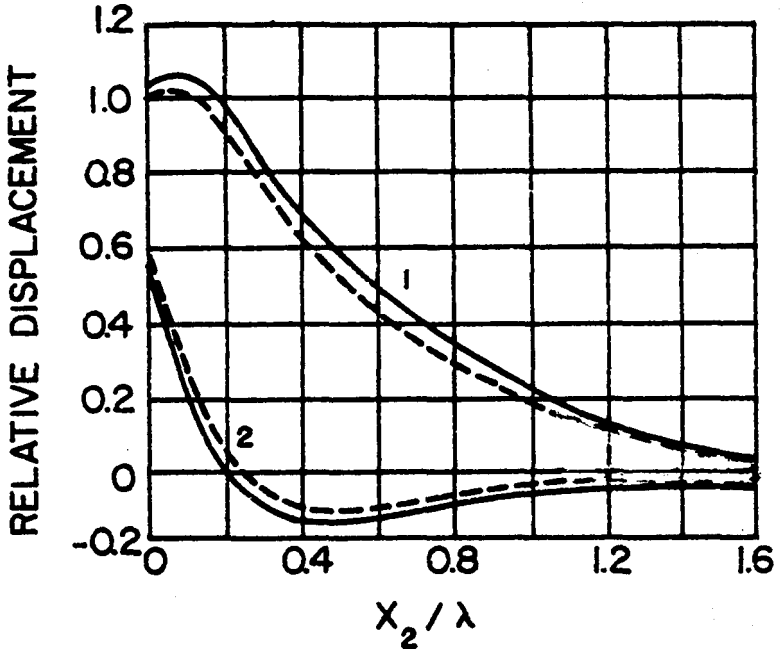

Fig. 3.2. Displacements amplitudes for Rayleigh waves in the depth from a free surface. $u_1/u_2(x_2 = 0)$, curves 2, and $u_2/u_2(x_2 = 0)$, curves 1, for ν=0.25 (---) and ν=0.34 (—), (29)

3. Reflection and refraction of plane waves

When a plane harmonic wave encounters a free boundary, the energy in the particle motion is reflected. If the wave interacts at the interface of two semi-infinite media then reflection and refraction of energy occurs. The system of incident, reflected and refracted waves must satisfy four conditions of continuity at the boundary: The stresses as well as the displacements at the interface of two half spaces must be compatible. Thus, for a single incident wave four waves can exist, two as reflected and two as refracted waves. Fig. 3.3 shows the reflected and refracted waves for an incident P-wave. The angles of incidence, reflection and refraction follow the generalized Snell's Law

$$\frac{c_o}{\sin\theta_o} = \frac{c_n}{\sin\theta_n} \tag{3.10}$$

where c_o is the velocity of the incident wave at an angle of θ_o. c_n represents the velocities of either reflected or refracted waves corresponding to an angle of reflection or refraction θ_n (n = 1, 2, 3, 4).

When a P-wave is incident on the free boundary of a half space, two waves are reflected (Fig. 3.4). In order to satisfy the boundary condition one of the reflected waves has to be a longitudinal wave and the other a vertically polarized SV-wave. A SV-wave is a shear wave, whose direction of particle motion is normal to the direction of propagation in the $(x_1\ x_2)$ - plane. A horizontally polarized shear wave, SH-wave, has particle motion normal to the direction of propagation but in the x_3 direction.

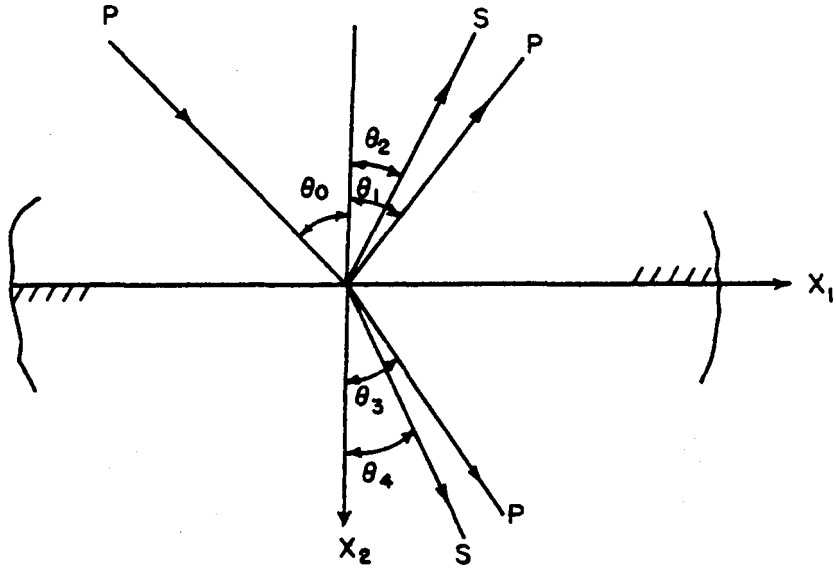

Fig. 3.3. Refraction and reflection of a P-wave at the interface between two semi-infinite media ($\theta_o = \theta_1$)

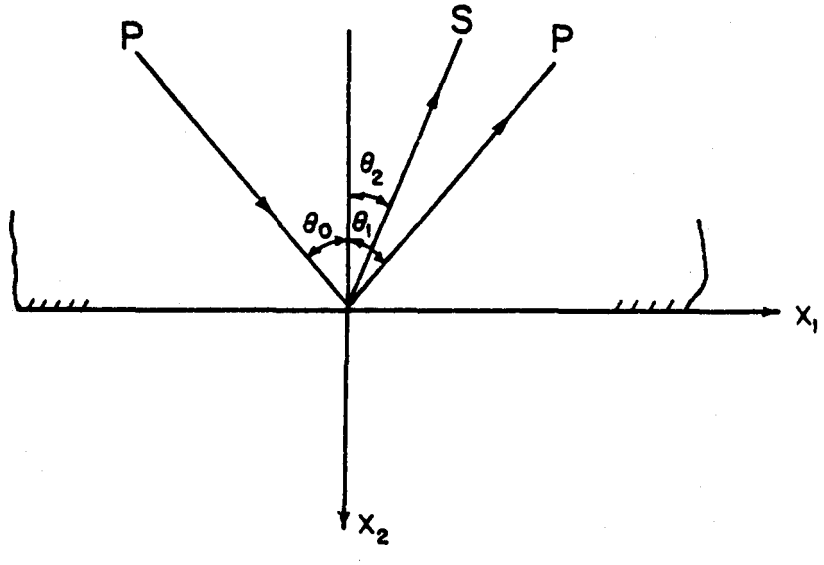

Fig. 3.4. Reflection of P-wave ($\theta_o = \theta_1$)

When, at an interface, one of the reflected or refracted angles is 90°, the incident angle is called the critical angle corresponding to the reflected or refracted wave. For this particular angle, the reflected or refracted wave becomes a surface wave and grazes along the interface. A Rayleigh wave can be generated in this manner by a P-wave incident on a wedge, which is placed on another material, so that the refracted P or S waves travel along the boundary as a surface wave. Detailed discussion on mode conversions, which is the conversion of one kind of particle motion to another can be found in several tests (29,30).

B. Ultrasonic Waves in Testing of Materials

1. Generation and reception of ultrasonic waves

The principle of generation and reception of ultrasound is based on the piezoelectric effect. It is a property of certain materials whereby electrical charges are produced on the surface when the material is deformed. Conversely, if the material is placed between two electrodes and a electric field voltage pulse is applied on the surfaces, it will produce a deformation of the material.

One of the piezoelectric materials used is the quartz crystal. It has the form of a hexagonal prism. The crystal has one z-axis, three x-axes and three y-axes, also known as the polar axes as shown in Fig. 3.5.

The crystal is cut with different orientations to produce different kinds of waves. For an x-cut crystal, which has the y and z-axes in the plane of the plate, and the x-axis normal to it, the deformations

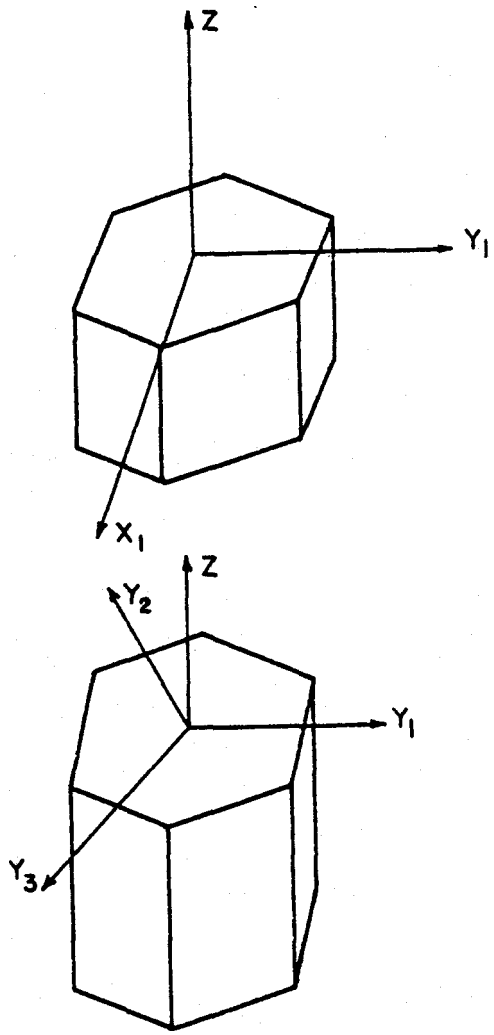

Fig. 3.5. Crystal axes in quartz

that occur when a voltage is applied to the opposite faces of the plate are shown in Fig. 3.6. The deformation in the x direction is used to produce longitudinal waves. The deformations along the y-axis and the change in the shape produces transverse waves. Transverse waves can be avoided by using a couplant which will not transmit the shear action so that only the longitudinal motion is transmitted. The x-cut crystal also acts as a receiver for longitudinal waves as these waves cause deformation to the crystal, producing a potential on its face.

Shear waves are generated by a y-cut crystal of quartz. On application of a potential to the opposite faces of the crystal, it deforms in such a way that, if the crystal is coupled with a tough cement to the test material, it generates shear waves. The reverse effect is used for the reception of shear waves.

Rayleigh waves are generated by incident longitudinal or shear waves at a critical angle so that the refracted shear in the test material is at 90° or grazes along the surface. The refracted shear wave mode converts to a R-wave at the surface. Normally a lucite or copper wedge is used on which the P-wave transducer is placed. The angle of incidence of the P-wave can be obtained from equation (3.10), where the incident P-wave velocity, corresponds to that in the wedge and the refracted shear wave velocity, corresponds to that in the test material. It is important to realize that the wedge angle depends on the test material, so the wedge designed for a particular material cannot be used for another. When using an incident shear wave in the wedge they must be SV-waves since SH-waves cannpt produce R-waves in the steel.

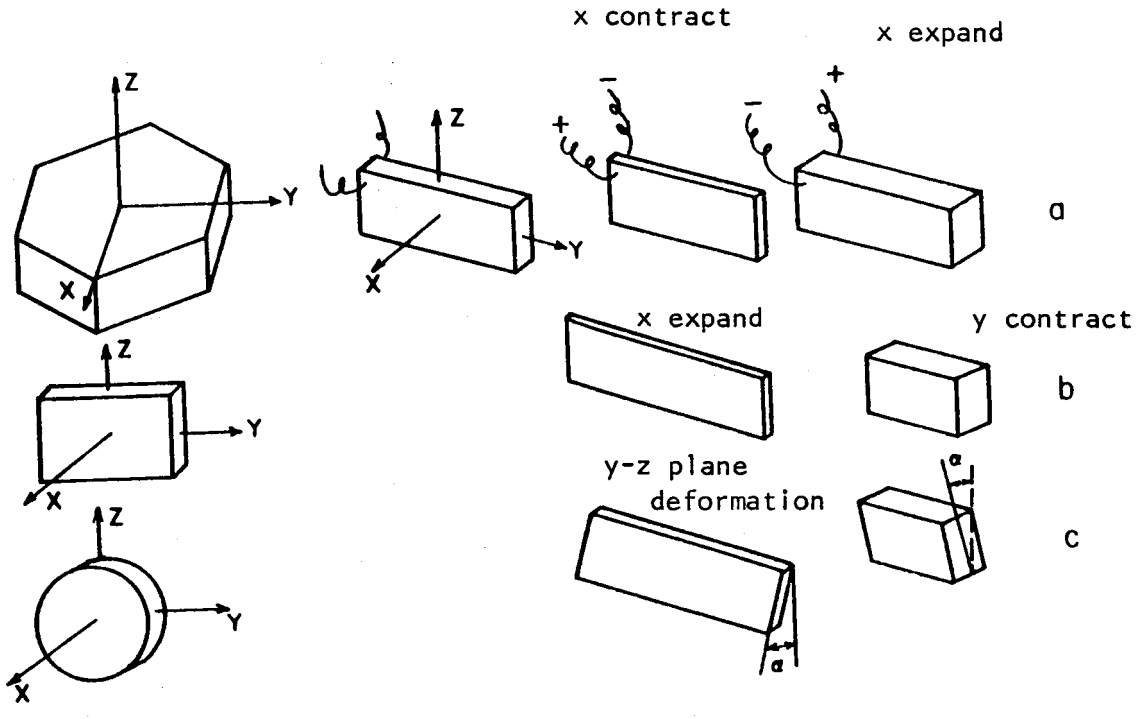

Fig. 3.6. Deformation of a x-cut quartz (a) change of thickness (b) with additional change in width (c) with additional shear (7)

This is because the particle motion produced by SH-waves is just horizontally polarized (x_3 plane) thus being incapable of producing elliptic motion of particles (x_1-x_2 plane), as required for Rayleigh waves (see Fig. 3.1).

The theoretical value of the efficiency of a Rayleigh wave wedge transducer is 81%, but the actual efficiency of these transducers is very low. Instead of using solid wedges, P-waves have been made incident at a critical angle in a water bath, into which the test material is placed. Fraser et al. (31) used this technique for making efficient, broadband transducers, and found a marked increase in efficiency as compared to Rayleigh waves generated by solid wedges.

A totally different method of generating surface waves uses interdigital transducers (32). These consist of two interpenetrating sets of electrodes deposited on a pieozoelectric substrate. These interdigital transducers were slightly modified for use in ultrasonic testing, by Morgan (25).

To get the maximum deformation for producing longitudinal waves from the piezoelectric plate, the plate is excited at its natural frequency, which depends on the plate thickness. When the crystal resonates, standing waves are produced so that the thickness equals half the wavelength. Hence the plate thickness d is

$$d = \frac{\lambda}{2} = \frac{c}{2f} \tag{3.11}$$

where c is the velocity of the longitudinal waves in quartz, λ is

the wavelength and f, the excitation frequency. Equation (3.11) can also be written as

$$f = \frac{c}{2d} \tag{3.12}$$

Knowing the velocity of longitudinal wave in the crystal, and expressing d in mm

$$f_{\ell} = \frac{2.88}{d} \text{ M Hz} \tag{3.13}$$

The characteristic frequency for transverse waves is found as

$$f_t = \frac{1.92}{d} \text{ M Hz} \tag{3.14}$$

Modes higher than the natural frequency can be produced with frequencies equal to 3, 5, 7,. . . times the characteristic frequency, as standing waves occur corresponding to these wavelengths. The characteristic frequency is generated by applying an electric potential of the same frequency.

Since different applications require probes with different frequencies, it is necessary that the pulser-receiver, which is connected to the probe, generate the particular resonant frequency of the probe. The resonant frequency is achieved by incorporating the circuit elements, particularly the coil, in the probe which when connected to the pulser-receiver generates the resonant frequency.

A probe can either act as a transmitter or a receiver. Very often both functions are combined so that a single probe can be used both as a transmitter and a receiver.

When the plate in a transducer is excited by a pulse at its resonant frequency, the oscillations produced do not resemble those

of the forcing potential. They are damped because the plate has inertia and is placed between two media, the backing material and the test material. Depending on the damping coefficient the oscillation of a plate decays faster or slower. The damping coefficient depends on the acoustic impendences of the materials between which the piezoelectric plate is placed. The damping coefficient, which is a measure of the decay of the amplitude of the plate when vibrating free, is particularly important in determining the shape of the pulse that is generated. It determines the bandwidth of the pulse. Low damping produces waves at maximum pressure, but of narrow bandwidth. For this reason the bandwidth is increased by increasing the damping coefficient.

For frequency analysis it is particularly important to have a broad frequency band. This is achieved by using a short excitation pulse on a highly damped transducer.

The effect of damping on the oscillations in a plate is shown in Fig. 3.7. On the application of the alternating voltage pulse (Fig. 3.7a), the amplitude of the oscillations builds up gradually and then decays in a similar fashion (Fig. 3.7b), if the damping is low. For high damping (Fig. 3.7c), the amplitude builds up and dies faster. Thus it is clear that damping changes the pulse shape, which effects the frequency bandwidth. Low damping produces a narrow frequency band, while high damping produces a broad frequency band.

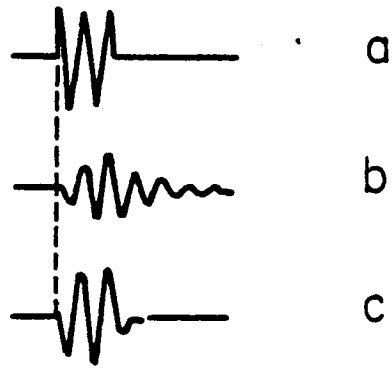

Fig. 3.7. Effect of damping on the oscillation of a plate (a) alternating voltage (b) oscillations of the plate at low damping and (2) high damping (7)

2. Sound field from a circular transmitter (7)

As the transducer vibrates on a test piece it transmits waves into the test material. Due to the effect of having a finite aperture these waves are not plane waves. The field changes considerably due to diffraction phenomena at the transducer edges. Plane waves generated near the center interfere with the cylindrical waves from the edges to produce a transmitted pressure field of maxima and minima. The last maxima as shown in Fig. 3.8 is located at a distance N from the transmitter along the axis of the transducer-beam. This distance N, known as the near field distance, can be found as

$$N = \frac{D^2 - \lambda^2}{4\lambda} \tag{3.15}$$

where D is the diameter of the transmitter. When the wavelength is small compared to the diameter, the near field distance can be written as

$$N \approx \frac{D^2}{4\lambda} \tag{3.16}$$

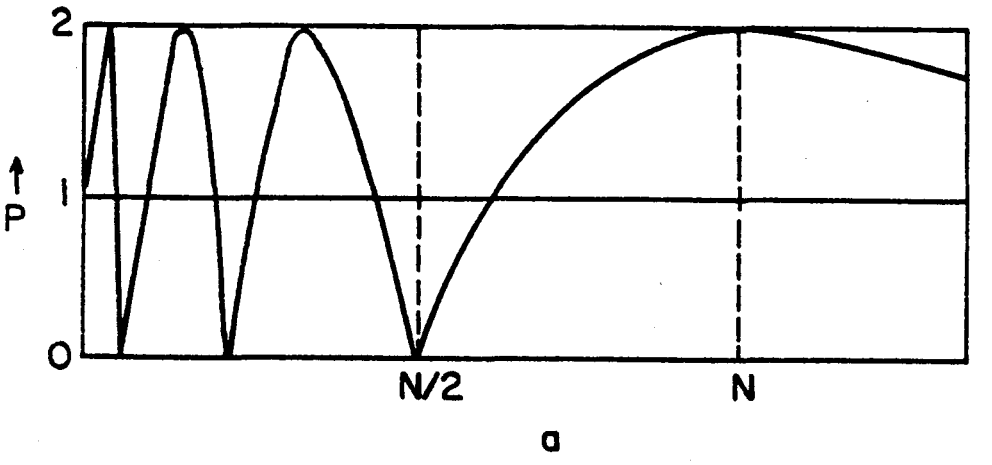

Fig. 3.8. Acoustic pressure on the axis of a transmitter (7)

The sound pressure, in the near field zone varies from zero to twice the mean pressure, Po. This effect in testing of materials, is however not so serious as the wavelengths present in the frequency band combine to produce a fairly uniform pressure field.

After the wave has traveled the distance N, it starts diverging i.e. the near field maxima starts widening. A set of secondary maxima and zero points are produced as shown in Fig. 3.9. The figure shows that the wave spreads at a certain angle which is found by joining the center point of the transmitter to the first zero point, at a distance of 3N from the transmitter. The angle of this line with the transmitter axis is known as the angle of divergence ν_o, which may be calculated from the theory of diffraction as:

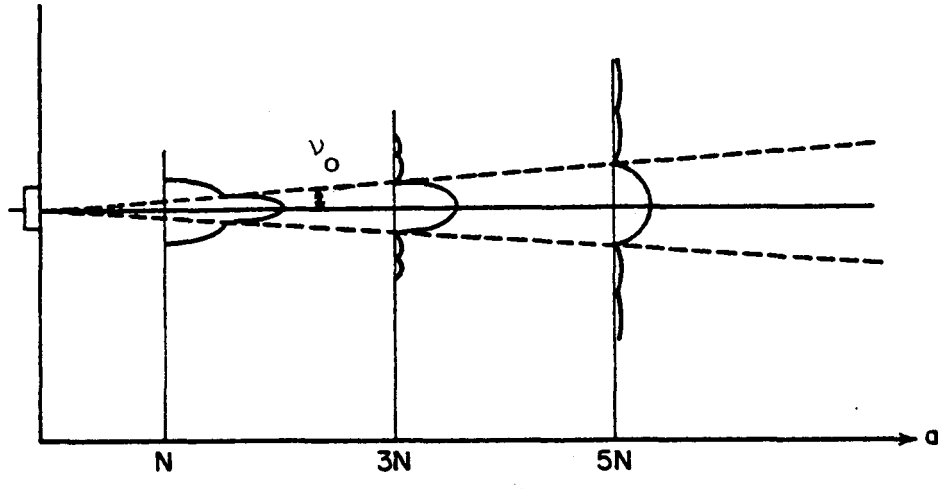

Fig. 3.9. Transition from near field for far field (7)

$$\sin \nu_o = 1.2 \frac{\lambda}{D} \tag{3.17}$$

Thus a small wavelength is required for a small angle of divergence. A large divergence angle causes a rapid fall in the pressure. The acoustic pressure in the far field at a distance 'a' from the transmitter is approximately equal to (7)

$$P \simeq Po \frac{\pi D^2}{4\lambda} \frac{1}{a} \tag{3.18}$$

Equation (3.18) clearly indicates that the pressure in the far field is directly proportional to the square of the diameter of the transmitter, and inversely proportional to the wavelength and the distance 'a'.

3. Effect of frequency on the testing of materials

The frequency of the wave and its corresponding wavelength have a dominating effect in ultrasonic testing of materials. In the last section it was shown that the acoustic pressure in the far field of a transducer is inversely proportional to the wavelength. Other phenomena which depend on the wavelength of the wave include grain boundary scattering and material absorption, as well as diffraction of waves from a flaw. Typically, the wavelength of ultrasonic waves used for testing is in the order of millimeters.

The reflection from a flaw, or the echo from the flaw, is prominent if the wavelength is smaller than the size of the flaw. In this case, the flaw surface acts as a mirror and an intense echo is reflected back. If the flaw is small compared to the wavelength, then the interaction of the wave with the flaw produces scattering of waves, and hence the echo is weak.

If the wavelength is too small, the rough surface of a flaw can produce scattering. If the difference in the height of irregularities of a rough surface is more than 1/3 the wavelength, scattering occurs and the surface doesn't act as a mirror. When the roughness increases to the order of a wavelength, the reflection disappers completely. This is possible on badly corroded surfaces and on cavities in castings.

Scattering is also produced within a material. Inhomogeneity in a material can be due to manufacturing defects such as porosity in sintered materials, and non metallic inclusions or pores in forging. It can also be due to the presence of different grains, as in cast

iron, which have different acoustic impendences and cause scattering. The presence of different crystallites of different structure, such as in steel and brass, also cause inhomogeneity. The orientation and the size of the grains effect the transmission significantly.

Scatter from the grains in polycrystalline materials increases approximately as the third power of the grain size and becomes significant, when the grain size is greater than a tenth of the wave length. That is, the scatter from grains increases as the wave length decreases.

Another effect which is to be considered for transmission of waves is absorption. This is due to direct conversion of sound energy into heat. Absorption also increases with the frequency of the waves.

In general, transverse waves attenuate more strongly than longitudinal waves, particularly in plastics. In the case of surface waves, the effect of the surface roughness is added to the attenuation. The high frequency components of the surface wave, which correspond to a smaller wavelength, attenuate much more at rough surfaces than the low frequency components.

Summarizing, the effect of frequency is as follows. With an increase in frequency

(1) the wavelength decreases

(2) the angle of divergence decreases

(3) the acoustic pressure along the axis in the far field decreases at a slower rate

(4) reflection or echo from a flaw increases

(5) the near field distance increases

(6) scattering from rough surfaces and grains increases

(7) absorption of waves increases

Thus, a compromise is to be made when choosing a frequency by considering the various factors above.

C. Photoelastic Visualization

For photoelastic visualization, it is recommended to use a birefringent model material whose acoustic and elastic properties are as near as possible to those of the actual prototype material, i.e. steel or aluminum. For this to be satisfied, the preferred model materials will be quartz or glass. (P-wave bulk velocity in glass = c_L = 5.66 x 10^3 m/sec.) The wave speeds in these materials are so high and the wavelengths so small that in order to "freeze" the wave motion extremely short exposure times (about 25-50 ns) are required. Photoelastic visualization in glass and quartz has been done by Hall (22, 33, 34) for British Rail. His results have been mostly qualitative.

In the work reported here, the material chosen was Homalite-100, because of its good dynamic photoelastic properties. The only draw back is that its acoustic and elastic properties differ considerably from the actual test piece material. However, it has a high fringe constant which allows better visualization of the secondary waves, the wave speeds are much slower (c_L = 2.1 x 10^3 m/s in plate), and the wavelengths are longer so that exposure times of around 1 μs are sufficient.

A multiple-spark camera (Cranz-Schardin type Fig. 3.10), was used to get a sequence of pictures of the waves at different times. This technique was used by Burger and Riley (35) and Riley and Dally (36) to study the wave behavior in layered media. The camera can operate at a framing rate which can be varied in discrete steps from a 67,000 frames/sec to 810,000 frames/sec. The effective exposure time is around 0.6 microseconds.

1. Electrical circuitry of the camera

The camera (37) has sixteen pairs of spark gaps arranged in a 4 by 4 rectangular array. Each gap is 0.25 inches wide between 0.50 in diameter solid brass spheres. The circuit used to run the system is shown in Fig. 3.11. The energy required to discharge the spark gaps is accumulated in 0.05 μFD (20 KV-DC) capacitors (C_1, C_2, C_3. . .) each of which is connected to an electrode in the spark gap array. The inductances (L_1, L_2, L_3 . . .) are air wound and the winding, can be tapped at any of eight locations. The time between the discharging of the two pressure gaps, say G_1 and G_2, is a function of the C_2 L_2 C_3 loop. Hence varying the inductance changes the framing rate without changing the individual exposure times. The eight tap locations permit the selection of 28 different values of inductance to obtain 28 different framing rates.

The capacitors and the spark gaps are first charged to a positive potential of 15 KV by a 15 KV-DC (5mA) power supply. Then a 15 KV-DC pulse from a variable 1-20 KV-DC trigger module is applied to a third

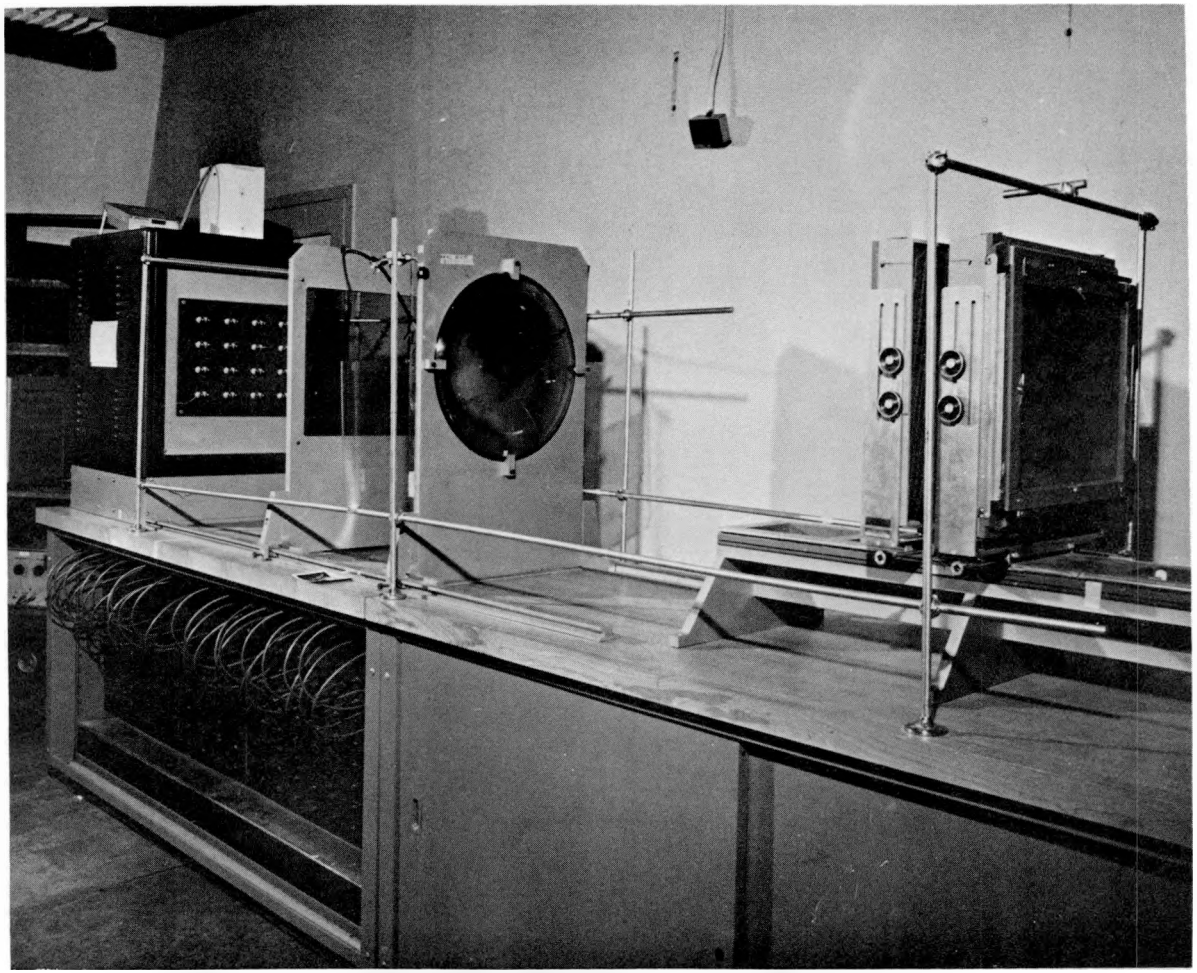

Fig. 3.10. Cranz-Schardin Camera

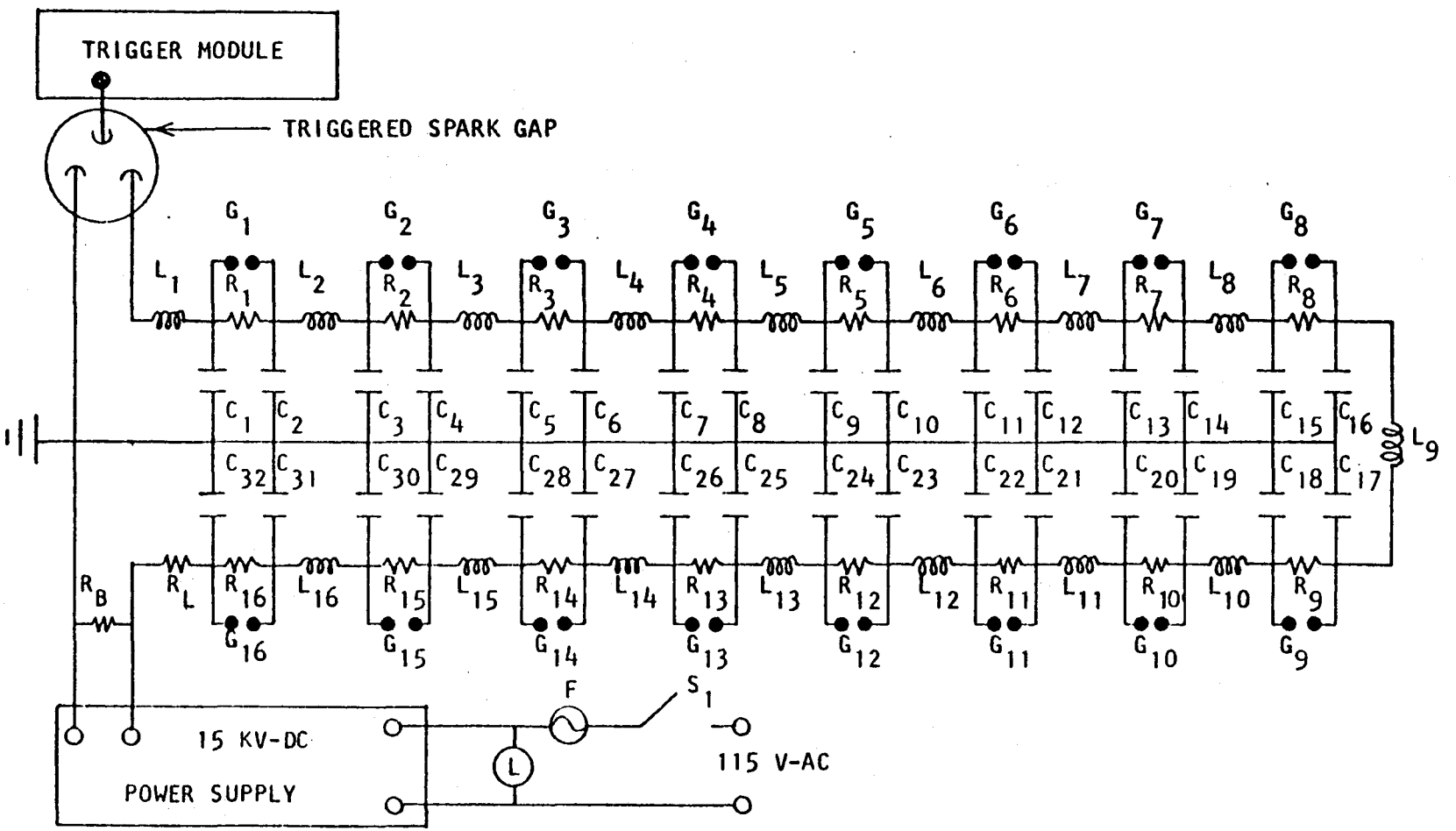

Fig. 3.11. The spark gap system circuit

electrode in a triggered spark gap. This closes the L_1 C_1 loop and initiates the firing sequence starting at G1. A sinusoidal voltage oscillation is induced in the C_2 L_2 C_3 loop as the positive potential of 15 KV-DC potential in C_3 decays to a negative 15 KV-DC. This causes a potential difference across G_2 of 30 KV-DC which ionizes the air between the spark gap to discharge the potential producing an intense light output. The sequence continues as a cascade through all 16 spark gaps after which the circuit is discharged through the 22.5 MΩ bleed resistor R_B.

2. Optical system

The optical system (Fig. 3.12) associated with the camera is capable of polarization and image separation. Since a sequence of pictures is required in a particular time, the sixteen spark gaps act as sixteen light sources and then sixteen images are finally obtained on the film plane. The light from the sparks first passes through the circular polaroid, after which the polarized light passes through the model, and another circular polaroid. It is then collected by a 16 inch diameter plano convex condensing lens (f = 20") which focuses the light from each spark into a separate lens on the lens board. Since each lens "sees" the light from only one spark it will record a distinct frame on the 14" x 11" film plane. There will be no interference or "shadow" from the other sparks.

The lenses have fixed apertures of f/4.5 and focal lengths of 7.5 inches. They are of high optical quality and are shown in Fig. 3.13.

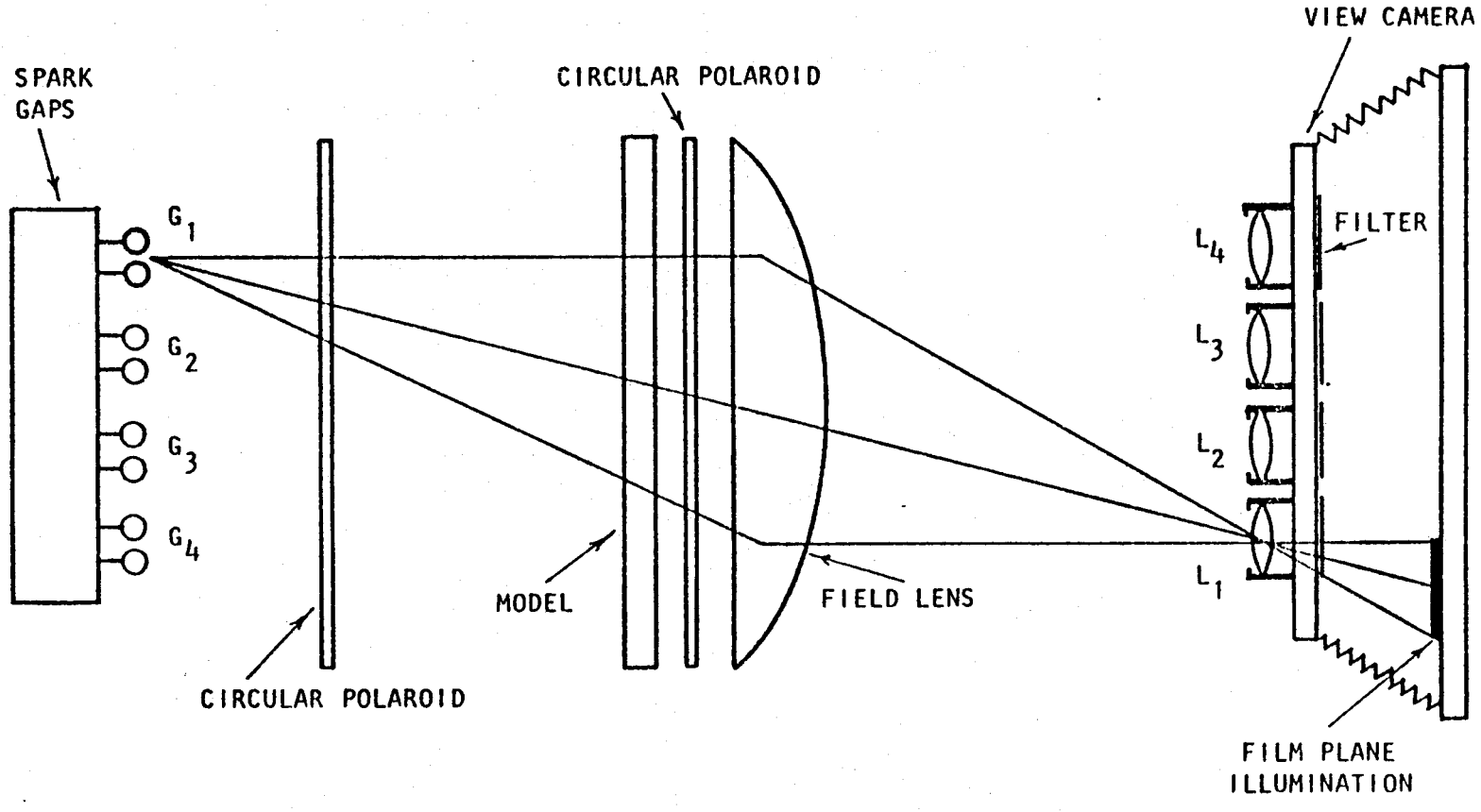

Fig. 3.12. The optical alignment of the system

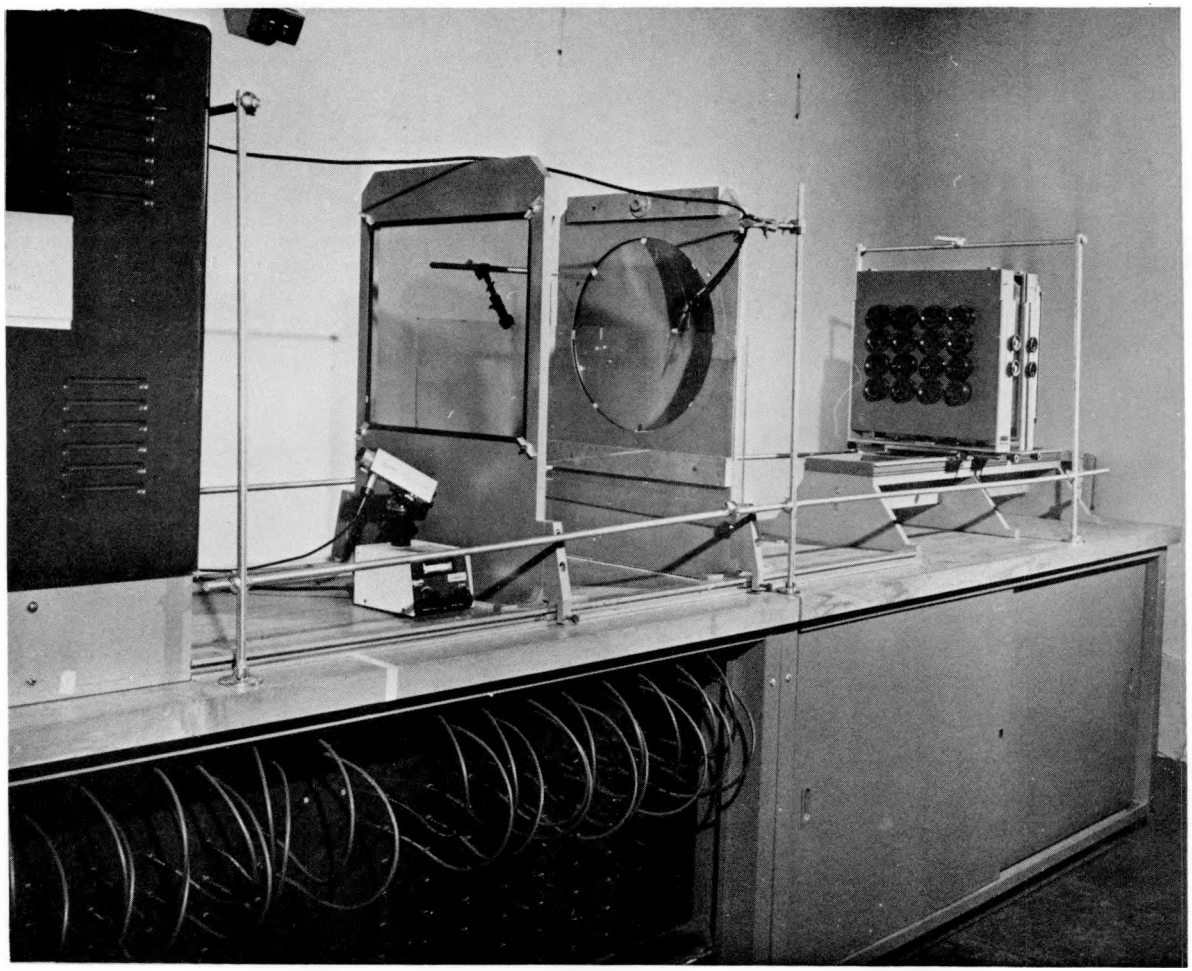

Fig. 3.13. Cranz-Schardin Camera

The system is primarily focused by adjusting the distance between the spark board, the field lens the lens board and the film plane. The field lens is not color-corrected which means that each wavelength will come to focus in a different plane. The image is, therefore, not sharp. This is taken care of by using sixteen 2 x 2 inch Wratten No 47-B filters which allow only a narrow band of light to pass. The particular filter allowed light to be passed in the blue region. The blue region is chosen because the blue light corresponds to the hottest temperature of the spark, and lasts for a short time (about 0.6 μsec). The large wavelengths are associated with the cooler emissions from the spark and, therefore, have longer duration of times. By filtering them out the effective exposure time is kept short. The film used was 14 x 11 inch color separation film Kodak Type 4133 which is sensitive to the blue region transmitted by the 47 B filters.

3. Control circuit

The basic function of the control circuit, is to explode the charge and to provide the necessary delay between the explosion and the trigger for the camera. This time delay depends on the distance between the charge and the point of interest on the model. The control circuit is shown in Fig. 3.14 and the hardware in Fig. 3.15. When the switch S of the detonation circuit is closed it puts a 2000 V pulse across a thin chrome alloy wire which is placed in the lead azide charge. The wire explodes and sets off the charge. Simultaneously a 20 V pulse from the detonation circuit triggers the delay circuit and the oscilloscope. The delayed pulse in turn triggers the camera ciruit. A

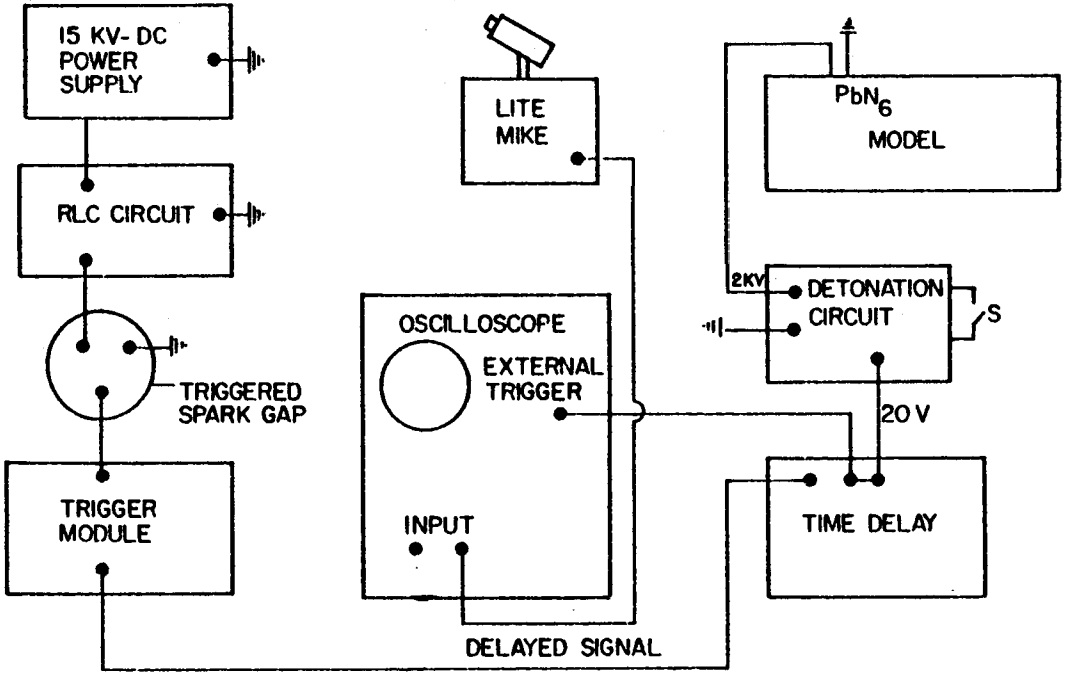

Fig. 3.14. Control Circuit

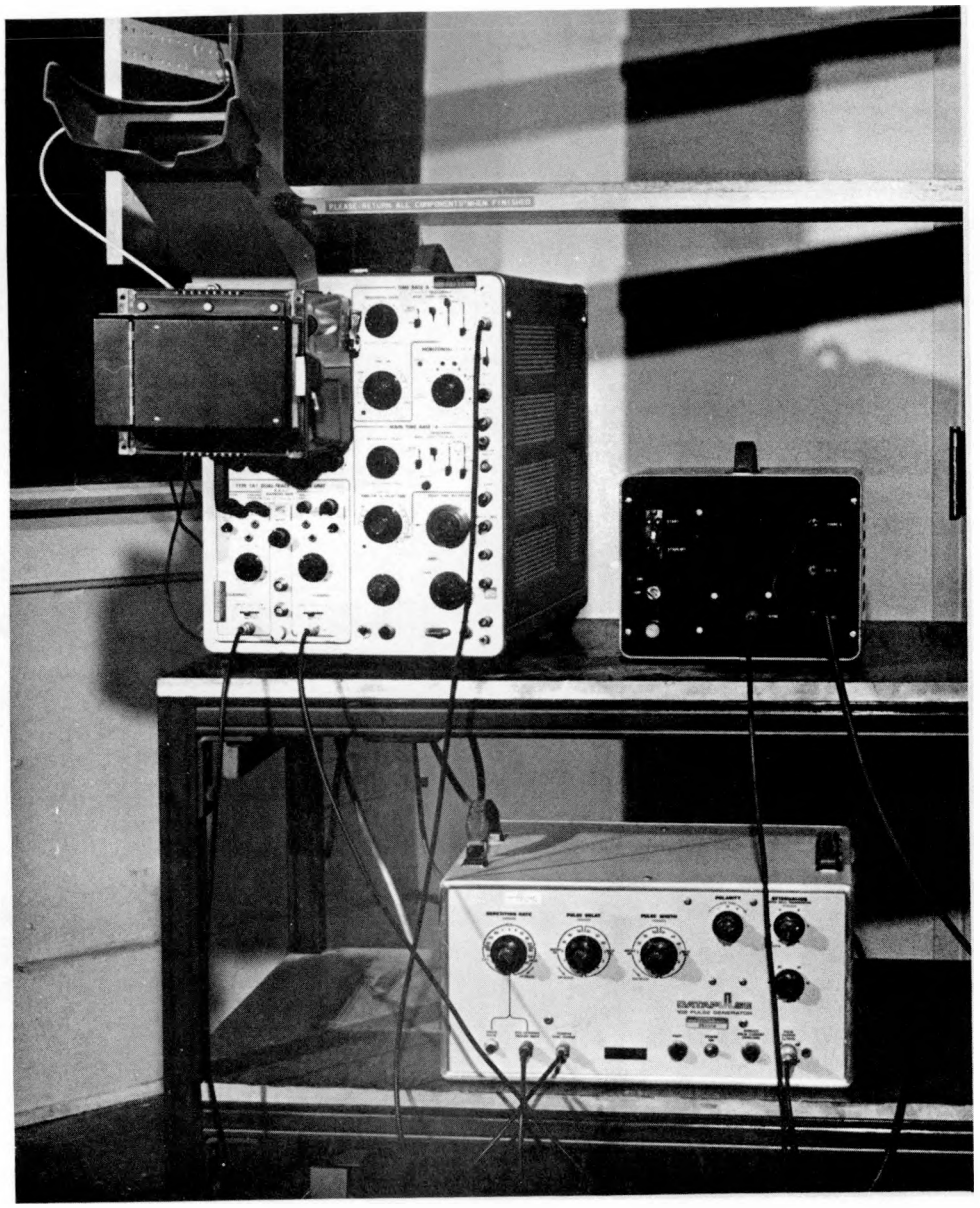

Fig. 3.15. Control circuit system

high frequency photodiode (EGG Lite-Mike) is used to sense the time sequence illumination from each gap. The output of the Lite-Mike is the input to the oscilloscope and is recorded on the screen as spikes along the fast running time base. A picture from the scope then gives the actual delay time including the camera delay and the actual delay between each spark.

4. Theoretical prediction of the stress field

The Rayleigh waves are generated on the surface by a suddenly applied concentrated load (29, 38, 39). For generating a sudden line load the explosive is filled in a tube which makes a line contact with the surface of the model. By theoretical analysis given in Ref. 39, a pattern of wavefronts is obtained as shown in Fig. 3.16. The

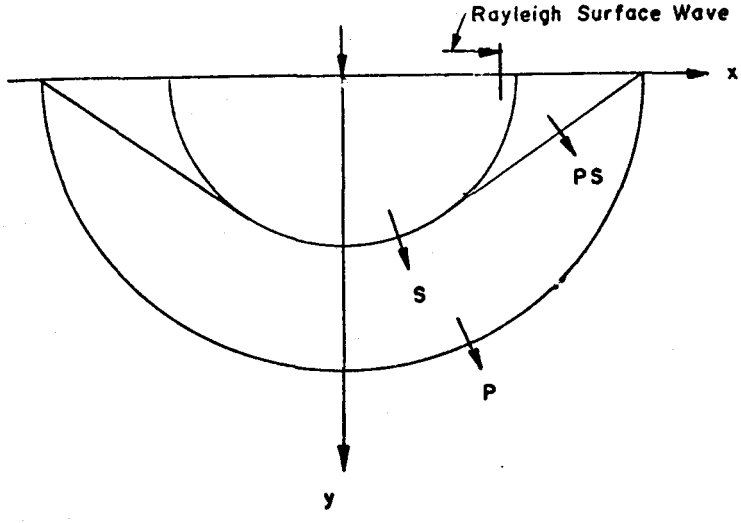

Fig. 3.16. Wavefronts generated by an impulse line source (39)

cylindrical P-wave travelling with a velocity c_L, leads all the waves as they travel outward from the point of disturbance. It is followed by the plane PS-wave (Von-Schmidt wave). The PS-wave is produced as the longitudinal waves cannot satisfy the boundary conditions of vanishing stresses at the free surface by themselves. Following the P and PS-waves are the cylindrical shear waves. From the theoretical analyses it is found that at $\theta = 0$ or π (on the free surface) a disturbance arises just behind the shear wavefront which propagates along the surface with the velocity of Rayleigh wave.

IV. DATA ACQUISITION AND ANALYSIS

A. Dynamic Photoelasticity

Dynamic photoelasticity provides full field two dimensional information on the propagation of elastic waves in sheets of birefringent material. Such information is valuable and was indeed, necessary in this research, for the insight that it provides in the ways in which waves interact with a slot.

The major drawback of current photoelastic techniques is that in order to provide sufficient resolution of the stress field it has to use highly birefringent model materials. These materials are all polymeric which means that they have very high attenuation for acoustic waves, low moduli, low density i.e. low acoustic impedance and wave speeds. The low modulus and high attenuation, renders standard ultrasonic transducers incapable of inducing stress waves of sufficient magnitude to provide useful fringe information. In this research, a rapid-burning explosive (lead-azide) was used to provide a sharp impulse wave. Such a wavefront, however, is not identical to the one derived from transducers.

Despite these disadvantages the information gained from photoelasticity was of great help in unraveling the mixture of transmitted, reflected, refracted, diffracted and mode converted waves received by the ultrasonic transducers after a pulse had interacted with a slot in a steel plate.

1. Preparation of model and generation of Rayleigh wave

The material chosen for the dynamic photoelasticity model was a 6.3 mm (1/4 inch) thick sheet of a polyester type of material marketed by SGL Homalite under the trade name of "Homalite 100." Its principal properties are listed in Table 4.1. Four plates with geometry shown in Fig. 4.1 but with four different slot depths were used as indicated in Table 4.2.

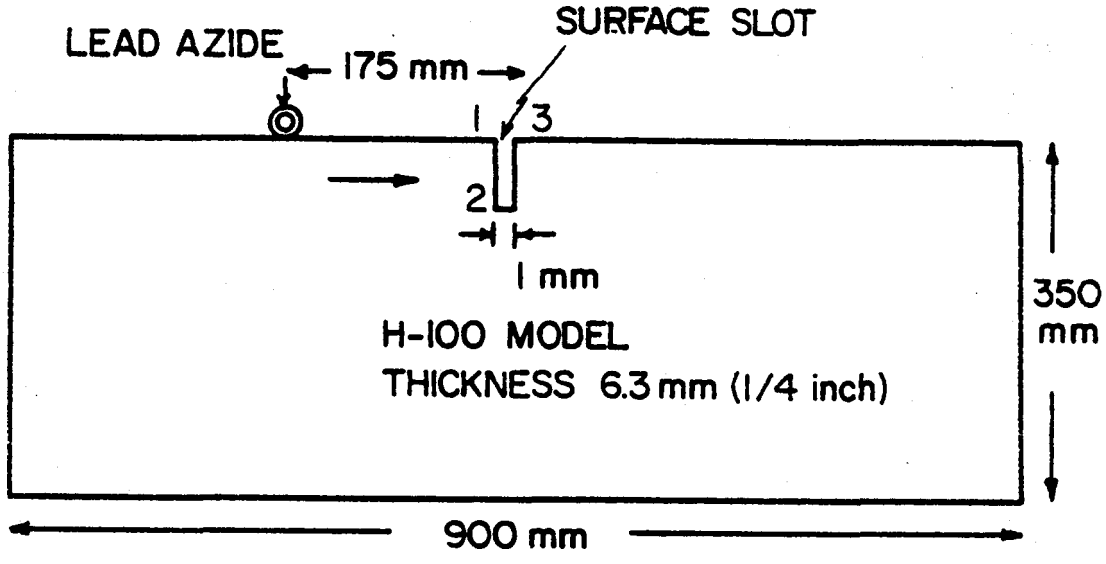

Fig. 4.1. Homalite - 100 model with a slot

The peak frequency of the input R-wave was 25 KHz which corresponds to a wavelength of 44.4 mm. This peak wavelength is found from the Rayleigh wave velocity, which is tabulated in Table 4.1, and a plot of the frequency components of the signal which are given later. Since the input R-wave has a broadband frequency spectrum (14 KHz to 110 KHz approximately).

Table 4.1. Principal properties of Homalite 100

Velocities in H-100 plate.		
Longitudinal wave	-	2.1×10^3 m/sec (83,000 in/sec)
Shear wave	-	1.22×10^3 m/sec (48,000 in/sec)
Rayleigh wave	-	1.11×10^3 m/sec (43,500 in/sec)
Elastic modulus (tensile)	-	2.4×10^9 N/m^2 (3.5×10^5 p.s.i)
(Compressive)	-	4.5×10^9 N/m^2 (6.5×10^5 p.s.i)
Specific gravity	-	1.23

Table 4.2. Depth of slots and the ratio of wavelengths to the principal dimensions

Model No.	Slot Depth (mm)	λ^* = 44.4mm for R-wave			λ = 10 mm			λ = 80 mm		
		$\frac{\lambda^*}{h}$	$\frac{\lambda^*}{t}$	$\frac{\lambda^*}{b}$	$\frac{\lambda}{h}$	$\frac{\lambda}{t}$	$\frac{\lambda}{b}$	$\frac{\lambda}{h}$	$\frac{\lambda}{t}$	$\frac{\lambda}{b}$
1	2.8	15.9	44.4	7.0	3.6	10	1.6	28.8	80	12.5
2	6.9	6.4	44.4	7.0	1.4	10	1.6	11.2	80	12.5
3	9.9	4.5	44.4	7.0	1.0	10	1.6	8.0	80	12.5
4	12.9	3.5	44.4	7.0	.8	10	1.6	6.4	80	12.5

b = plate thickness

h = slot depth

t = slot width - 1 mm

λ^* = wavelength of peak frequency amplitude i.e. at 25 KHz = 44.4 mm in Homalite 100

the wavelengths of the Fourier components vary from 10 mm to 80 mm about the peak value. The ratio of wavelength to the depth of slot is also shown in Table 4.2. A parametric study of the different effects of the four slots was used to find the ways in which changes in the frequency spectrum of the Rayleigh wave can be used to characterize the depths of the slots.

The R-wave was generated by exploding a small lead azide charge on the top edge of the plate. The explosive was packed into a tube, which was glued to the edge at a distance of approximately 175 mm from the slot. It was intended to approximate a line contact which would generate a cylindrical wave. The distance of 175 mm was chosen so that the reflected P-waves from the edge and the bottom of the plate would not interfere with the surface wave during the period of observation.

Taking zero time as corresponding to the time of detonation, the delay time between the detonation and the first picture, and the subsequent delay times between consecutive pictures were set so that information was acquired on the nature of the incident wave before the slot, on the wave interacting with the slot and on the transmitted and reflected waves after interaction with the slot.

Vertical grid lines were drawn every 20 mm, centered on the slot. Thus lines numbered "10" were 100 mm ahead and behind the slot. Figures 4.2 and 4.3 are composites of the 16 frames obtained for the shortest (2.8 mm) and largest (12.9 mm) slots. The time between sequential

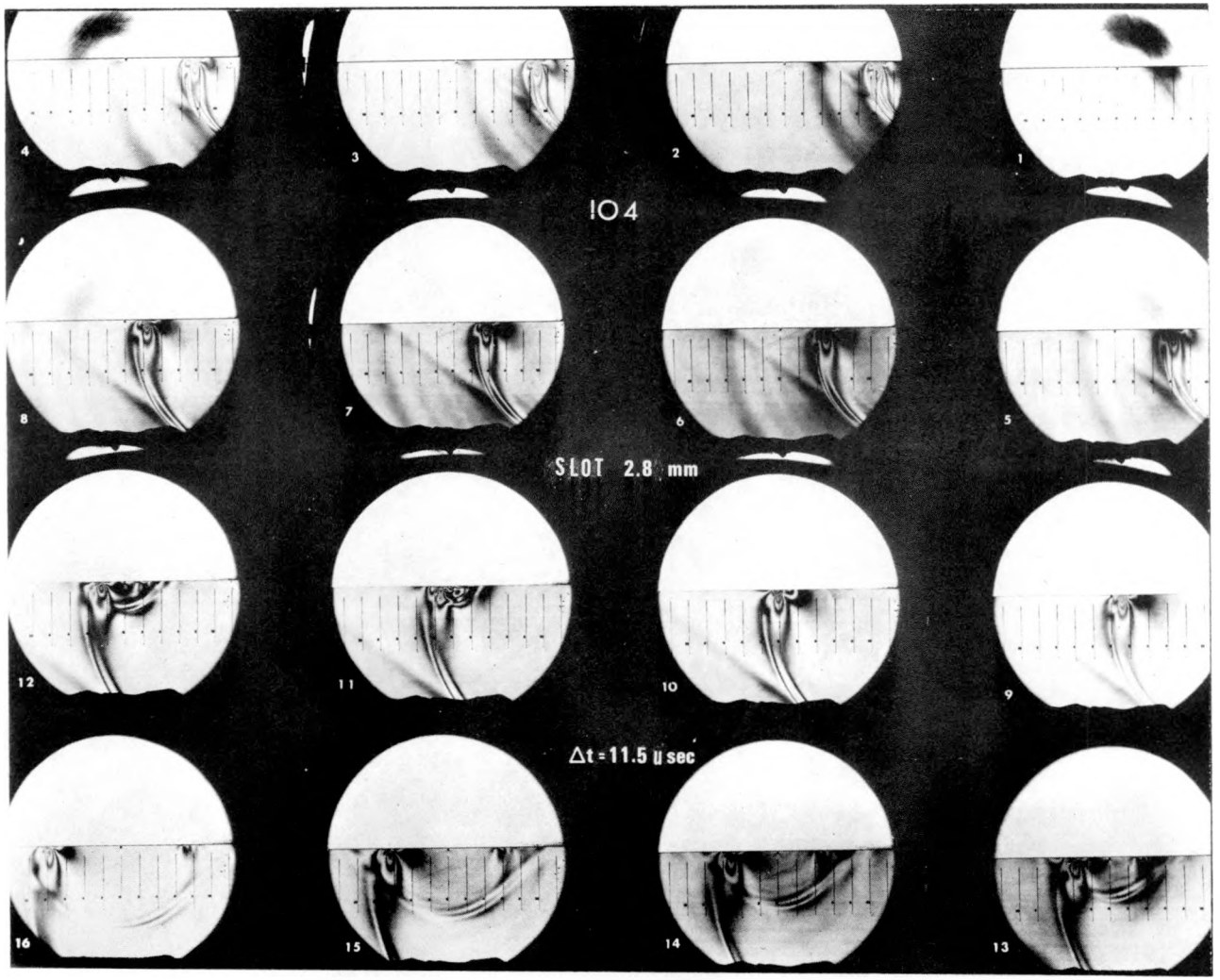

Fig. 4.2. Interaction of the input wavefronts with a 2.8 mm slot

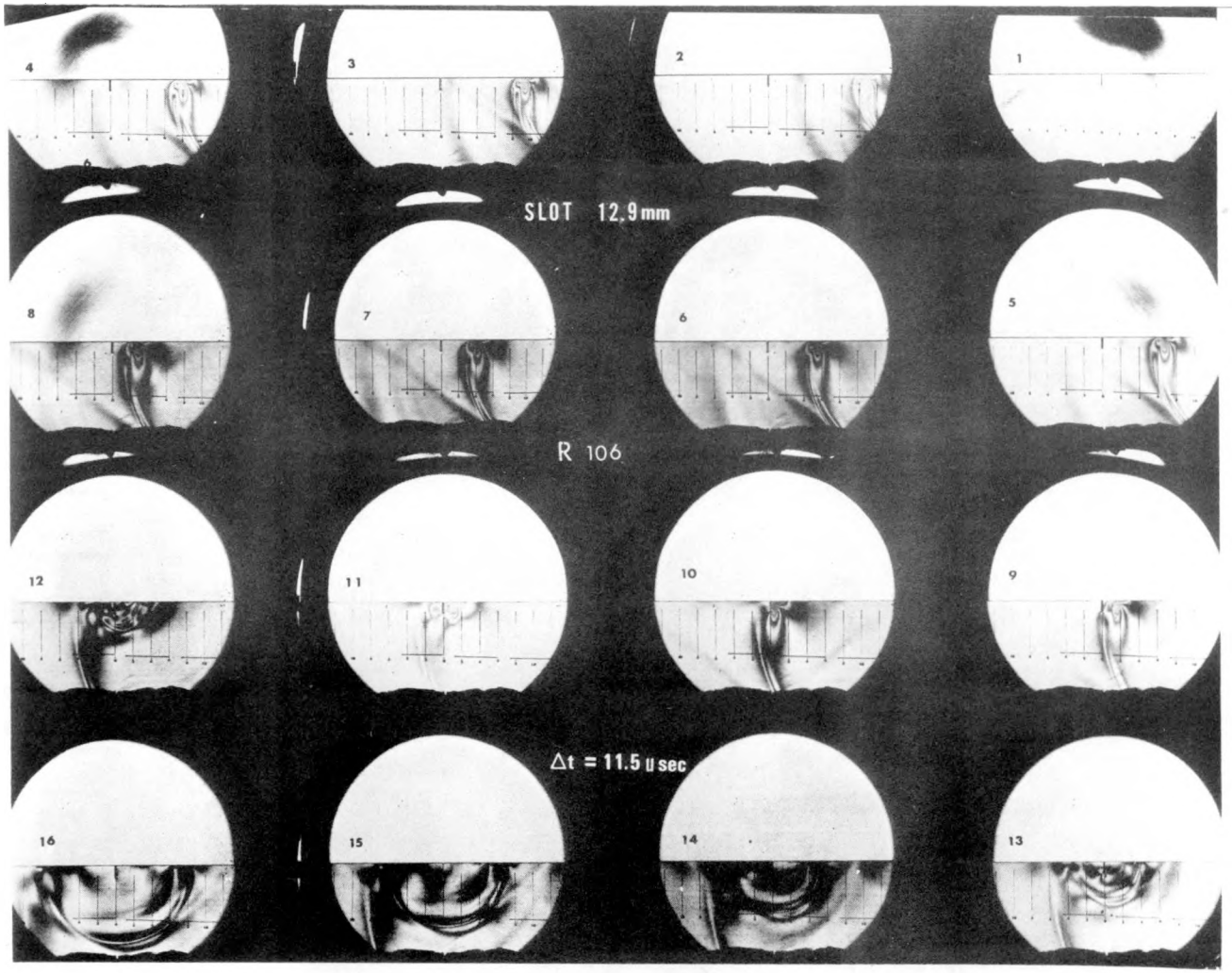

Fig. 4.3. Interaction of the input wavefronts with a 12.9 mm slot

pictures was 11.5 microseconds. The total event time represented by the 16 frames in a set was 173 μs.

In the 2nd, 3rd, and 4th frames of each composite, the P-wave can be clearly seen ahead of the S and R-waves. At these times the distance travelled by the P-wave is approximately twice that travelled by the S and R-waves. Also clearly seen is the Von-Schmidt or PS-wave. The input wave before it interacts with the slot is enlarged and shown in Fig. 4.4. These pictures verify the theoretical prediction of the waves generated by a suddenly applied line load (39).

2. Interaction of Rayleigh wave with a corner and the tip of a slot

A prerequisite for any analysis of the waves after their interaction with the slot, is a knowledge of the waves which are formed by mode conversion. The following notation was devised to indicate the various waves. A capital letter indicates the type of wave, P for longitudinal wave, S for shear wave, PS for Von-Schmidt wave and R for Rayleigh wave. A subscript indicates the original wave from which the mode converted wave (capital letter) was generated. A superscript identifies the point of origin on the model of reflected or mode converted waves. Another superscript differentiates between a reflected (r) or transmitted (t) component.

In this manner the notation S_R^1 indicates a shear wave formed by mode conversion of the original R-wave at the first upper corner of the slot, point 1 on Fig. 4.1. R^{2r} will be the Rayleigh wave reflected from the original R-wave at the slot tip (point 2).

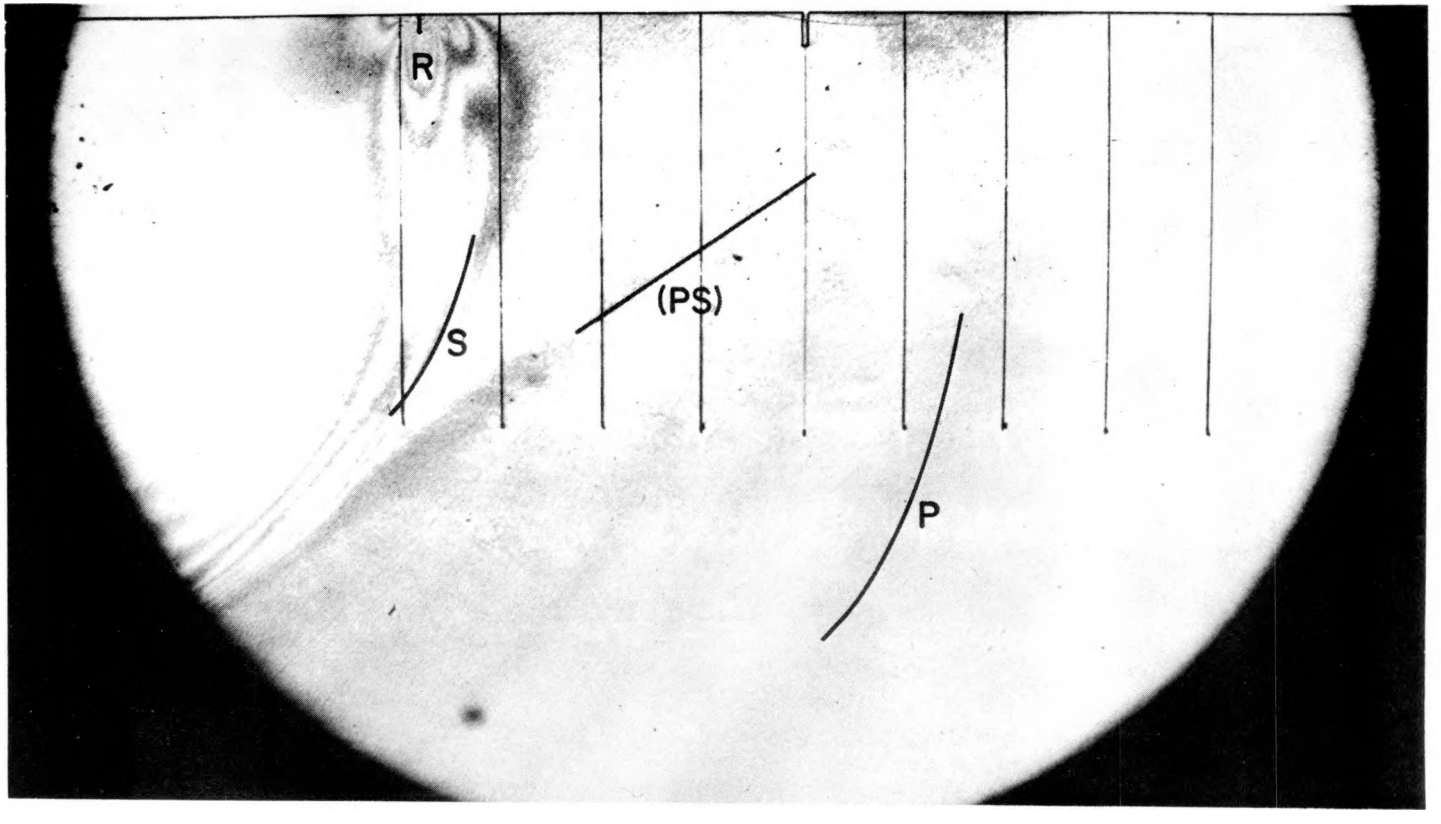

Fig. 4.4. Input wavefronts

The input from the detonation is shown indicating the various wavefronts in Fig. 4.5. The shear is mainly a SV-wave, i.e. it is 'ver-

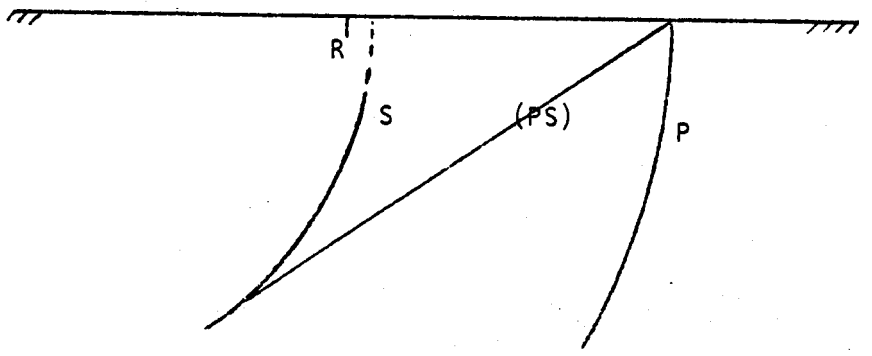

Fig. 4.5. Input wavefronts

tically polarized,' The 'horizontally polarized' component, or SH-wave, is absent. SH-waves have particle motion transverse to the plate which is not excited by the loading produced by the explosive. The SV-wave reduces to zero at the top surface on mode converting to a R-wave, as it travels along the surface. Its presence is felt in the interior away from the surface.

To understand the conversions more clearly two special models were used. In the first one the interaction of an input wave with a

rectangular corner, such as point 1 was studied with the aid of a model shown in Fig. 4.6. Since the input P wave travels far ahead

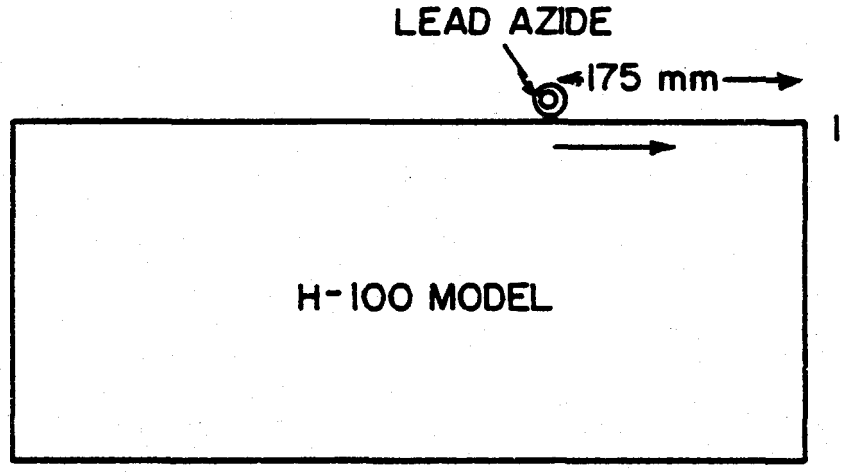

Fig. 4.6. Model used to study the interaction of input waves with a corner

of the S and R-waves its effect is not considered in the analysis and it does not show in the pictures. Fig. 4.7 is a sketch of the waves which are expected to be present shortly after a S and a R-wave had rounded a corner. The S-wave is reflected from the face as an S^r-wave. There is also a possibility that on reflection, S-wave mode converts to a P-wave. Since the P-wave travels 2.1/1.22 times faster than the S-wave in Homalite-100 plate, it is shown ahead of the S^r-wave as P_s^r. The R-wave on interaction with the corner 1 mode converts to a shear wave S_R^1 and a P-wave P_R^1. A (PS) wave is formed between the P_R^1 and S_R^1 wave

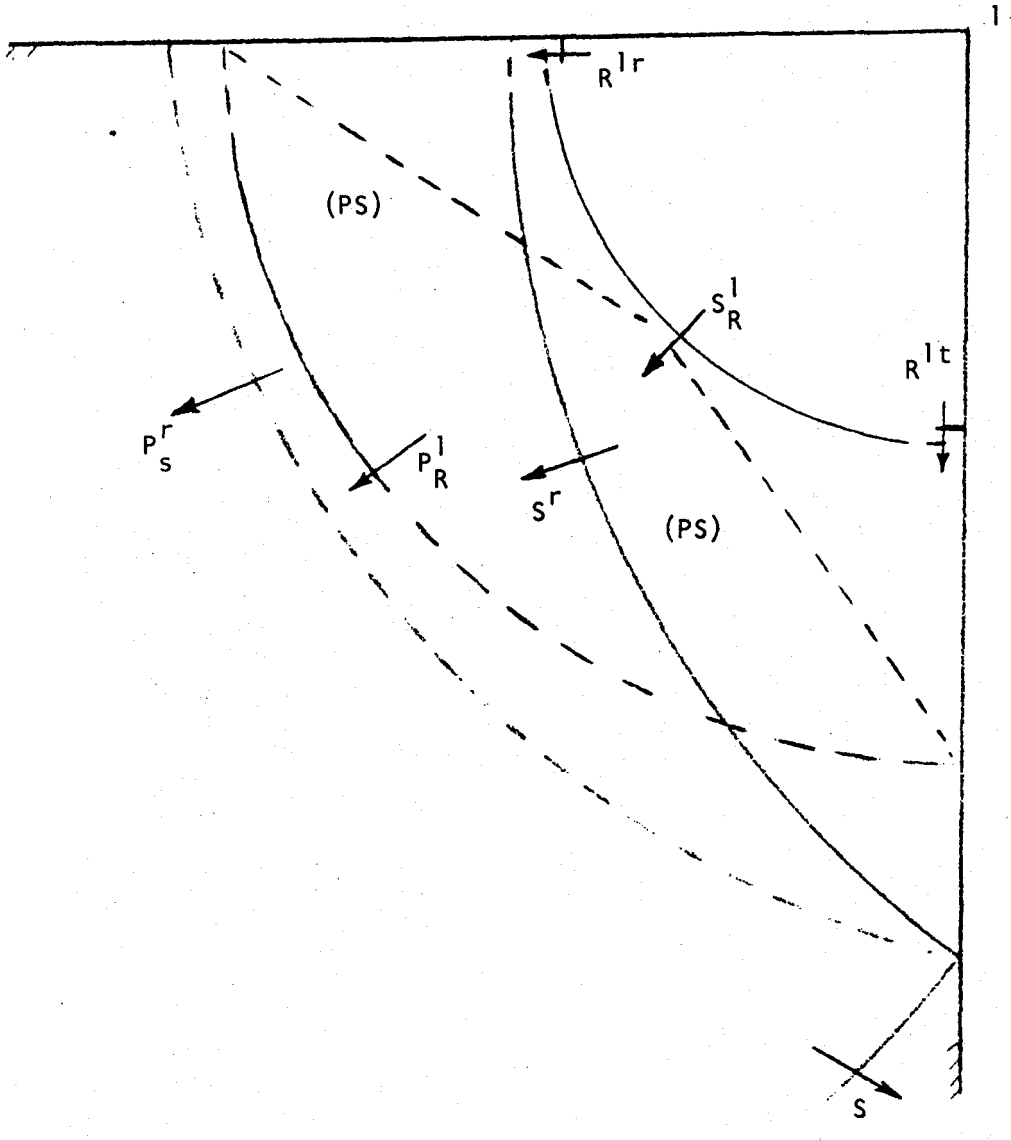

Fig. 4.7. Waves expected when an input wave interacts with a corner, (—) waves present in dynamic photoelasticity results, (--) waves absent in dynamic photoelasticity results

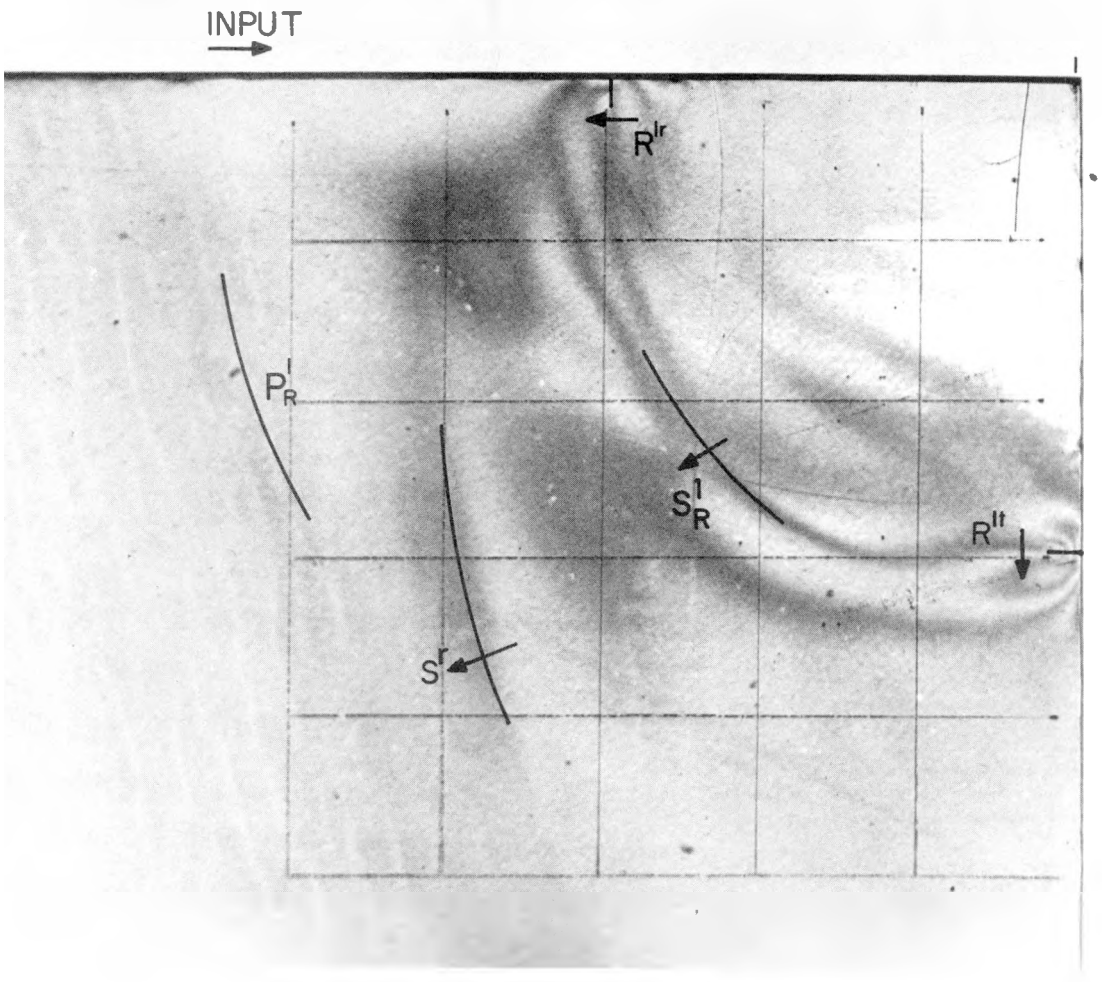

Fig. 4.8. Interaction of input wave with a corner

fronts. Part of the energy in the R-wave is also reflected as R^{lr}-wave transmitted as R^{lt}-wave. Fig. 4.8 shows the various waves as obtained by dynamic photoelasticity. The dark lines in Fig. 4.7 are the waves which are also present in Fig. 4.8. The waves represented by dotted lines cannot be identified on the photoelastic photographs. This may be because the waves corresponding to these lines are so weak that they do not produce half a fringe.

In the second model, shown in Fig. 4.9, mode conversions from a

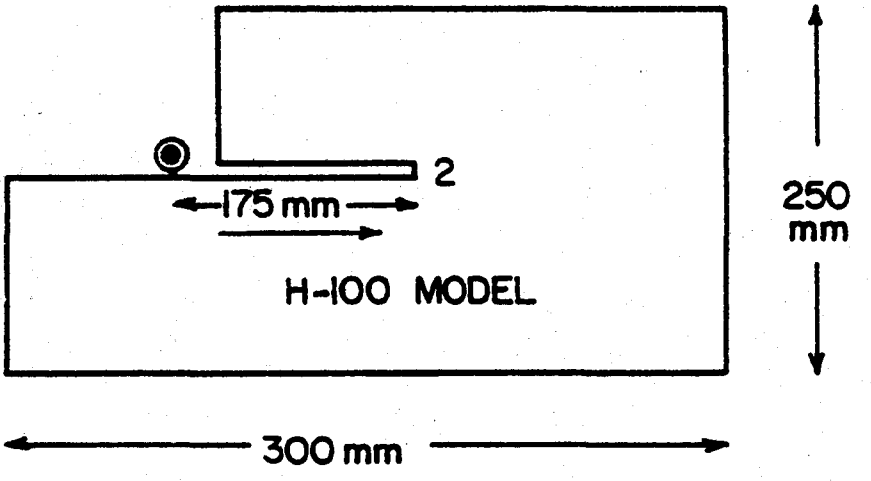

Fig. 4.9. Model used to study the effect of slot tip on the input wave

R-wave at the tip of a slot were studied. Fig. 4.10 shows the waves which will be expected from the interaction of the input S and R-waves. In this case the input shear wave is unaffected by the tip as it is not

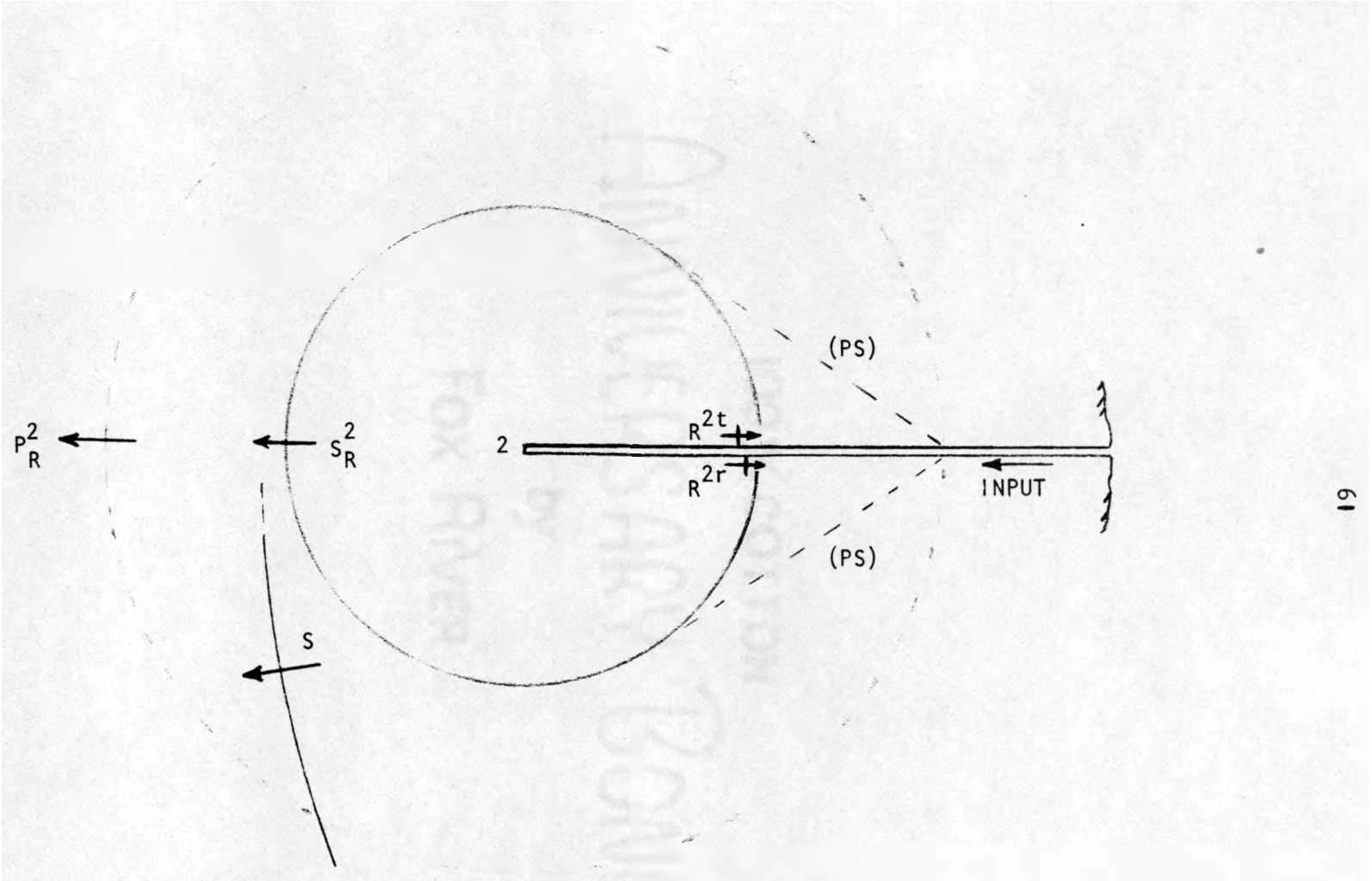

Fig. 4.10 Expected waves from a slot tip

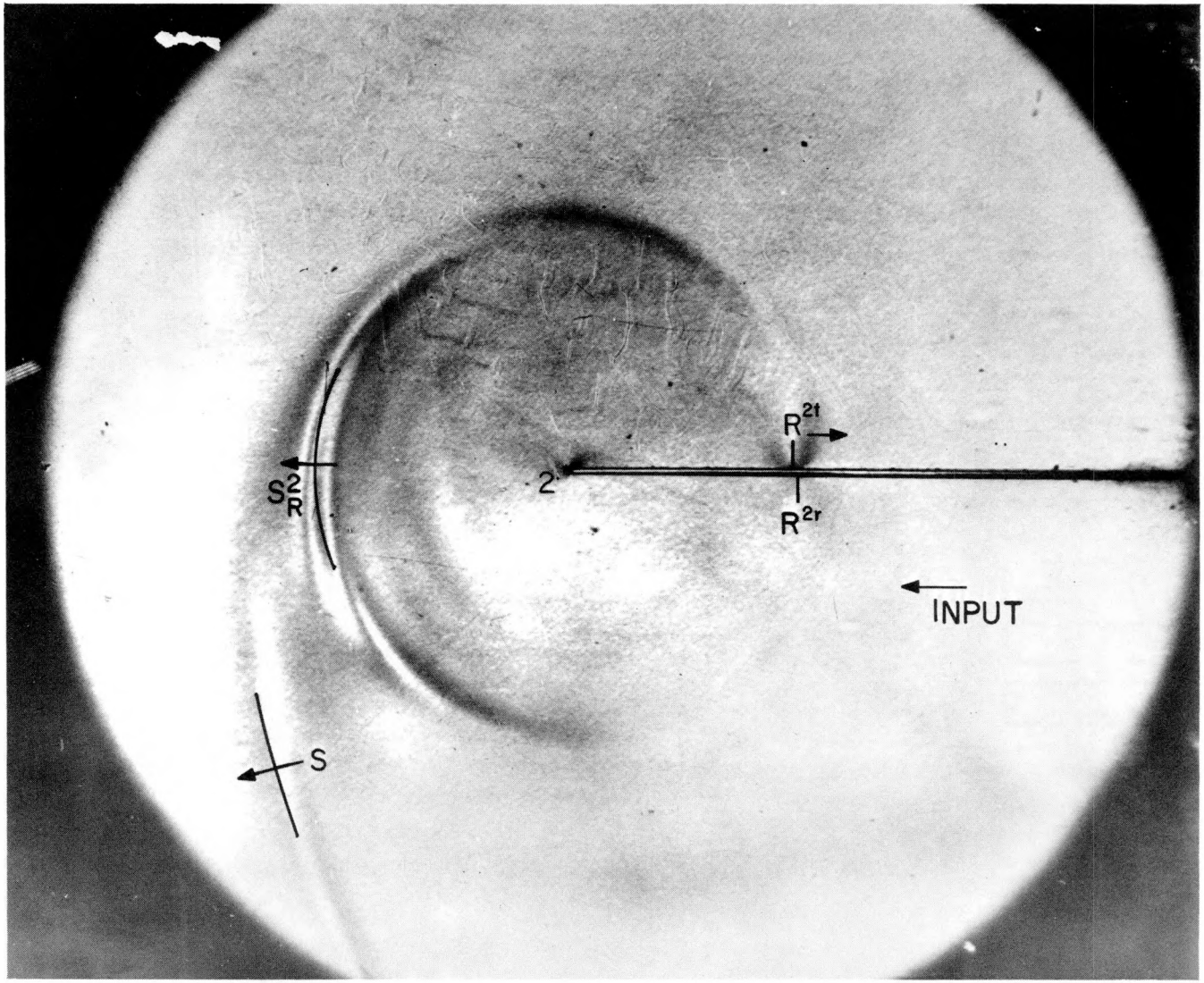

Fig. 4.11. Interaction of the input wave with a slot tip

present at the surface. The input R-wave is expected to shed a shear wave S_R^2 and a longitudinal wave P_R^2. Part of the R-wave will travel around the tip as R^{2t}. A small amount of energy will be reflected back as R^{2r}. Fig. 4.11 shows the waves by photoelasticity. It is seen that the P_R^2 is not present in Fig. 4.11. The reflected R^{2r}-wave is very weak and hard to see in the reproduction of Fig. 4.11. It was, however, evident in the original photograph.

3. Interaction of a Rayleigh wave with a slot

The wave pattern that originates from the interaction of input waves with a thin slot in a plate is shown in Fig. 4.12. This is the enlargement of frame 14 of Fig. 4.3 (12.9 mm slot). The important points at the slot are numbered 1, 2 and 3 as shown in the figure.

A frequency analysis of the input Rayleigh wave showed that the strongest frequency occurred at 25 KHz. This corresponds to a wavelength of 44.4 mm. It is known (29) that the particle motions that identifies with a Rayleigh wave penetrate to a depth of about 2 times the wavelength. The magnitude of the displacements, however, decay exponentially from the surface such that it can be neglected in terms of usefulness for NDE at depths greater than one wavelength. This can be seen in Fig. 4.4 where the fringe order at a depth of more than 44 mm, is less than one half ($N < 0.5$).

The photoelastic results show clearly that the pattern of mode conversions and the intensity of the various waves depend on the depth of the slot. The input S-wave is strong in the interior of the plate,

and reduces rapidly to zero at the surface. When it reaches the slot most of its energy passes undisturbed past the tip. The portion of the shear wave which strikes the face of the slot is reflected and the portion that strikes the tip will diffract. For short slots the diffracted shear is small since the incident S-wave, which is mainly SV is weak near the surface. Thus the incident shear wave striking the tip of short slots is weak. As the slot depth increases, the intensity of the shear wave striking the tip will increase. The strength of the diffracted shear wave will increase correspondingly. It will again start decreasing as the effect of the larger diffraction angle becomes significant. The diffracted shear will be present at the surface as it does not graze the surface but strikes at an angle.

Also seen in Fig. 4.12 are two longitudinal waves P^2 and P^{1-2}. It is not clear from which wave the two fronts P^2 and P^{1-2} are generated. The source for the former is point 2, and for the latter point 2 and/or the face 1-2.

The photoelastic picture (Fig. 4.12) could not resolve the existence of two waves, if they existed as such. The single notation P^{1-2} was used to indicate their position.

The interaction between the slot and the Rayleigh wave is the most interesting. It is known that the depth of the Rayleigh wave is a function of the wavelength. As the R-wave approaches the slot, it strikes it from the slot opening to the slot tip. The particle motion at the slot opening will contain all the Fourier components, i.e. all the wavelengths

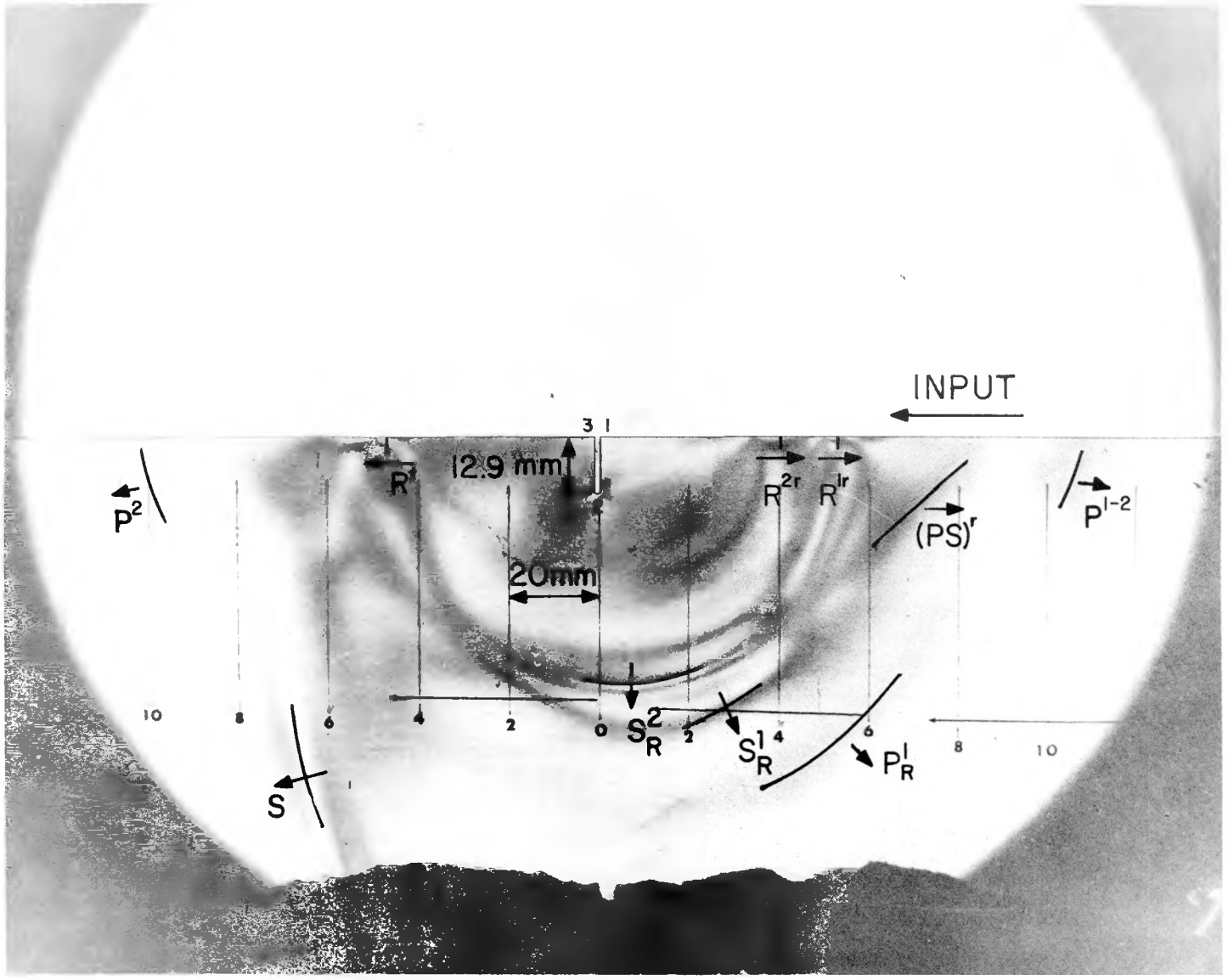

Fig. 4.12. Waves generated by the input wave when it interacts with a 12.9 mm slot

of the input wave. The particle motion at the tip will be mainly due to the long wavelength parts of the R-wave.

The interaction of the upper portion of the wave with the slot opening (point 1) is similar to the earlier discussion of the interaction of an R-wave with a corner. A R^{1r}-wave is reflected, a shear wave, S_R^1, is produced by mode conversion from the R-wave at point 1, and a transmitted Rayleigh wave turns around the corner and continues down the front face of the slot to the tip. Here a portion of the R-wave mode converts to a shear wave S_R^2, another portion is reflected back up the front face as R^{2r} and the remainder proceeds around the tip and up the face of the slot.

The deeper particle motion of the R-wave will interact with the slot differently. The energy distribution in the Rayleigh wave as it interacts with the slot is sketched approximately in Fig. 4.13. The figure shows that the deeper particle motion (corresponding to the long wavelengths) goes under the slot and forms another Rayleigh wave, called here an "undercut" R-wave. The deeper particle motion will also form a shear wave at the slot tip which will scatter from the tip. The transmitted signal called R^t in Fig. (4.14) is a composite of all the R and S-waves diffracted from the crack tip, including the shear wave which is scattered from the tip due to the incident shear wave. The shear wave is present in the transmitted response at the surface, because unlike the input S-wave, it does not graze the surface but strikes at an angle.

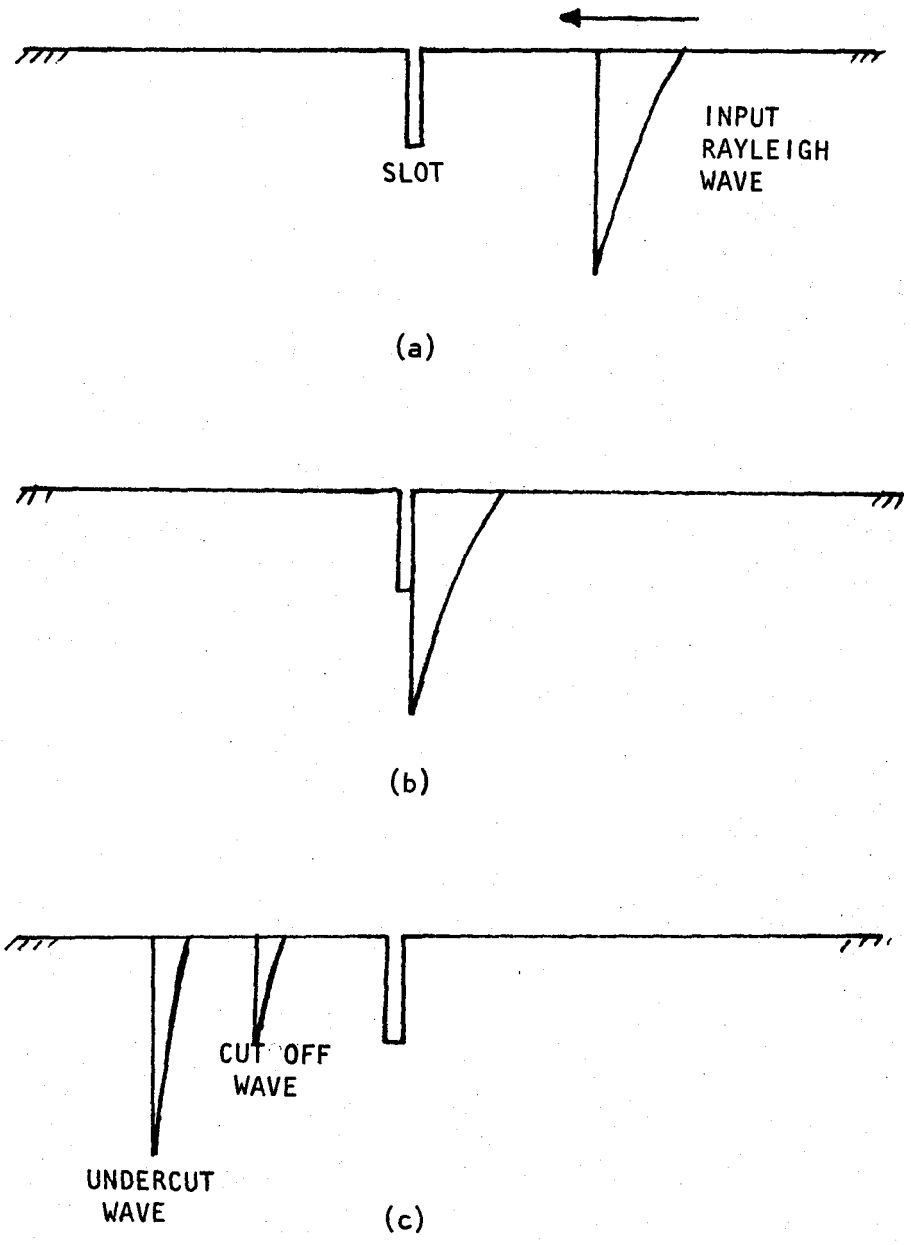

Fig. 4.13. Formation of the cut off and undercut Rayleigh waves (the figure does not show other mode converted and reflected waves)

The fringe order of the transmitted wave at the surface gives the stresses at the surface. Plotting these gives the shape of the wave (Fig. 4.14). Since the slot depth affects the cut-off level, the shape of the R^t-wave will change with the depth of the slot (Fig. 4.15).

The results on the waves formed on interaction with the slot are in good agreement with Bond and Ilan (15, 40) who studied the interaction of Rayleigh waves with a slot by using finite difference techniques (Fig. 4.16). His results have all the waves except P^{1-2} and P^2. It is thus possible that these are not generated by the R-wave, but by the input S-wave which is absent in Bond's analysis. Thus comparing the two results, it is found that dynamic photoelasticity is indeed very useful in finding the interaction of waves with discontinuities in a two dimensional medium.

4. Frequency analysis of transmitted wave from photoelasticity data

The frequency of the transmitted wave is analyzed, since it contains the undercut (deeper part) R-wave, whose frequency depends on the depth of the slot. Thus it is possible that the frequency spectrum of the transmitted wave has sufficient information to size the crack.

In Fig. 4.14 the photoelastic fringe orders are plotted, along the top surface of the plate, for the waves after interaction with the

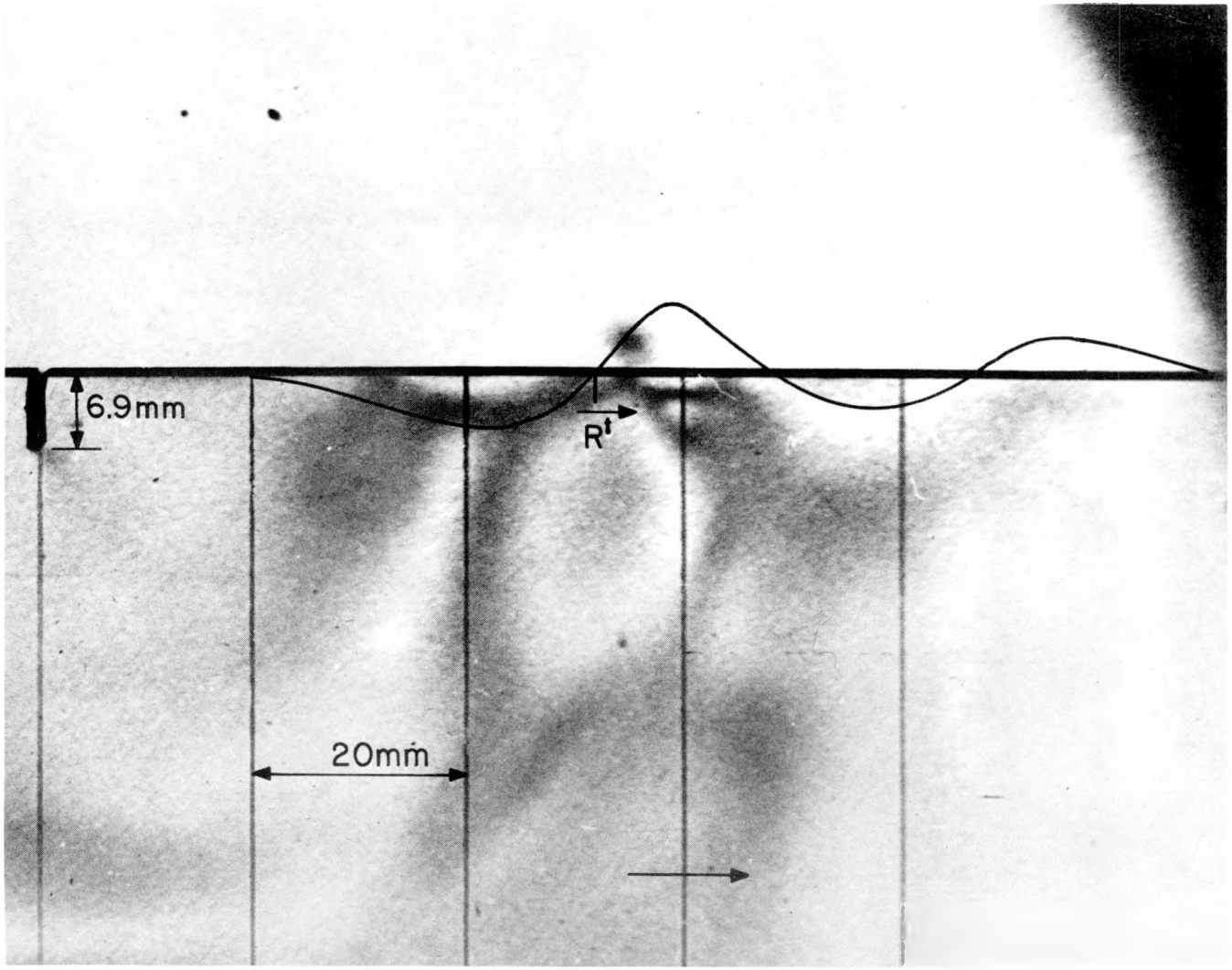

Fig. 4.14. Transmitted wave

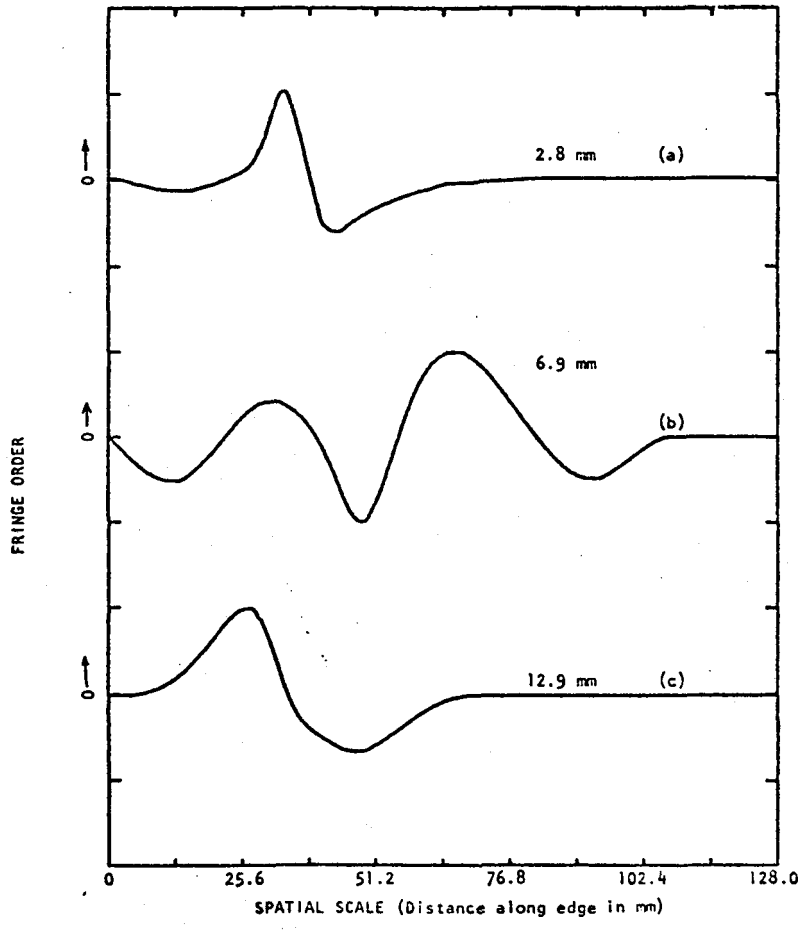

Fig. 4.15. Transmitted waves, (a) slot depth = 2.8 mm, scale 1 div = 3 fringes (b) slot depth = 6.9 mm, scale 1 div = 1 fringe (c) slot depth = 12.9 mm, scale 1 div = 1 fringe

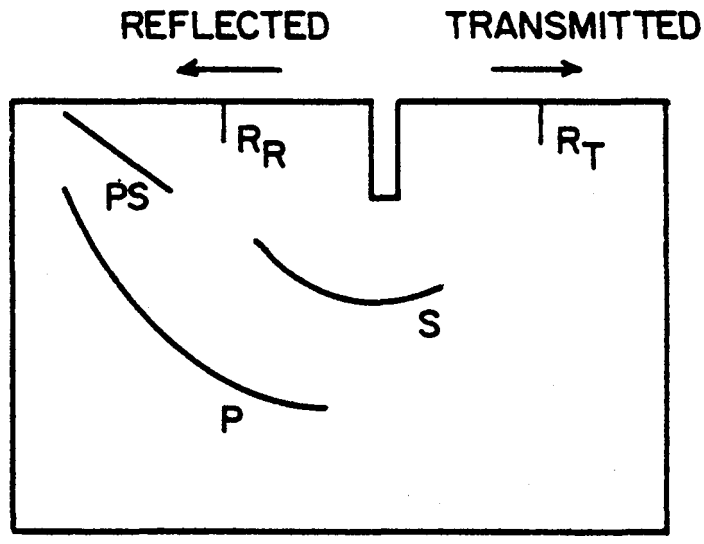

Fig. 4.16. Waves predicted by Bond and Ilan (15, 40) finite difference analysis

slot. The only stress possible on a free boundary is a normal stress tangential to the boundary (Fig. 4.17). The fringe order is propor-

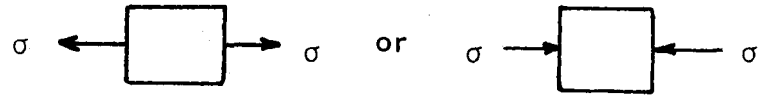

Fig. 4.17. Normal stress tangential to the boundary

tional to the stress on the boundary i.e.

$$N = \sigma_t b/2f_\sigma$$

$$\text{or } \sigma_t \propto N$$

where N = fringe order

σ_t = tangential stress

f_σ = fringe constant

b = plate thickness.

For the purpose of this research it was not necessary to compute the actual values of σ_t, since it is directly proportional to the fringe order along the boundary.

The curve in Fig. 4.14, therefore, represents the amplitude of the stress wave along the surface. The position of the picture in the field of the plate was chosen to show the "transmitted" R-waves, plus whatever other waves happen to be clustered in the same region at the time of observation.

The variation of the fringe order with distance along the surface (the spatial fringe distribution) was digitized by hand and entered into the mini-computer system which is described later. A curve fitting routine was used to fit a cubic spline through these points (see Fig. 4.18). This wave was then read automatically to give the adjusted fringe orders at equal increments of 0.25 mm, along the boundary. The fringe orders at these incremental points defines the wave very well. They are then taken as the input for a Fast Fourier Transform (FFT) program, which was written for the computer system. The FFT of the

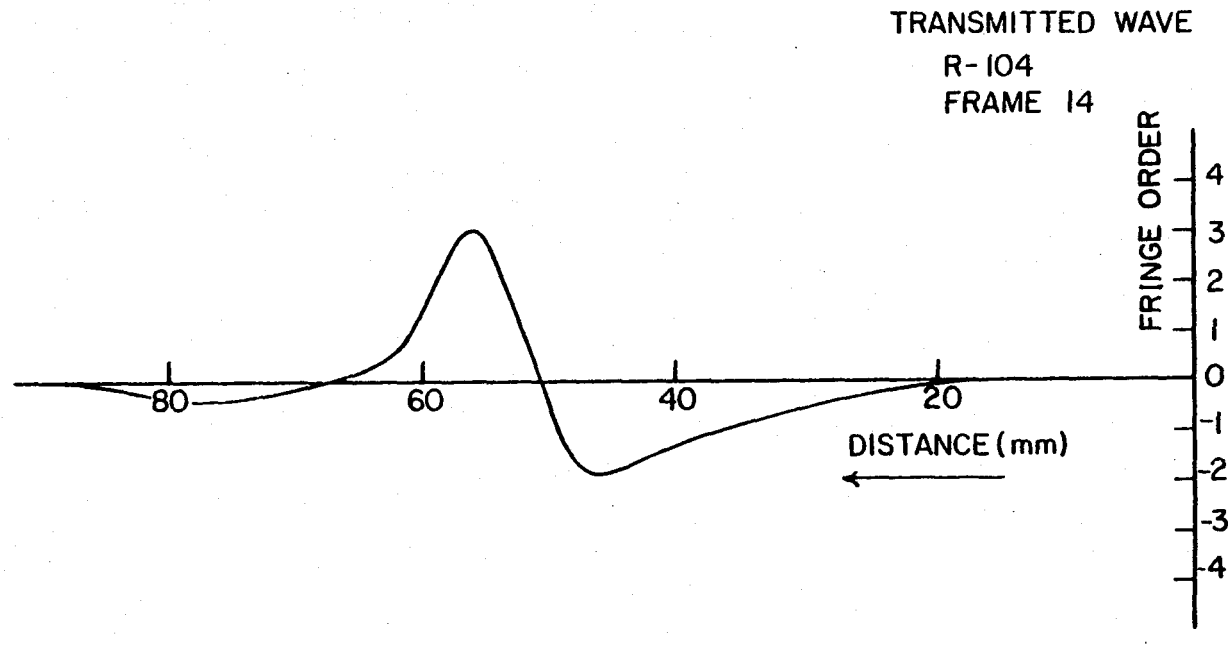

Fig. 4.18. Cubic spline fit of the transmitted wave for a 2.8 mm slot (distance shown is from the slot)

signal contains both the real and the imaginary components of frequency. Both components are added vectorially to obtain the magnitude of the frequency, or the frequency spectrum. This information is plotted as the output of the program. Fig. 4.19 (see next page) shows the magnitude of the spatial frequency distribution for the transmitted waves from each of the four slots. The spatial frequency is plotted as the transmitted wave is a mixture of S and R-waves which travel at different velocities and it is not possible to convert the spatial plot of Fig. 4.19 to a single equivalent time scale. There are significant differences in the frequency spectrums. For the shortest slot (2.8 mm), the spectrum is quite similar to that of the input wave (Fig. 4.20), with some modulations. This is possibly due to resonances of the faces of the slot. As the slot depth is increased to 6.9 mm, the high frequency content drops, while the low frequency content remains strong.

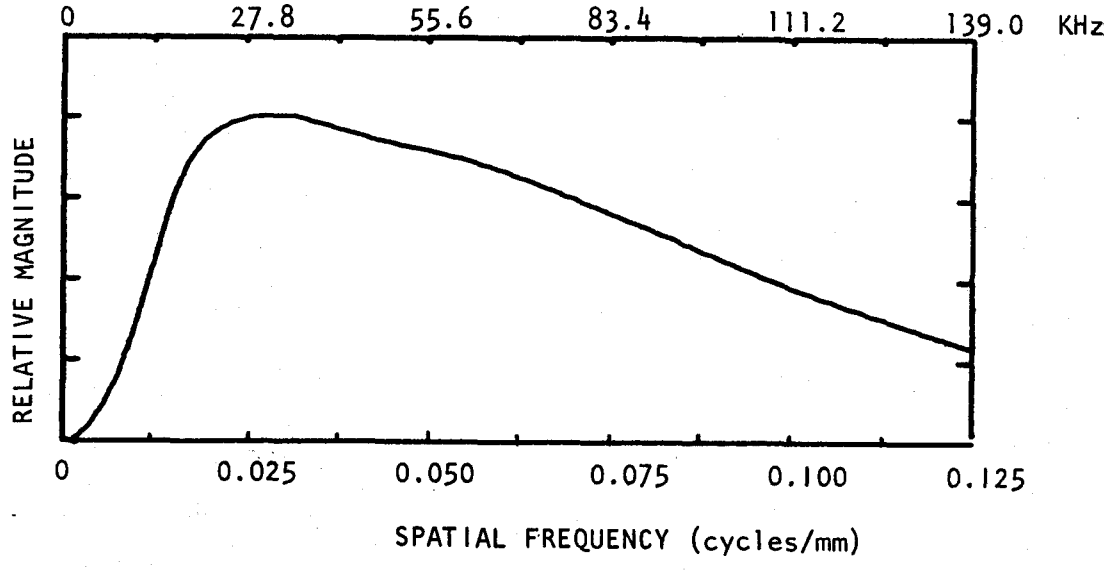

Fig. 4.20. Frequency magnitude of the input R-wave for 2.8 mm slot

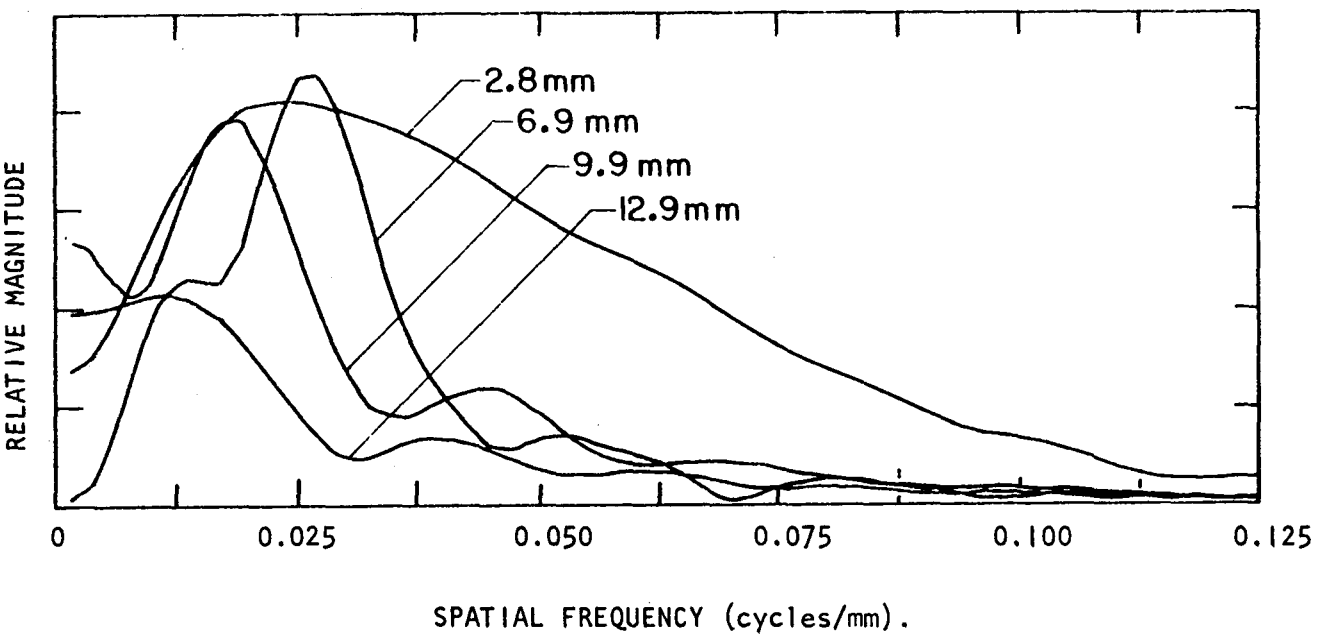

Fig. 4.19. Frequency magnitude curves for four different slots

Since the depth of the R-wave depends on the wavelength, the portion of the wave which extends beyond the slot tip will pass, and form the undercut R-wave and a mode converted S-wave. The upper part of the R-wave which is "cut off" becomes very weak as it goes around the slot and loses significant energy into reflected R-waves and mode converted waves. It is to be noted that this cut off part was the one which mainly contained the high frequency components. The portion of this wave which is transmitted around the slot to appear as part of the transmitted R-wave on the far side of the slot will have greatly reduced amplitude. Since this wave contains the high frequency components, the high frequency portion of the transmitted spectrum will be weak. On the other hand, the undercut R-wave contains the low frequency content which remains strong in the transmitted wave. This argument holds true until the depth of the slot becomes so great that there is no significant undercutting. The shear wave which is formed by the deeper particle motion will also be of low frequency as it is formed by low frequency components (deeper portion) of the R-wave. With the increase in the slot depth the input R-wave is sliced at a lower level which is the long wavelength region.

Thus the depth of the slot significantly affects the formation of the waves at the tip. The wavelength (frequency spectrum) of these waves, will be related to the wavelengths of the input R-wave, which exists at the tip. Since the depth of the R-wave is directly proportional to the wavelength, the frequency spectrum of the waves generated at the slot tip should be a function of the depth.

B. Ultrasonic Testing

In the last section dynamic photoelasticity was used to obtain qualitative information on the way in which a notch changes the characteristics of input Rayleigh waves. The results indicated that as a notch gets deeper, the high frequency components in the transmitted Rayleigh wave will be progressively attenuated. This was attributed to the property of the R-wave according to which its shorter wavelength (high frequency) components stay close to the surface. The longer wavelengths produce the deeper waves. Thus a slot will act as a low pass filter by cutting of the short wavelength (shallow) components while allowing the long wavelength (deep) waves to pass underneath the tip. The deep portion of the wave that passes underneath the slot forms the "undercut" wave, and also scatters as a shear wave from the tip. The frequency spectrum of these waves (waves from the deeper portion of the R-wave) contain the low frequency (long wavelength) components of the incident wave. It is, therefore, reasonable to suggest that the wavelength at which the frequency of the transmitted wave is "cut off" will be the frequency at which the wavelength relates to the depth of the slot. If this is true the frequency spectrum of the transmitted wave will give quantitative information on the depth of surface slot.

A ultrasonic test was devised to test this hypothesis.

1. Transducers

The transducers used for the ultrasonic testing were 5MHz, broadband, R-wave wedge transducers designed for use on steel. These trans-

ducers transmit a wide frequency spectrum, which is a requirement for the method of frequency analysis used here. The test requires that the incident wave should have wavelengths that will excite particle motions up to a distance from the surface which is deeper than the slot. When a transmitter and receiver were placed on the steel block, they recorded an input wave. The magnitude vs frequency of this input wave is shown in Fig. 4.21. This is a good broadband signal with a frequency variation from 1 to 5 MHz corresponding to wavelengths from 3 to 0.6 mm. The models were steel blocks, with 0.43 mm wide, machined slots, which were 1, 2, 3, 4 and 5 mm deep. These depths were selected because theory (39) predicts that the elliptical particle motion of a R wave penetrates to a depth of 2λ. Thus a wavelength of 3 mm will excite particle motion as deep as 6 mm. It was anticipated, that the maximum depth to which this analysis would work, would be 5 mm. Beyond 6 mm there should not be any undercut wave.

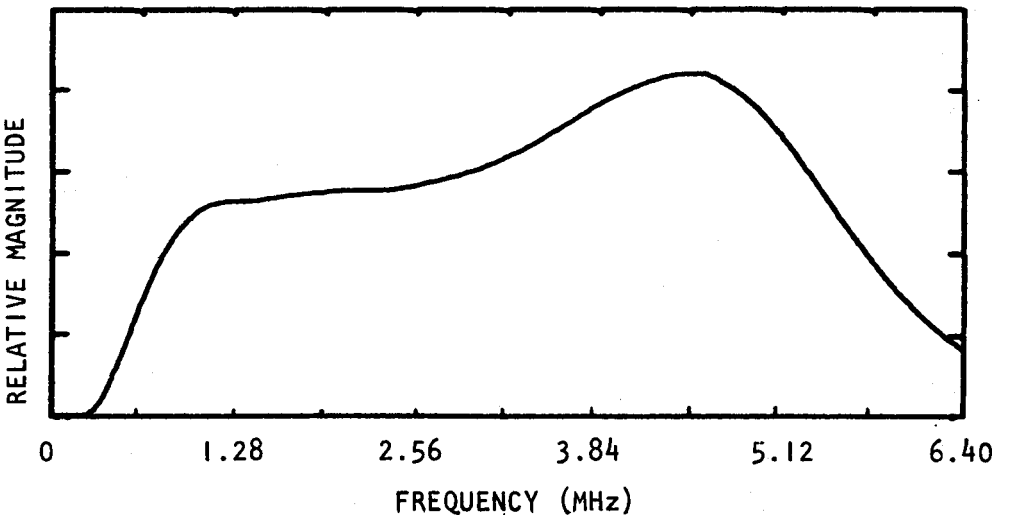

Fig. 4.21. Input frequency magnitude of the ultrasonic R-wave

The piezoelectric plates used in these transducers is 1/2 inch diameter P-wave plates. The transducer plate is placed on a lucite wedge, which is cut in such a way that after crossing the interface into the steel, the refracted shear wave in the steel will transmit along the surface, i.e. the wedge is designed so that the incident P-wave strikes the steel surface at a critical angle of incidence. When a vertically polarized shear wave is made to travel along a surface, it mode converts to a R-wave. If the angle of incidence is less than the critical angle, the shear wave is refracted into the steel i.e. the angle of refraction is less than 90°, and the wave travels into steel as a shear wave. It was mentioned in Chapter III (page 33) that transducers have a divergence angle $\nu_o = \text{Sin}^{-1} (1.2 \frac{\lambda}{D})$. Some of the waves emitted from the transducer into the wedge are, therefore, not normal to the plate of the transducer. Some of these P-waves are incident at the steel surface at less than the critical angle and will produce shear waves, which travel into the steel block at an angle less than 90°. The divergence angle for the particular transducers of a frequency of 5 MHz was 3.5°. At 1 MHz the angle was of 18°. Thus in addition to the R-wave there will also be a shear wave present in the steel. The shear wave will be pure SV as the particle motion induced by the incident P-wave is incapable of generating SH-waves. At the surface, the SV-wave will have mode converted fully to form the incident R-wave. As the angle from the surface increases the SV-wave will start

showing its presence in the interior. When the angle from the surface is increased still further, the shear wave will decrease because of the rapid drop off in power as one moves out of the transducer beam beyond the divergence angle of 18°. Thus it is seen the shear wave, is not present at the surface but builds up in amplitude with an increase in angle from the surface. At deeper penetrations (larger angle) the shear wave decreases again. The input wave in front of these transducers is shown in Fig. 4.22. These wave fronts are quite similar to that of dynamic photoelasticity, except that, in addition to the S and R-waves, dynamic photoelasticity had P and PS wave fronts.

The velocity of the shear waves in the steel block was found to be 3.21×10^3 m/sec, and the velocity of Rayleigh wave was 3.00×10^3 m/sec. The wavelengths of shear and Rayleigh waves in steel correspond-

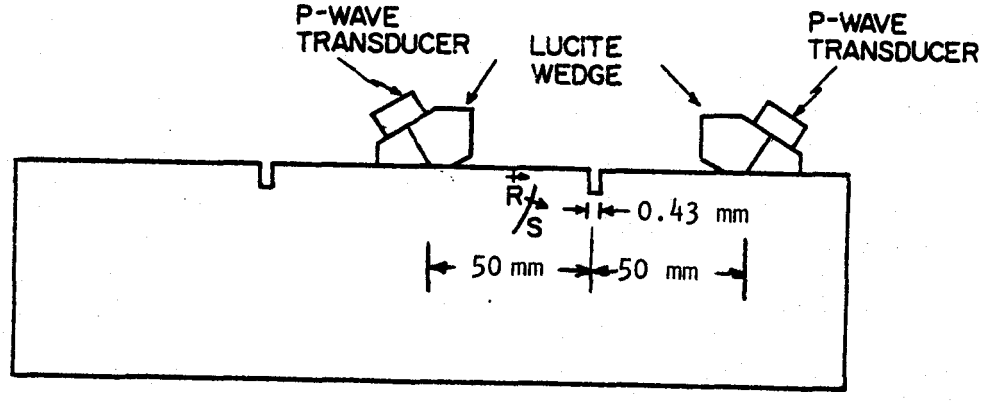

Fig. 4.22. Ultrasonic test set up, showing the input wavefronts

ing to a frequency of 5 MHz in 0.64 mm and 0.6 mm, and for 1 MHz 3.2 mm and 3 mm respectively).

2. Testing

The test specimen were low carbon steel blocks, 50 x 50 x 180 mm with 0.43 mm wide slots cut in the edge. The slots were of 1, 2, 3, 4 and 5 mm deep. Three additional slots 8, 11 and 14 mm deep were also machined to verify that, once the slot is deeper than the wave the undercut R-wave will not be present. It would have been better to have used fatigue cracks instead of slots. But since, this research was only the first step in a program for sizing cracks by means of frequency analysis we decided to work with thin slots instead. For the steel, the ratio of wavelength to slot width was 1.39 corresponding to 5 MHz and 6.95 for 1 MHz R-wave. We considered the slot to be "thin," i.e. it would behave as if it had a single tip. The transducers were placed on the steel block as in Fig. 4.23. The distance between the point on the wedge, where the center line axis of the transducer meets the steel block was kept 50 mm from the slot, for both the transmitter and the receiver (see Fig. 4.22). The transducers were connected to a pulser receiver and an oscilloscope as shown in Fig. 4.24. Its schematic is shown in Fig. 4.25.

The signals received by the transducers for various slots are shown in Fig. 4.26 which represents 8 photographs from the screen of an oscilloscope.

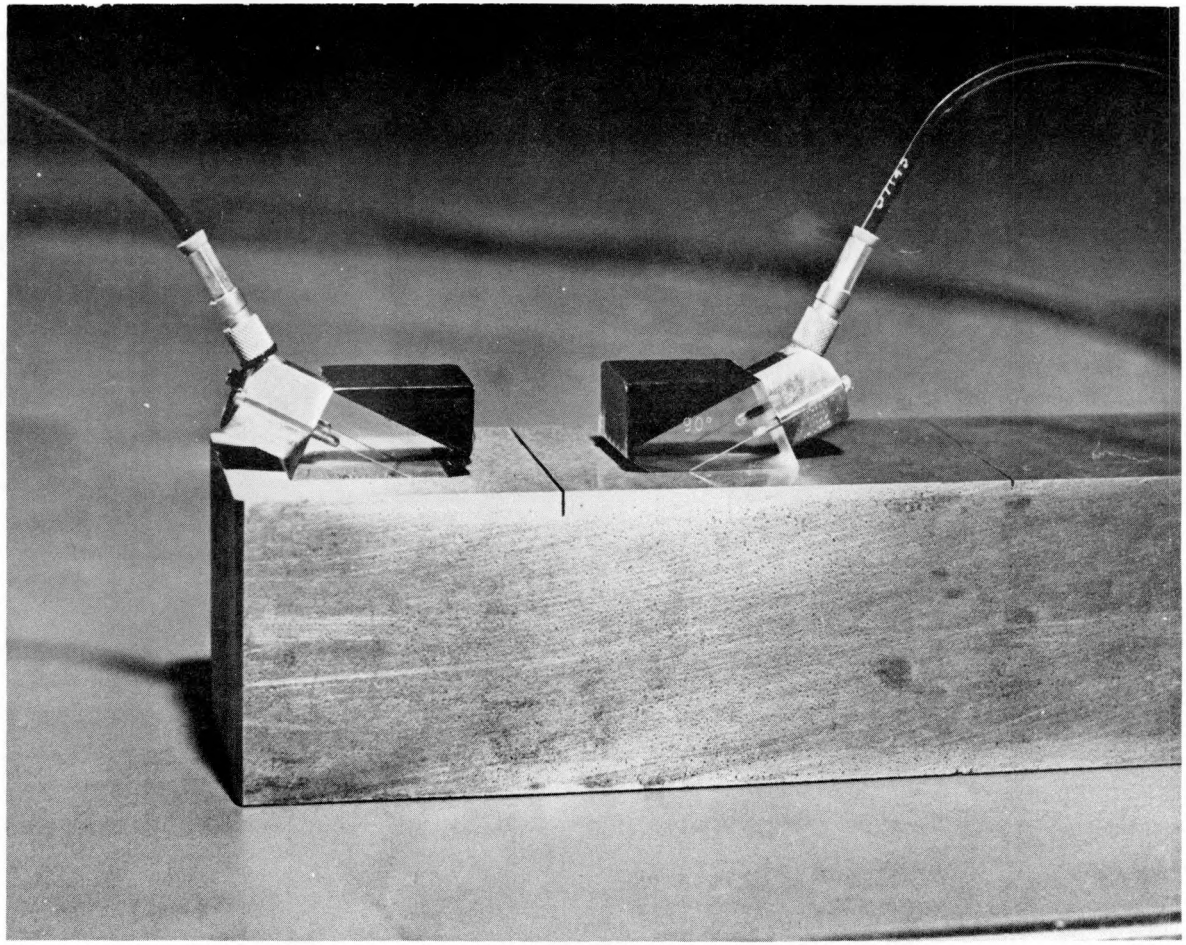

Fig. 4.23. Transducer on steel block with slot

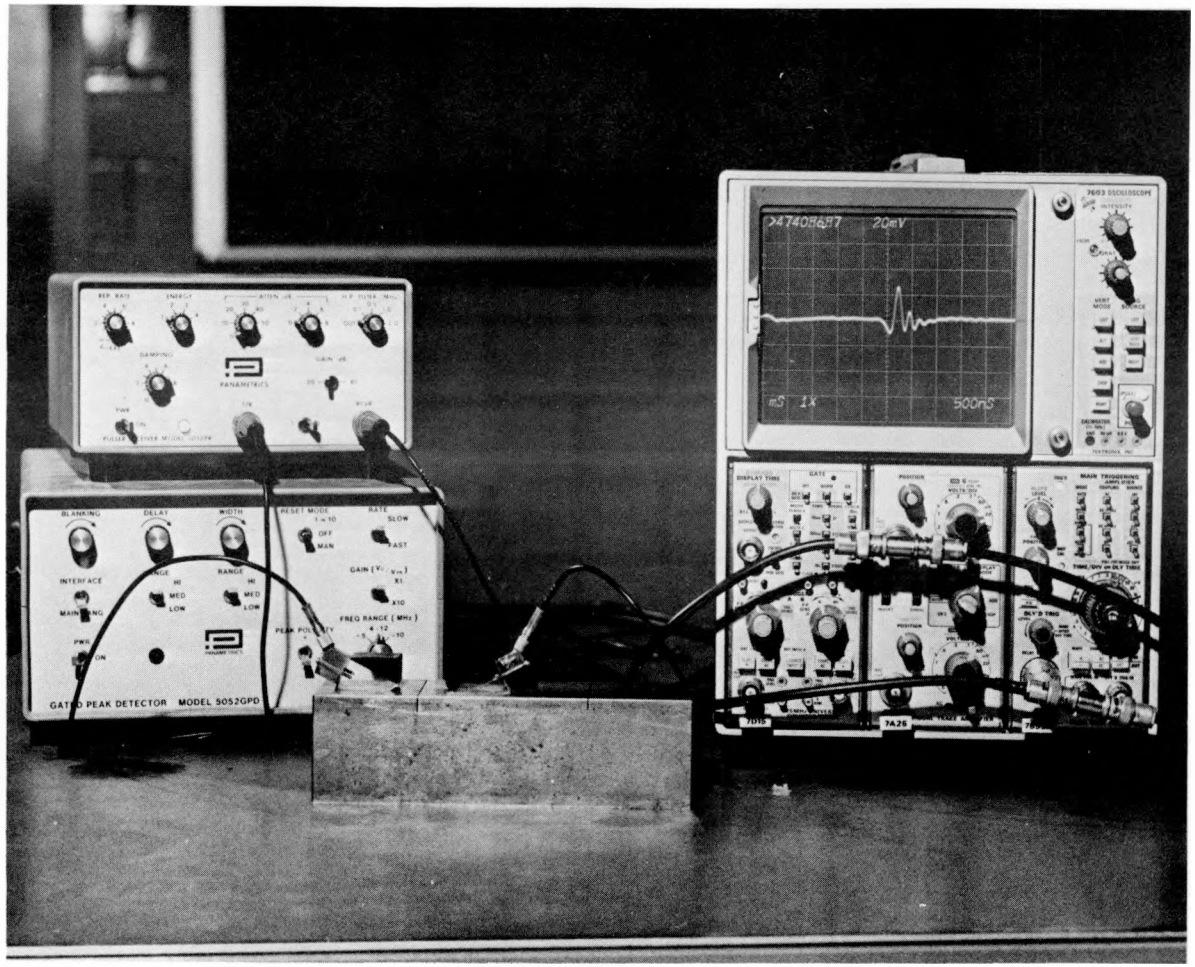

Fig. 4.24. Ultrasonic test set up, pulser receiver on left, test scope on the right

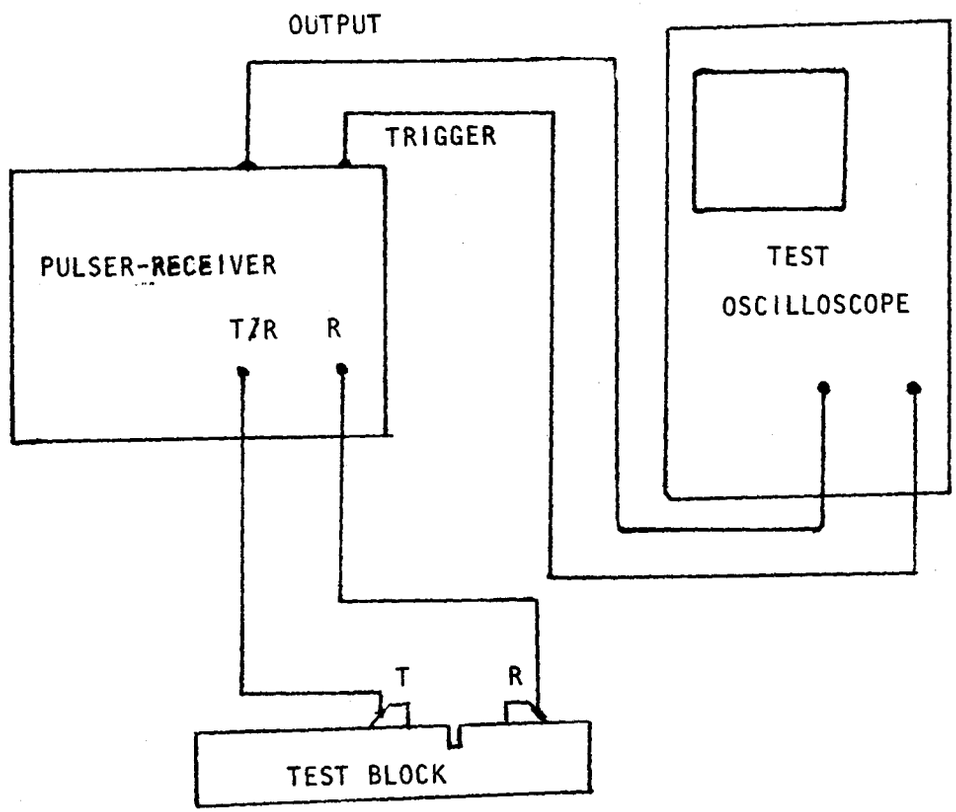

Fig. 4.25. Schematic of ultrasonic test setup

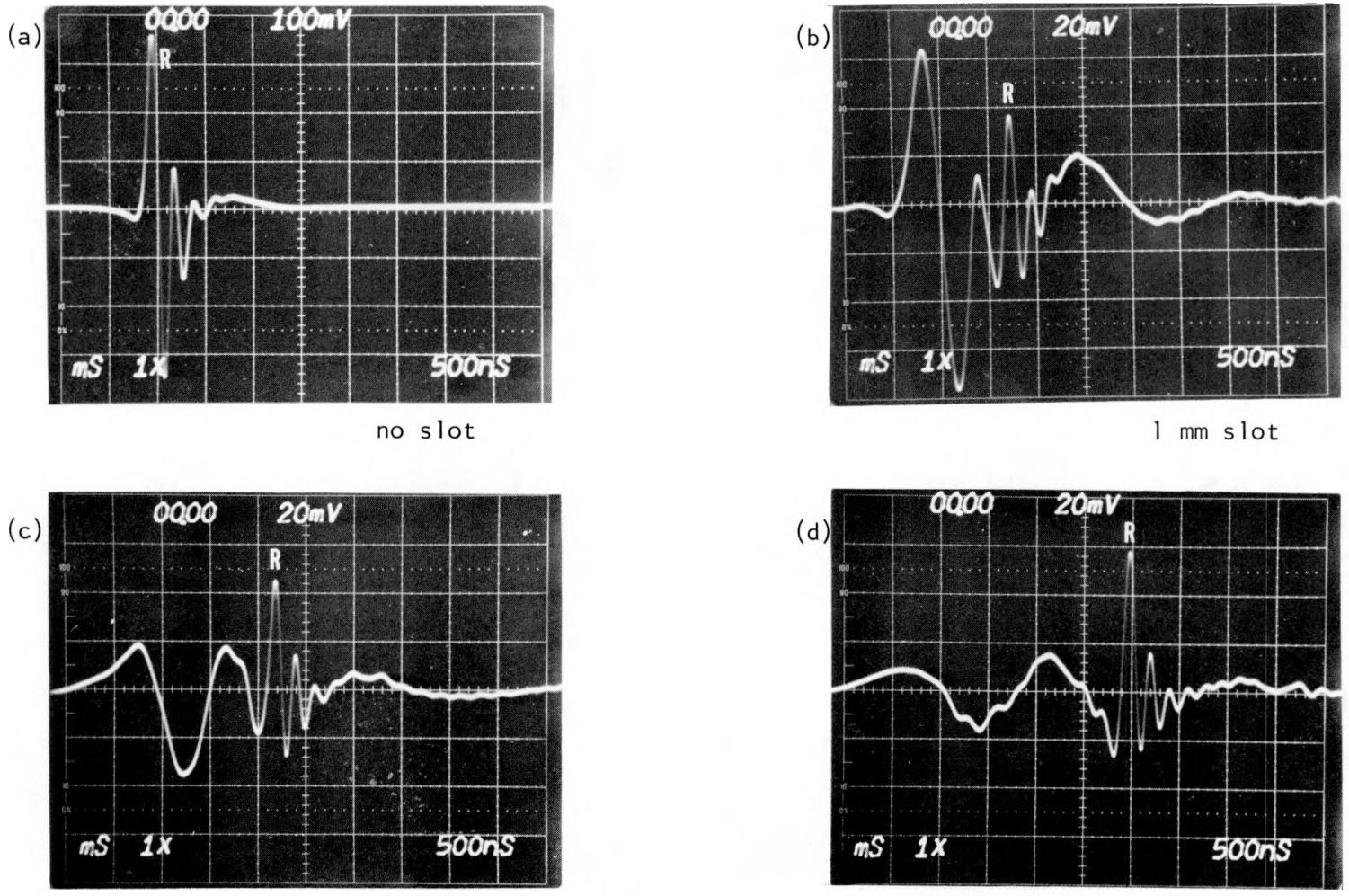

no slot

1 mm slot

2 mm slot

3 mm slot

Fig. 4.26. Transmitted signals for various slot depths

(e)

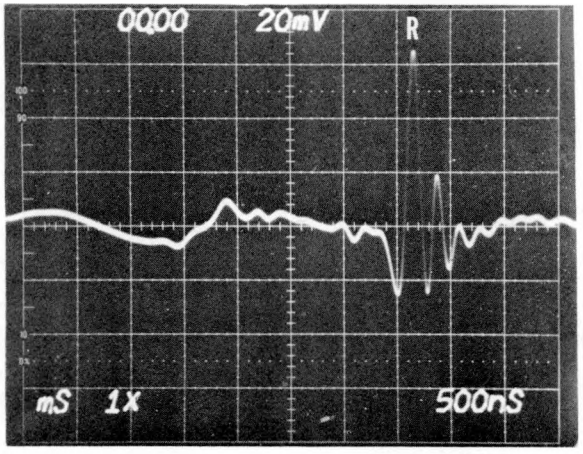

4 mm slot

(f)

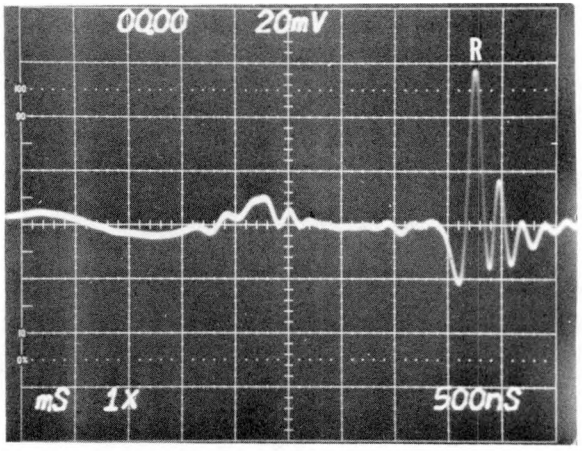

5 mm slot

(g)

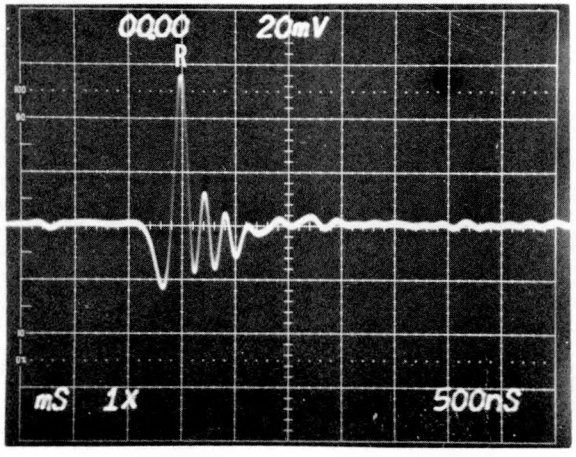

8 mm slot

(h)

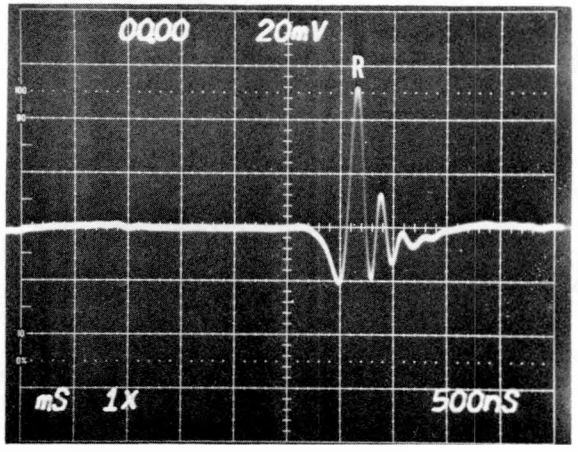

11 mm slot

Fig. 4.26. Transmitted signals for various slot lengths

In each of the pictures of Fig. 4.26 the horizontal axis represents time. The sweep rate was 500 nanoseconds per division or 5 microseconds for the full sweep. The relative sensitivity for the vertical scale is given in milivolts at top center of each picture. They are all the same, 20 mV/div except for the first where the signal was much stronger and had to be recorded at a lower sensitivity of 100 mV. On the same scale as the other pictures this signal would have been five times larger than shown. Time starts at the left. Thus, reading from left to right will identify the signals received by the "receiver" transducer in sequence. The caption "R" indicates a Rayleigh wave. The first picture (at 100 mV/division) is of the signal that arrived at the receiver when there was no slot in the plate. It represents the "input" signal for all the subsequent pictures, which were taken for different slot depths as indicated. This is a pure R wave.

Two particular characteristics are observed in Fig. 4.26 (b, c, d and e). First of all a sharp signal, captioned R, is observed in all of them. The shape of this signal does not change significantly with slot depth, only its amplitude changes slightly. This signal also lags behind all other signals and the lag increases with slot depth. This is the Rayleigh wave which went all around the slot, and is called the "cut off" R-wave. The second characteristic is the form of the front signal which leads the cut off R-wave. It is seen that this signal has the same form, i.e. two peaks and a valley on all four pictures, i.e. up to a slot depth of 4 mm. As the slot depth increases

from 1 to 4 mm, the signal decreases in amplitude and broadens out. This signal leads the cut off R-wave and, therefore, consists of 1) The shear wave that was diffracted by the tip point, the incident shear wave and the deep portion of R-wave. 2) The undercut R-wave (3) Other mode converted waves. Since this signal is a mixture of several waves, it is not perfectly smooth. The various waves present in this signal cannot be identified as they arrive at approximately the same time.

When the slot depth is 5 mm and more the front signal becomes weak and dies off. This is because the depth of the slot becomes greater than the depth of input R-wave. Also the diffracted shear wave from the incident shear wave decreases due to increase in the angle of diffraction.

It is also seen that the cut off R-wave amplitude does not change significantly when the slots are deep. The signal is smaller for the 1 mm slot, and increases for 2 mm and then for 3 mm. This is because as the slot depth increases from 1 mm onward there is less undercutting and scattering of the wave at the tip, and more and more of it goes around the slot. After 4 mm the amplitude of the R-wave changes little with depth as the slot depth is more than the depth of the input R-wave and there is no undercutting. The amplitude falls slightly due to attenuation because the path length from transmitter to receiver is larger with deeper slots.

3. Frequency analysis

The schematic of the computer hardware used for the analysis is shown in Fig. 4.27. The sample is taken from the ultrasonic pulser receiver through a Tektronix sampling scope. The sampling scope is interfaced to a LSI-11 minicomputer. The software in the system is capable of sampling the signal, finding the FFT, displaying it and plotting it through a X-Y plotter. Figure 4.28 shows the photograph of the data analysis system.

The transmitted signals were sampled for all the machined slots. Care was taken to include all the transmitted signals in the sample, from the first signal to the last signal, which is the cut off R-wave.

The frequency magnitude of all the transmitted signals is plotted in Fig. 4.29. These resemble very closely to those in Fig. 4.19 which was obtained by dynamic photoelasticity. The attenuation of frequencies starts from the high frequency end. Careful analysis of the figure reveals that all the curves approach the same plateau, at higher frequencies. The plateau is, in fact, the curve corresponding to a slot of 5 mm. After the curves have dropped to the level of the plateau, they follow approximately the 5 mm curve. The curves for 8, 11 and 14 mm deep notches are similar to the one for 5 mm. They are not drawn. The plateau curve corresponds to the frequency spectrum of the cut off R-wave which is the only major signal for slots of 5 mm and longer. Thus, if the cut off R-wave is removed from all the transmitted signals,

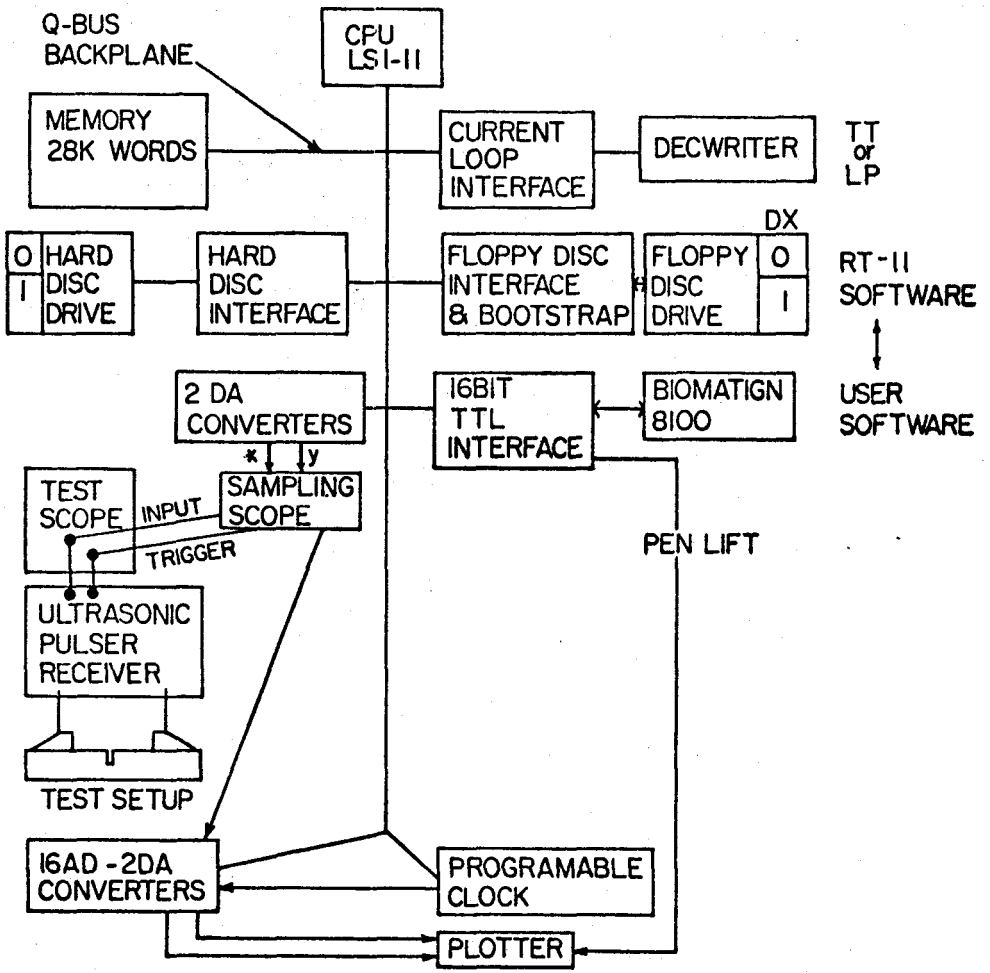

Fig. 4.27. Schematic of Computer Hardware

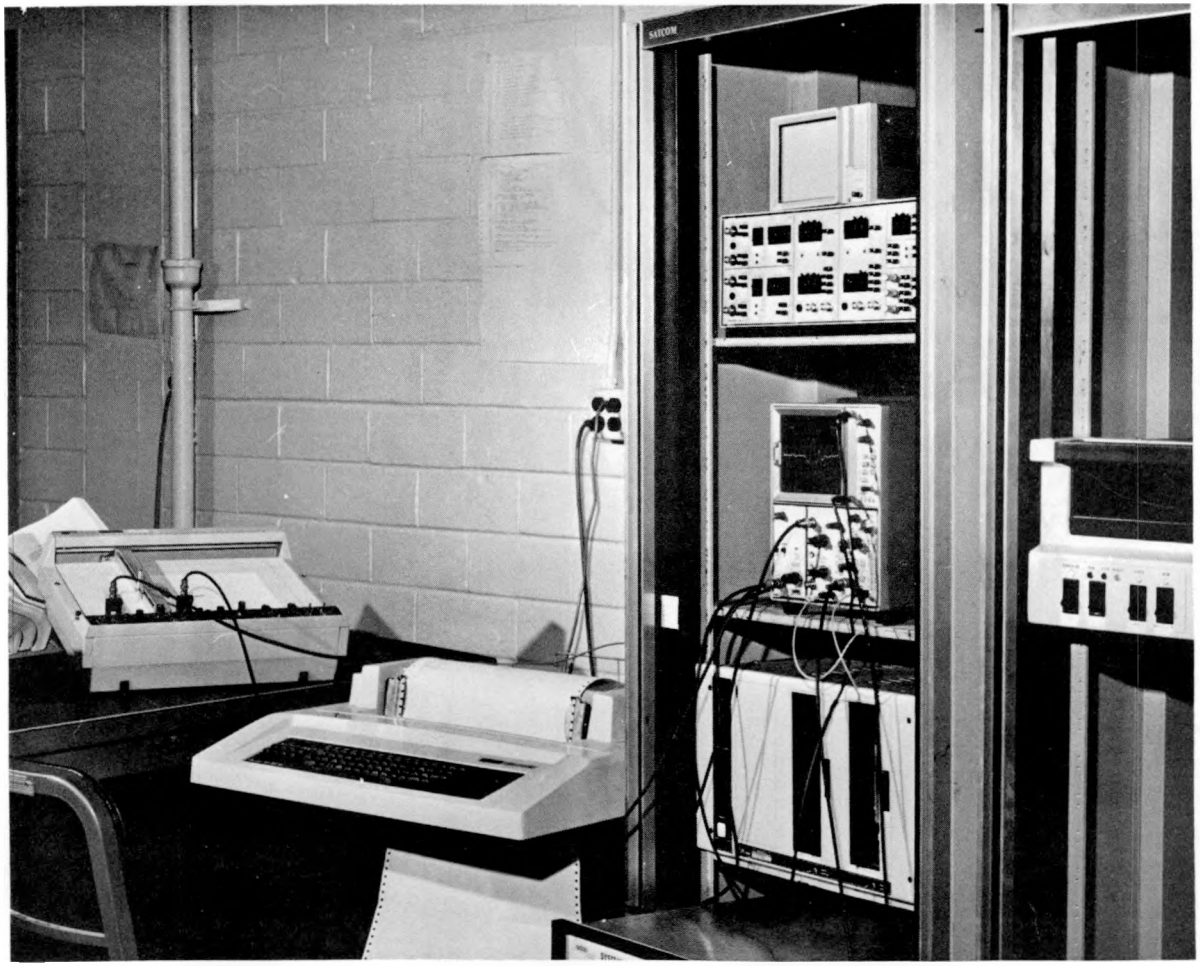

Fig. 4.28. Data Analysis system

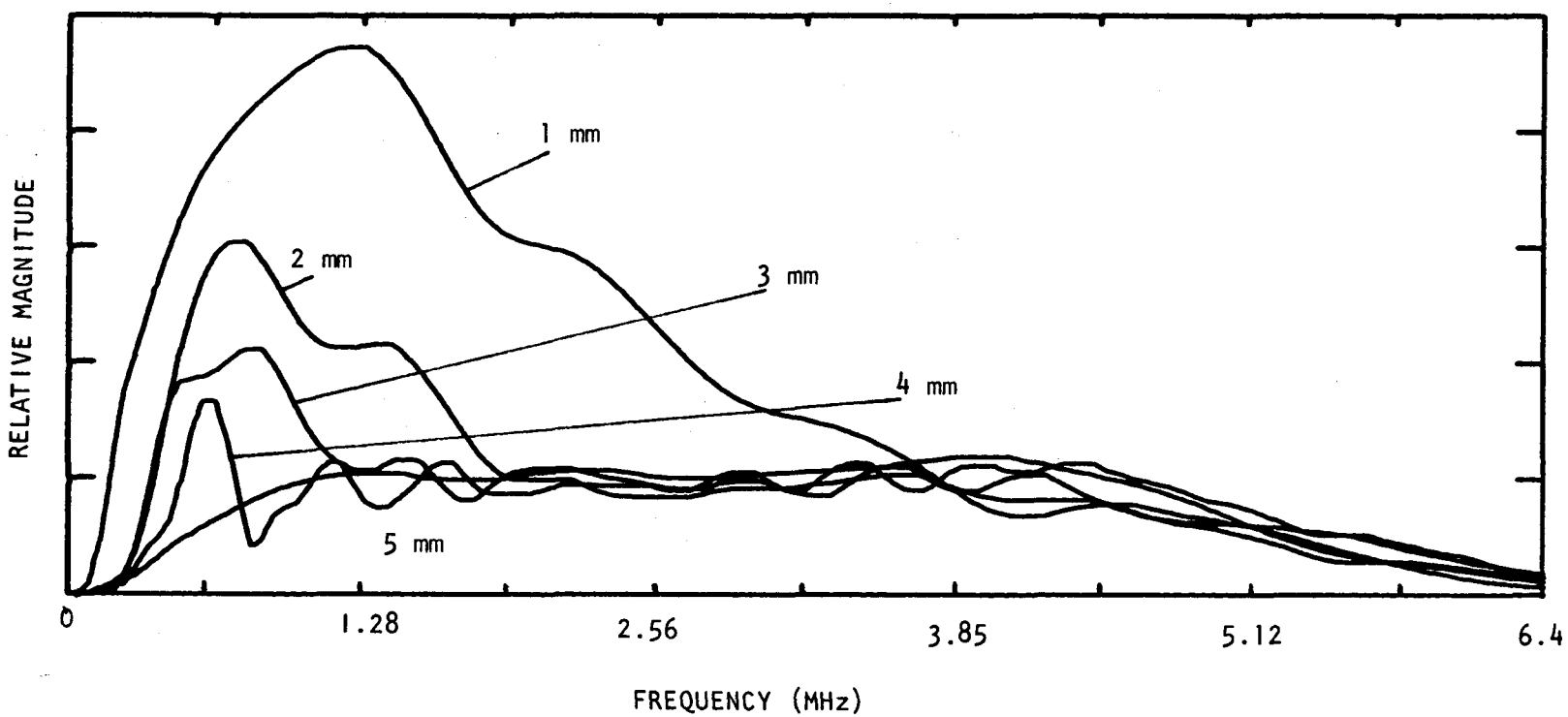

Fig. 4.29. Frequency magnitude of the transmitted signals

the plateau will be removed. The last signal, i.e. the cut off R-wave was digitally zeroed and the frequency magnitudes plotted in Fig. 4.30. The curves obtained were smooth and showed very clearly that the attenuation of frequency components started from the high frequency end and proceeded to lower frequencies as the slot depth increased. It should be known that the curves in Fig. 4.30 correspond to the frequency magnitude of the undercut R-wave, the diffracted S-wave from the incident S and R-waves, and mode converted waves. The mode converted signals are very small and clearly do not have a significant effect, except in cases where the undercut R-wave and the diffracted S-wave is weak.

Fig. 4.30 confirms what previous figures suggested, namely that the frequency attenuation starts from the higher side and moves to the lower side. To correlate this aspect quantitatively, it is necessary to relate a particular point on the curve to the slot depth. One of the points chosen was where the frequency magnitude first goes to a minimum. It was called the "cut off" point. It is called the cut off point, as the frequency components which are higher than the frequency corresponding to this point were "cut off" by the slot. These points on the curves are indicated as C_1, C_2, C_3, C_4 corresponding to 1 mm, 2 mm, 3 mm and 4 mm slots. Secondly the peak of the curves can also be related to the slot depth. These points are called P_1, P_2, P_3, P_4 as shown in Fig. 4.30. The "cut off" points and the

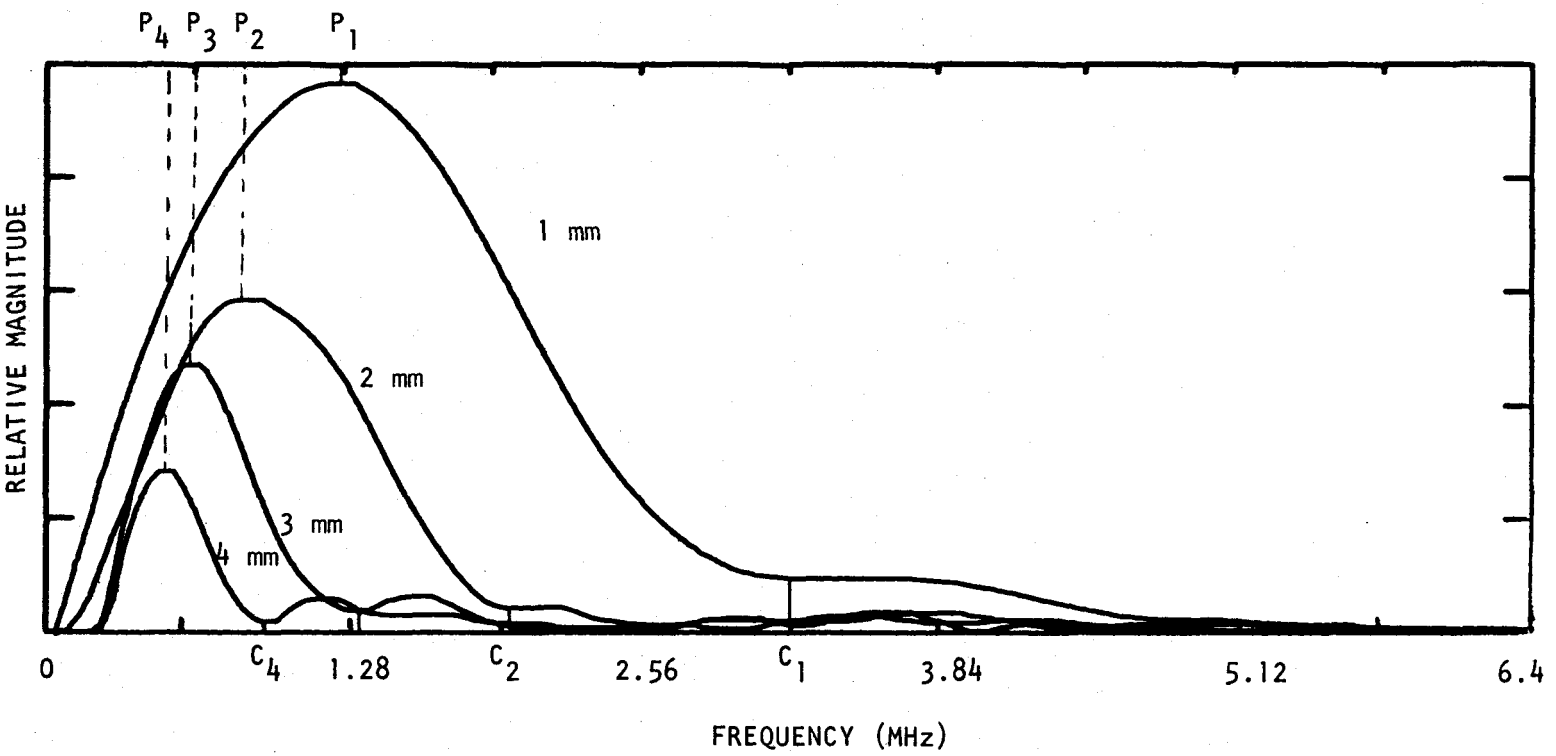

Fig. 4.30. Frequency magnitude of the undercut R-wave and diffracted shear wave

"peak" points are also obtained from Fig. 4.30. The wavelengths corresponding to the peak and cut off points are tabulated in Table 4.3 and plotted in Fig. 4.31 and 4.32.

If this technique for sizing cracks is to be useful, the indications should be insensitive to the distance between the two transducers and to variations in the electrical damping of the instruments. Fig. 4.33 shows the affect of distance for a 3 mm slot. The cut off frequency was the same when the distance between the transducers was varied from 60 to 190 mm. The peaks of the curves did change slightly. Fig. 4.34 shows the effect of damping on the cut off and peak points. It shows that the relative magnitudes of the peak points change, but the frequencies corresponding to the peak points and the cut off points remain unchanged.

From Fig. 4.31 is has been found that the curve which relates the slot depth to the cut off wavelength is nearly a straight line with a slope of 0.8. Thus a slot will filter off all the wavelengths which are less than 0.8 times the slot depth. The cut off points thus corresponds to a wavelength which is 0.8 times the depth of the slot. Thus the slot depth is 1.25 x cut off wavelength.

4. Inclined slots

Since this method is primarily a depth determining method, the depth (not the length) of inclined slots can be found. This becomes very important in fracture mechanics where depth is the most significant parameter.

Table 4.3. Frequencies and wavelengths corresponding to cut off and peak points

Slot (mm)	Cut off frequency (MHz)	Cut off wavelength (mm)	Peak frequency (MHz)	Peak wavelength (mm)
1	3.19	0.9	1.25	2.4
2	2.00	1.5	0.85	3.5
3	1.35	2.2	0.64	4.7
4	0.93	3.2	0.52	5.8

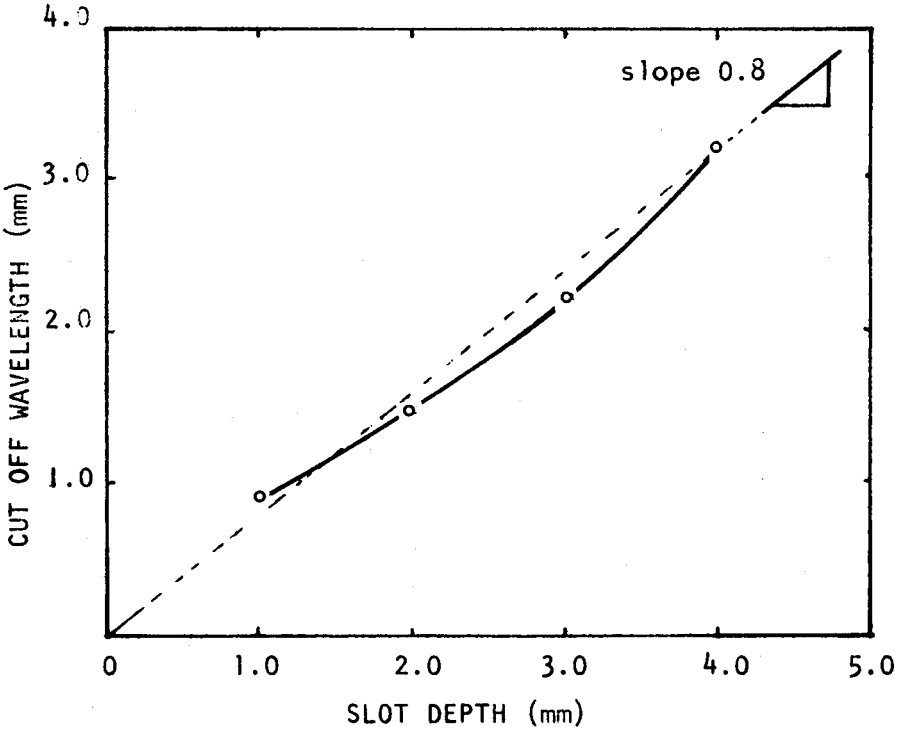

Fig. 4.31. Slot depth vs cut off wavelength (——), line with slope = .8 (---)

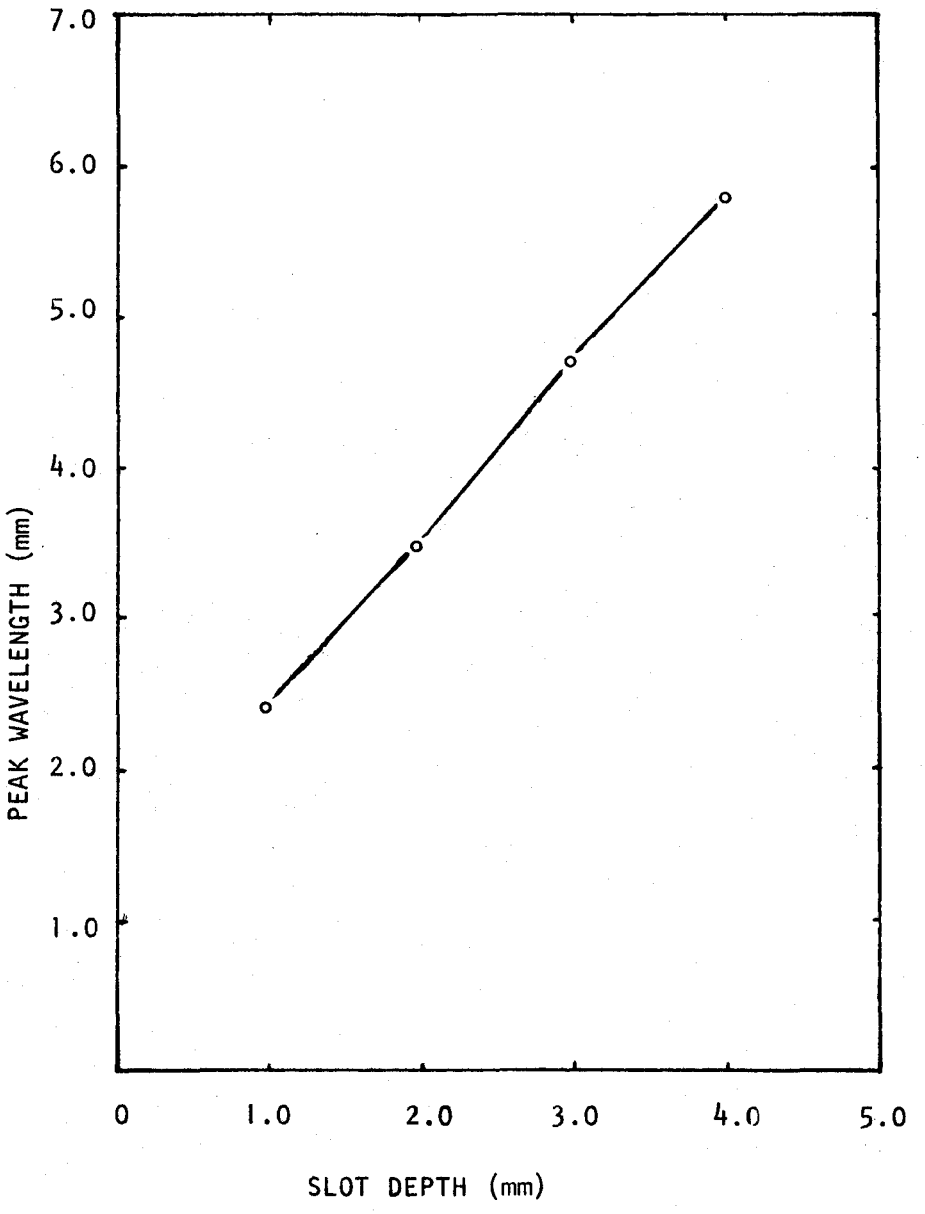

Fig. 4.32. Slot depth vs peak wavelength

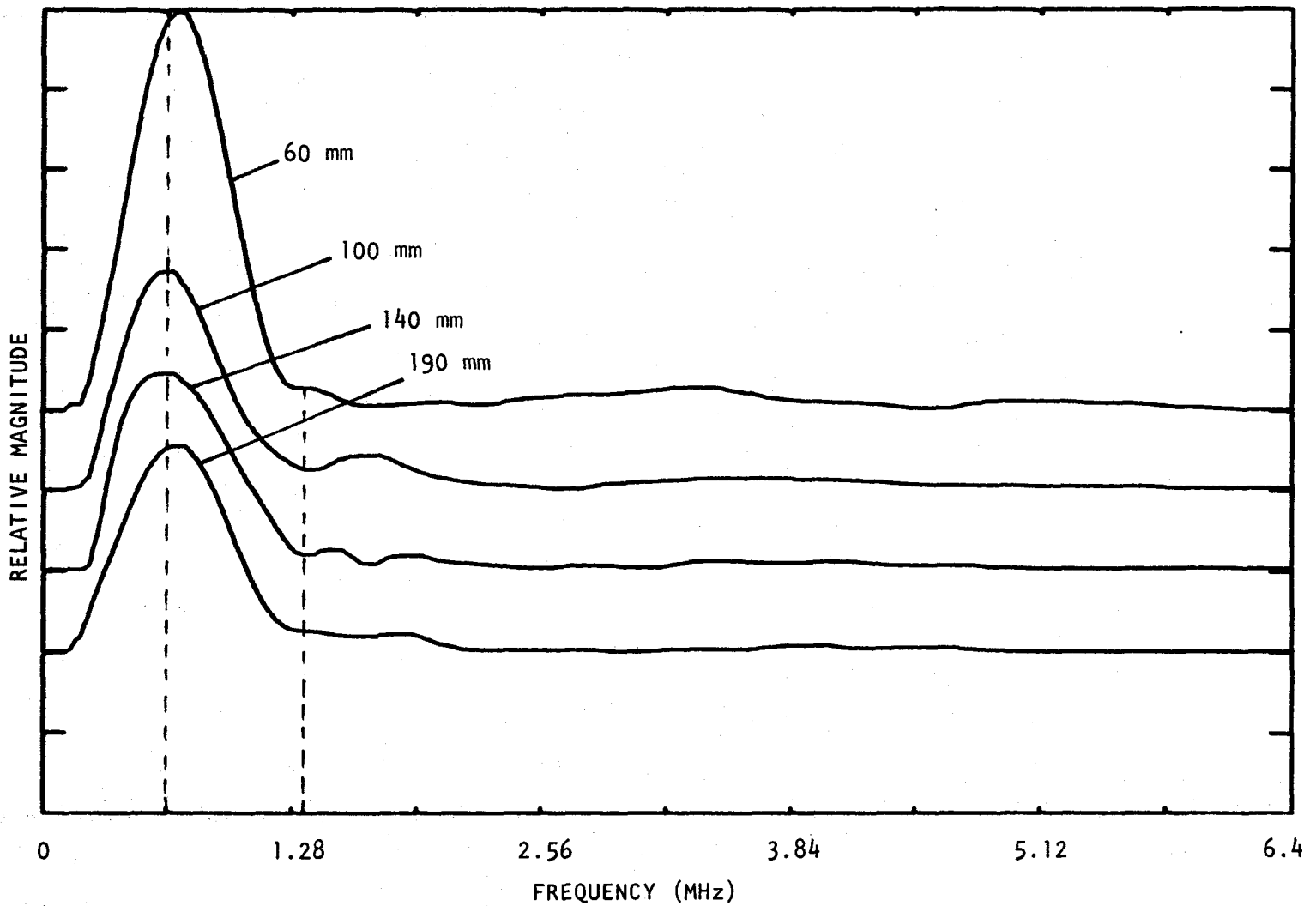

Fig. 4.33. Effect of distance between the transducers on the frequency magnitude of the undercut R-wave and diffracted shear wave (3 mm slot)

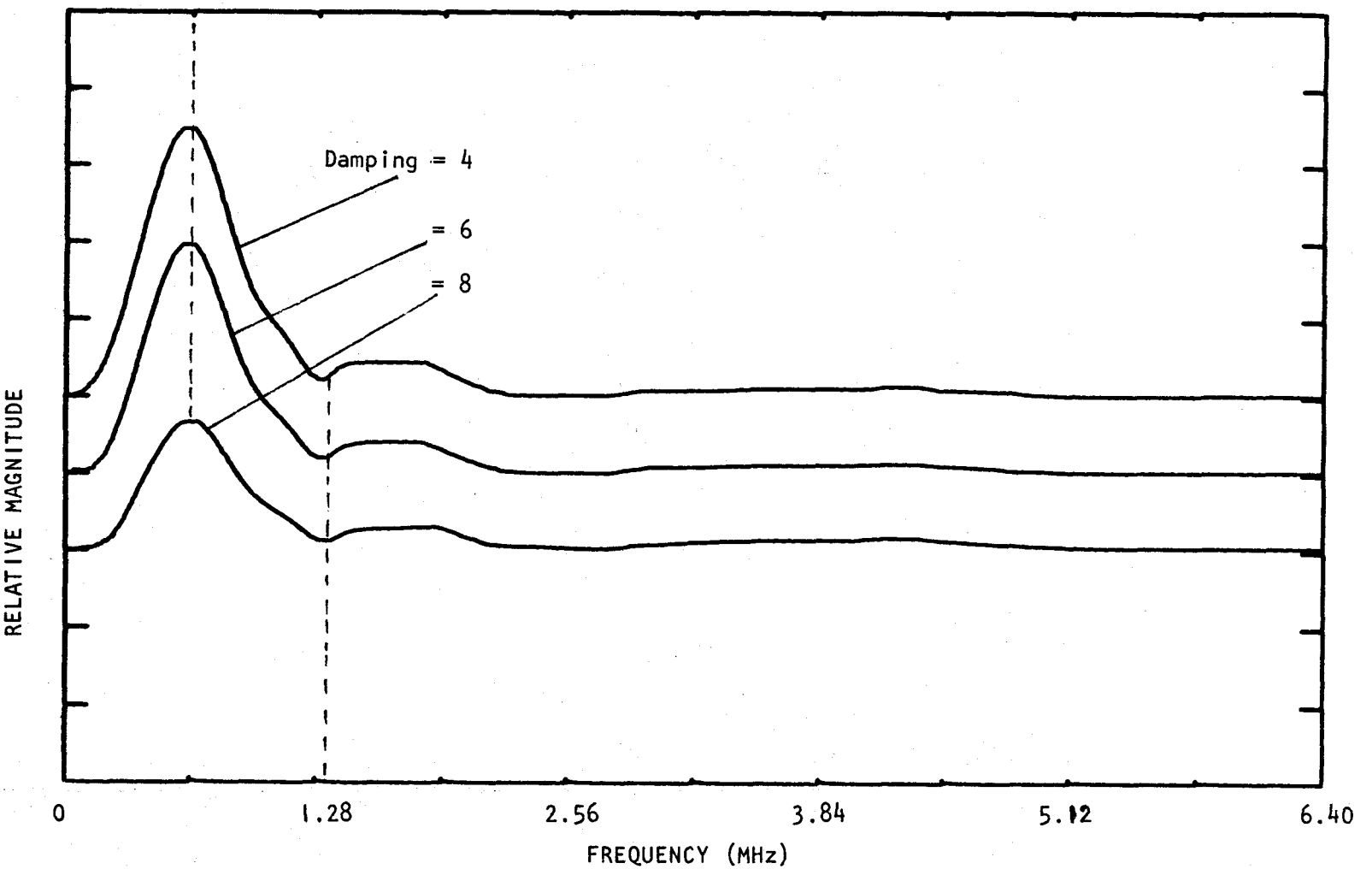

Fig. 4.34. Effect of electrical damping on the frequency magnitude of the undercut R-wave and diffracted shear wave (3 mm slot)

Two slots, of length 2 mm and 5 mm cut at 45° to the square of the plate, were tested. Their depths were, therefore, 1.4 and 3.5 mm, respectively. Fig. 4.35 shows the transmitted signals for the two inclined slots. Figures (a) and (b) are for the 2 mm long (1.4 mm deep) slot and figures (c) and (d) for the 5 mm long (3.5 mm) deep one. In Figs. (a) and (c) the wave is incident on the 35° corner. For (b) and (d) it is incident on the 45° corner. Fig. 4.35(a) and (b) shows that if the transmitter and receiver are interchanged, the signal remains unaffected. The same is true for the 5 mm slot. Also, it is found that the cut off R-wave is inverted as compared to the normal slots, when the slot length is 5 mm.

The frequency magnitudes for the cut off points corresponding to these slots are shown in Fig. 4.36 and tabulated in Table 4.4. When the cut off wavelengths were computed and read into Fig. 4.31 the depth was found as 1.5 mm and 3.8 mm. On using the formula (1.25 x cut off wavelength) the depth was found to be 1.5 mm and 3.7 mm when the peak points on Fig. 4.36 were likewise read into Fig. 4.32 they gave the depths as 1.7 mm and 4 mm. The peaks do not have a good theoretical basis to be related to the slot depth yet the results are remarkably close to actual values.

The cut off points, however, have a physical explanation and it is clear from the results that they can be used to find the depths of surface breaking slots very accurately.

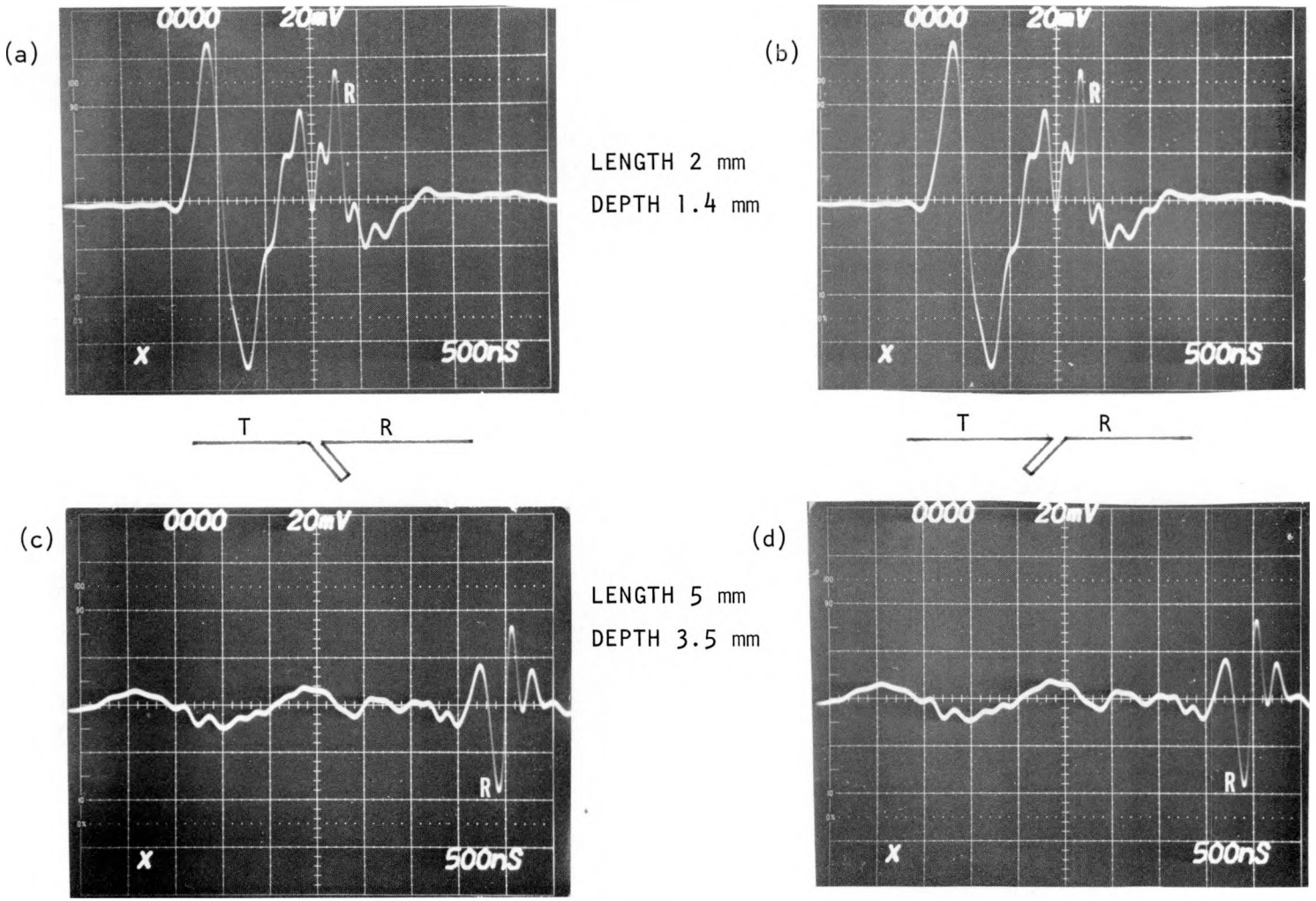

Fig. 4.35. Transmitted signals for inclined slots

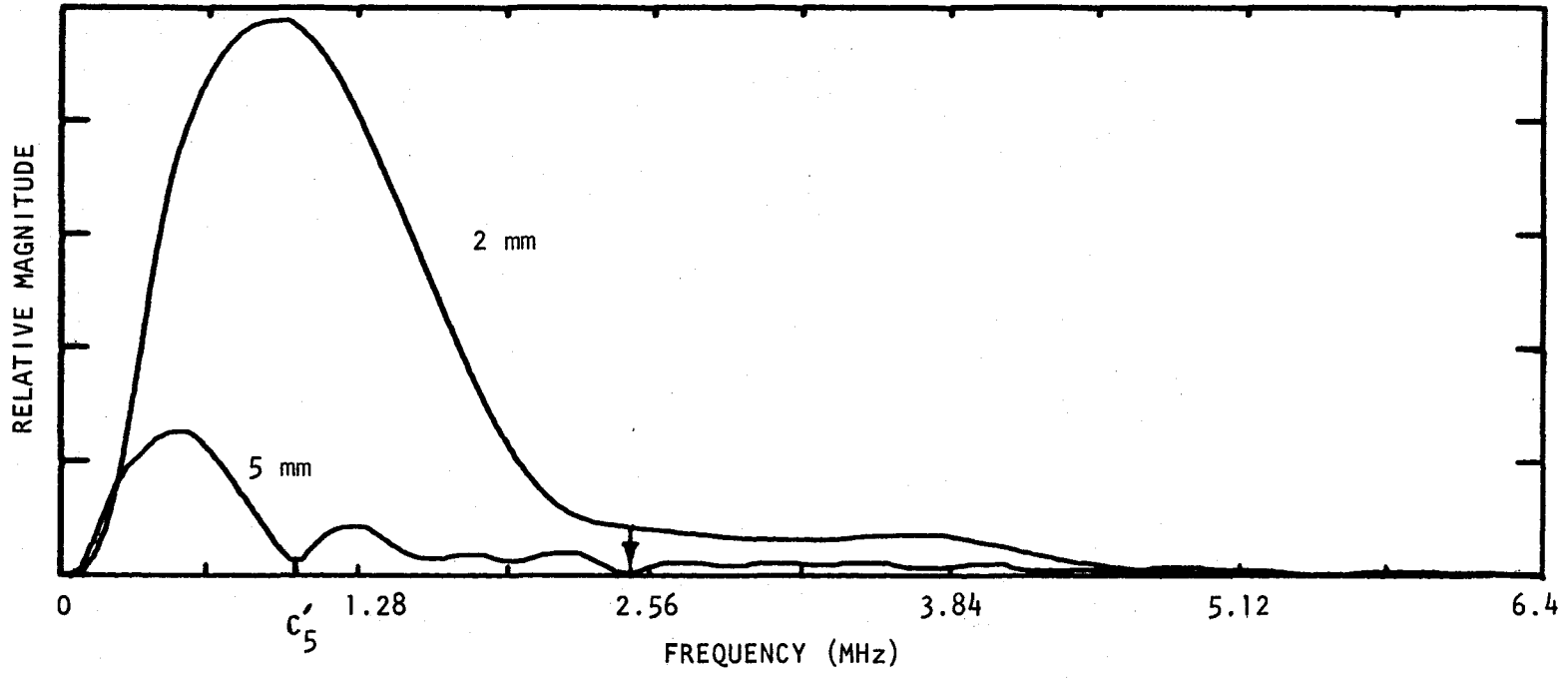

Fig. 4.35. Frequency magnitude for inclined slots

Table 4.4. Depth predicted for inclined slots using the cut off point, peak point and the formula

Slot length (mm)	Slot depth (mm)	Cut off frequency (MHz)	Cut off wavelength (mm)	Peak frequency (MHz)	Peak wavelength (mm)	Depth predicted by Cut off wavelength on extrapolation (Fig. 4.31) mm	Depth predicted by Peak wavelength on extrapolation (Fig. 4.32) mm	Depth predicted by the formula (1.25 x cut off wavelength) mm
2	1.4	2.45	1.2	.92	3.2	1.5	1.7	1.5
5	3.5	1.00	3.0	.52	5.8	3.8	4.0	3.7

C. Conclusions

The property of the Rayleigh wave which relates the wavelength to its depth below the surface, has been effectively used to find the depths of slots. Fig. 4.31 shows that the depth of a slot is nearly linearly related to the wavelength. The slope of the line is. 0.8. Thus a slot of 3 mm cuts off all the wavelengths which are less than about 2.4 mm. The theory (29, 39), predicts that the particle motion excited by an R-wave is localized to a depth of 2λ. The results from both photoelastic and ultrasonic tests show that the slot is a fairly efficient filter for wavelengths less than 0.8 times the slot depth. The wavelengths in the undercut R-wave and other waves scatterd from the slot tip, are all longer than 0.8 times the slot depth. Thus the slot depth is 1.25 x cut off wavelength.

So in using this technique for inspection purposes the bandwidth of the R-wave should be such that the shortest wavelength (highest frequency) is 0.8 times the shortest crack depth that needs to be inspected. The largest wavelength (lowest frequency) should be longer than 0.8 times the deepest crack that is expected. Increasing the maximum wavelength to one times the crack depth gives a better resolution and should be considered the preferred limit. In doing this, the undercut R-wave will be much stronger than the mode converted waves and will thus be affected less by them. Thus if it is required to size cracks from 1 mm to 10 mm, the wavelengths in the R-wave, should be from 0.8 mm to 10 mm.

This analysis is based on the results from 4 slots. The full validity of the technique should now be tested on a larger sample (more specimens) and over a larger range of crack depths.

Once the technique for sizing slots is confirmed, it should be applied to fatigue cracks. It is predicted that the fatigue cracks will result in the same kind of relationship between the slot depth and the cut off wavelength. Tests should also be run to confirm that different transducers will give the same results, i.e. even though the frequency curves of the transducers are different the cut off wavelengths will be the same.

After working on steel, different structural materials should be tested and the relationship of the cut off wavelength with crack depth found.

It is often not possible to place a transmitter and a receiver on opposite sides of a crack. However, an indirect R-wave can be generated when an SV-wave strikes a surface at an angle greater than some critical value. Schmerr (41) has studied the pulse distortion of an SV-wave at a free surface which will generate a R-wave. This technique for using indirectly induced R-waves should be developed.

This study did not consider the effects of residual stresses and/or plastic zones near the tips of slots. Such zones almost always exist at crack tips. So, a program to evalute the effect of residual stresses on the accuracy of the technique should be initiated.

Since in most applications it is far more convenient to use one probe, the possibility of using the reflected signal should be tried. This signal should have more high frequency components. The only requirement in this case is likely to be that the input wave should be much deeper than the crack. If the crack depth is not much smaller than the wave depth, the reflected signal will be very strong. Thus the effect of a small change in crack depth will be insignificant on a strong reflected signal. When the crack size is small enough compared to the depth, the incremental change on the reflected signal, which will then be weak, is much more significant.

V. BIBLIOGRAPHY

1. A. L. Robinson. "Making nondestructive evaluation a science." Science, 205 (1979), 477-479.

2. M. J. Buckley. "The future economic role of NDE." IEEE Trans. on Sonics and Ultrasonics, 23 (1976), 287-292.

3. R. B. Thompson and A. G. Evans. "Goals and objectives of quantitative ultrasonics." IEEE Trans. of Sonics and Ultrasonics, 23 (1976), 292-299.

4. E. P. Papadakis. "Future growth of nondestructive evaluation." IEEE Trans. of Sonics and Ultrasonics, 23 (1976), 284-287.

5. R. S. Sharpe. "The Harwell Non-Destructive Centre." British Journal of Non-Destructive Testing, 21 (1979), 131-134.

6. G. S. Kino, T. M. Waugh, P. D. Corl, C. S. DeSilets and P. M. Grant. "Acoustic imaging techniques for nondestructive testing." Preprint G. L. Report No. 2815. Department of Electrical Engineering, Stanford University, Palo Alto, CA, May 1978.

7. J. Krauthkramer and H. Krautkramer. Ultrasonic Testing of Materials. New York: Springer-Verlag, 1977.

8. J. R. Birchak and C. G. Gardener. "Comparative ultrasonic response of machined slots and fatigue cracks in 7075 aluminum." Materials Evaluation, 34 (1976) 275-280.

9. D. M. Corbly, P. F. Packman and H. S. Pearson. "The accuracy and precision of ultrasonic shear wave flaw measurements as a function of stress on the flaw." Materials Evaluation, 28 (1970) 103-110.

10. M. T. Resch. B. T. Khari-Yakub, G. S. Kino and J. C. Shyne. "Stress intensity factor measurement of surface cracks." First International Symposium on Ultrasonic Materials Characterization, National Bureau of Standards, Washington, DC, 1978.

11. B. H. Lidington, D. H. Saunderson and M. G. Silk. "Interference effects in reflection of ultrasound from shallow slits." Non-Destructive Testing, 8 (1975), 185-190.

12. B. Bottcher, E. Schulz and H. Wustenberg. "A new method or crack determination in ultrasonic material testing." Proc. of the 7th International Conference on Non-Destructive Testing, Warsaw, 1973.

13. M. G. Silk and B. H. Lidington. "The potential of scattered or ultrasound in the determination of crack depth." Non-Destructive Testing,

8 (1975), 146-151.

14. H. W. Reinhardt and J. W. Dally. "Some characteristics of Rayleigh wave interaction with surface flaws." Materials Evaluation, 28 (1970), 213-220.

15. L. J. Bond. "A computer model of the interaction of acoustic surface waves with discontinuities." Ultrasonics, 17, (1979), 71-77.

16. M. G. Silk. "Sizing crack like defects by ultrasonic means." Chapter 2 in Research Techniques in Non-Destructive Testing, R. S. Sharpe, Ed. London: Academic Press, 1977.

17. M. G. Silk and B. H. Lidington. "Defect sizing using an ultrasonic time delay approach." British Journal of Non-Destructive Testing, 17 (1975), 33-36.

18. M. G. Silk. "Defect sizing using ultrasonic diffraction." British Journal of Non-Destructive Testing 21 (1979), 12-15.

19. M. G. Silk. "The transfer of ultrasonic energy in the diffraction technique for crack sizing." Ultrasonics, 17 (1979), 113-121.

20. M. G. Silk and B. H. Lidington. "An evaluation of single probe bulk-wave time-delay techniques in sizing cracks in steel." NDT International, 10 (1977), 129-134.

21. M. G. Silk. "The determination of crack penetration using ultrasonic surface waves." NDT International, 9 (1976), 290-297.

22. K. G. Hall. "Crack depth measurement in rail steel by Rayleigh visualization." Non-Destructive Testing, 9 (1976), 121-126.

23. A. Ilan, L. J. Bond and M. Spivack. "Interaction of a compressional impulse with a slot normal to the surface of an elastic half-space." Geophysical Journal of the Royal Astronomical Society, 57 (1979), 463-467.

24. L. Adler, K. V. Cook and W. A. Simpson. "Ultrasonic frequency analysis." Chapter 1 in Research Techniques in Ultrasonic Testing, R. S. Sharpe, Ed. London: Academic Press, 1977.

25. L. L. Morgan. "The spectroscopic determination of surface topography using acoustic surface waves." Acustica, 30 (1974), 222-228.

26. L. W. Zachary, C. P. Burger, L. W. Schmerr and A. Singh. "Surface crack characterization by dynamic photoelastic spectroscopy." Proc. of the SESA Spring Conference, San Francisco, CA, May 1979.

27. L. J. Bond. "Finite difference methods applied to ultrasonic non-destructive testing." Proc. of the meeting on ARPA/AFML Review of Progress in Quantitative NDE, LaJolla, CA, July 1979. To be published.

28. E. A. Lloyd, D. S. Wadhwani and A. F. Brown. "Non-destructive testing of adhesive-bonded joints." Proc. of Ninth World Conference on Non-destructive Testing, Melbourne, Australia, November 1979, To be published.

29. J. D. Achenbach. Wave Propagation in Elastic Solids. Amsterdam: North-Holland Publishing Company, 1973.

30. W. M. Ewing, W. S. Jardetzky and F. Press. Elastic Waves in Layered Media. New York: McGraw-Hill Book Co., Inc., 1957.

31. J. Fraser, B. T. Khari-Yakub and G. S. Kino. "The design of efficient broadband transducers." Applied Physics Letters, 30 (1978), 698-700.

32. A. A. Oliner. Acoustic Surface Waves. Berlin: Springer-Verlag, 1978.

33. K. G. Hall. "Ultrasonic wave visualization as a teaching aid in non-destructive testing." Ultrasonics, 15 (1977), 57-59.

34. K. G. Hall. "An evaluation of ultrasonic probes by the photoelastic visualization method." British Journal of Non-Destructive Testing, 20 (1978), 171-184.

35. C. P. Burger and W. F. Riley. "Effect of impedence mismatch on the strength of waves in layered solids." Experimental Mechanics, 14 (1974), 129-137.

36. W. F. Riley and J. W. Dally. "A photoelastic analysis of stress wave propagation in a layered model." Geophysics, 31 (1966), 881-8991

37. J. B. Ligon. "A photomechanics study of wave propagation." Ph.D. dissertation, Iowa State University, Ames, Iowa, 1971.

38. C. C. Chao, H. H. Bleich and J. Sackman. "Surface waves in elastic space." Journal of Applied Mechanics, 28 (1961), 300-301.

39. M. J. Forrestal, L. E. Fugelso, G. L. Meidhardt and R. A. Felder. "Response of a half space to transient loads." Proc. of Engineering Mechanics Division Speciality Conference, ASCE, 1966.

40. L. J. Bond and A. Ilan. "Target characterization: An experimental and numerical study." Proceedings of the Ninth World Conference on Non-Destructive Testing, Melbourne, Australia, Nov. 1979. To be published.

41. L. W. Schmerr, "Pulse distortion of an SV-wave at a free surface." Journal of Applied Mehanics, 41 (1974), 298-299.

VI. ACKNOWLEDGEMENTS

On completion of my work I wish to thank the people who have helped me in this study.

First and foremost, I thank Professor C. P. Burger for the knowledge, guidance and advice given me during the research. The success of this work was dependent on his encouragement and personal interest. He has had deep concern for his graduate students, and did whatever he could to solve their problems.

Professor L. W. Schmerr devoted much of his time in guidance with ultrasonic testing and data analysis. His explanations on the fundamentals were very clear and his comments very specific. I also thank Professor L. W. Zachary for his help in the initial stages of my work involving dynamic photoelasticity. Finally, I acknowledge the financial assistance and facilities provided by Ames Lab, USDOE, and the Engineering Research Institute; Iowa State University.

Sincere thanks to Mr. Tom Elliott for helping in the laboratory and the machine shop. Thanks to Ms. Janice Ballantyne for typing the manuscript in a short period of time.